



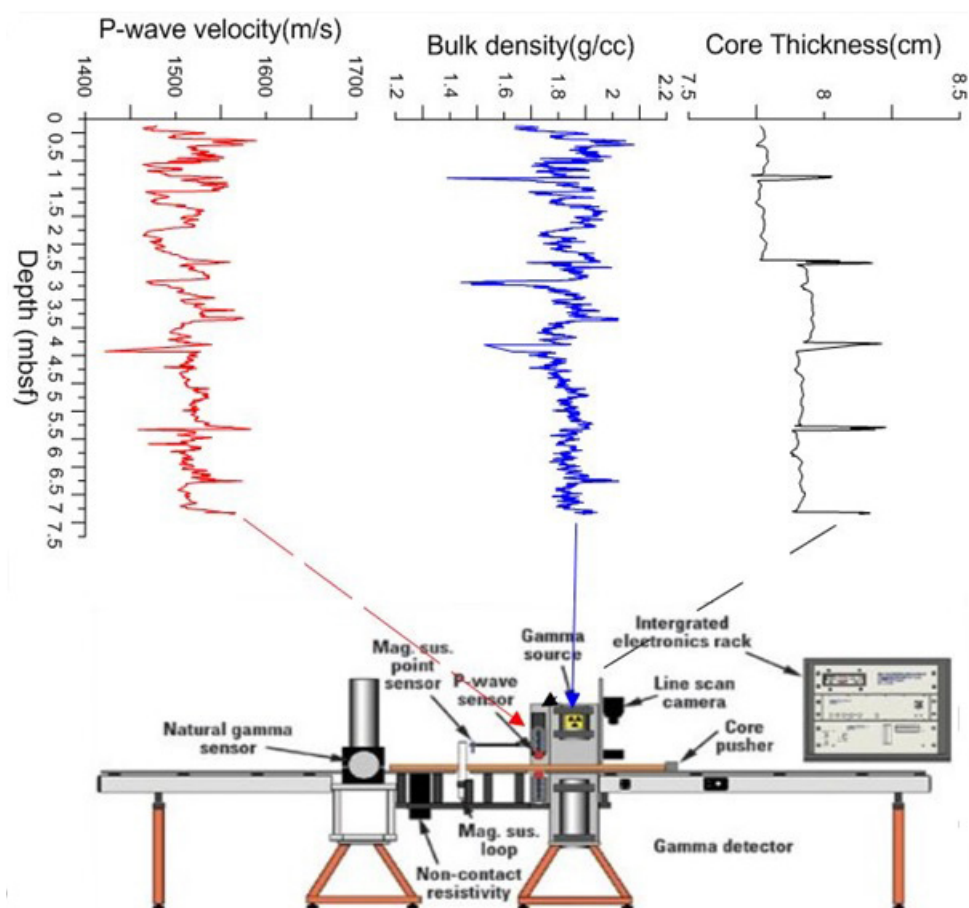
Stockholm University

Master Thesis

Degree Project in Marine Geology 45 hp

High-resolution measurements of bulk density and compressional wave velocity on split sediment cores using the Multi-Sensor Core logger

Hassan Al-Timimy



Stockholm 2013

Abstract

The compressional wave velocity and bulk density of sediments retrieved from the Lomonosov Ridge, Arctic Ocean, during LOMROGIII 2012 were measured using the Multi Sensor Core Logger (MSCL) system. A comparison of quantitative measurements of these properties on whole and split cores was conducted. Results obtained from using two types of acoustic transducers were evaluated. Data obtained from the hard P-wave transducer is more accurate than that obtained from the soft transducer, because it provides more accurate core thickness measurements. Three sources of errors in thickness measurements were identified: deformation of the oil-filled membrane surrounding the p-wave transducer, deformation of sediments caused by the load of the spring mounted in the plastic housing of the transducers, and incorrect selection of the reference point. Core thickness errors during logging have opposite influences on the calculated bulk density and the compressional wave velocity of the sediments. An identification and correction procedure for core thickness errors was developed. A comparison between compressional wave velocity and bulk density measurements of LOMROGIII sediments and published global empirical models was performed. The results showed that the widely used Raymer and Wyllie models cannot predict the compressional wave velocity-porosity relationship for Lomonosov Ridge sediments. The porosity-velocity relationship of sediments from this study is best described by the Erickson and Jarrad model.

Keywords

Multi sensor Core Logger, Arctic Ocean, Lomonosov Ridge, the compressional velocity, bulk density, whole and split cores, hard and soft transducers , porosity.

Content

1. Introduction.....	8
2. Study area.....	12
3. Methods.....	13
3.1 Sample preparation.....	15
3.2 Bulk density measurements.....	16
3.2.1. Principle of operation.....	16
3.2.2 Calibration and processing.....	16
3.3 P-wave velocity measurements.....	21
3.3.1 Principle of operation.....	21
3.3.2 Device.....	21
3.3.3. Calibration and processing.....	23
3.4 Core thickness measurements.....	25
3.4.1. The quantitative influence of core thickness errors on the P-wave velocity and bulk density measurements.....	27
4. Results.....	29
4.1 Overview.....	29
4.2 Comparison of ACT and HT data	32
4.3 statistical analyses of differences in density and velocity.....	34
4.3.1 Interpretatio of results	36
4.4 Correcting for errors in core thickness.....	38
5. Discussion	46
5.1 Velocity-density and porosity relationships.....	46
5.2 Comparison between Lomonosov Ridge sediments and porosity-velocity models.....	48
6. Conclusion.....	57
Acknowledgements.....	59
References.....	59
Appendix 1.....	63
Appendix 2.....	66
Figures and tables	
Figt.1. Map shows the Bathometry of the central Lomonosov Ridge and the locations of the collected cores during the LOMROGIII cruise 2012.....	13
Fig.2. Typical vertical MSCL configuration used in split core logging	

modified after Geotek, 2000.....	14
Fig.3. The vertical configuration of the compressional velocity, bulk density, and magnetic susceptibility units used in split core logging.....	14
Fig.4.Schematic view of the vertical configuration of the P-wave velocity and gamma ray sensors used with the MSCL modified after Gunn and Best, 1998.....	15
Fig.5. Schematic view of gamma ray logging modified after Geotek, 2000.....	16
Fig.6.Schematic diagram of gamma ray and core thickness.....	17
Fig.7. Schematic illustration of calibration piece and gamma ray components.....	20
Fig.8. Schematic view of gamma ray calibration.....	20
Fig.9. View of stainless steel piston (hard) transducer (left), acoustic filled oil rolling (soft) transducer (right)	22
Fig.10. Pulse timing window for P-wave level system.....	23
Fig.11.Schematic view of the P-wave calibration system after Geotek, 2000.....	24
Fig.12. Temperature dependence of P-wave velocity through distilled water based on equation of Leroy(1969)	25
Fig.13. A semi cylindrical aluminum piece used as a reference core thickness point.....	26
Fig.14. Schematic illustration of the core thickness measured using ACT (A) and HT (B) with illustration of core thickness errors expected when using soft transducer.....	27
Fig.15. Sediment physical properties and core thickness of PC07 from the Lomonosov Ridge measured in the upper ~7 m below seafloor using the HT (A) and ACT (B)	30
Fig.16. Sediment physical properties and core thickness of PC10 from Lomonosov Ridge measured in the upper ~7 m below seafloor using the HT.....	31
Fig.17. Cross-plot velocity-density relationships of split and whole cores from Lomonosov Ridge measured using the acoustic oil-filled rolling (soft) transducer.....	32
Fig.18.Cross-plot velocity-density relationships of split and whole cores from Lomonosov Ridge measured using the piston (hard) transducer.....	33
Fig.19. Average velocity, density data for split cores compared to spread of data from the whole core PC10.Black bars represent standard deviation. The processed velocity–density data of the PC10 are displayed in blue squares.....	34
Fig.20. Graphical display for rejection regions for two-tailed test.....	38
Fig.21. An example of P-wave velocity and core thickness relationship.....	40

Fig.22. An example of bulk density and core thickness relationship.....	40
Fig.23. Velocity-density relationships of corrected PC03, PC05, and PC09 velocity correlated with PC10 core using the correction based on increasing density and decreasing velocity values. Black bars represent the standard deviations.....	41
Fig.24. Bar diagrams illustrate the corrected and processed velocity-density relationships (gray bars) of PC06, PC07, PC08, PC11, and PC12 correlated with the processed data of PC10 (orange bars).The distribution curves(black) represent the Gaussian distribution of the data.....	42
Fig.25. Bar diagrams illustrate the corrected and processed velocity-density relationships of PC03 and PC05 compared with the PC10 data. The corrected velocity and density used velocity, density, and core thickness errors are represented in the blue, purple, and gray colors respectively. The corrected physical properties were compared with the processed velocity and density of PC10 (orange). The distribution curves (black) represent the Gaussian distribution of the data (orange)	43
Fig.26. Bar diagrams illustrate the corrected and processed velocity-density relationships of PC09 compared with the PC10 data. The corrected velocity and density used velocity, density, and core thickness errors are represented in the blue, purple, and gray colors respectively. The corrected physical properties were compared with the processed velocity and density of PC10 (orange). The distribution curves (black) represent the Gaussian distribution of the data	44
Fig.27. Cross-plot of corrected velocity-density relationships obtained by using the corrected velocity of PC03, PC05, and PC09 cores correlated with PC10.....	45
Fig.28. Cross-plot of velocity-density relationships of PC06, PC07, PC08, PC11, and PC12 cores correlated with the PC10 core.....	45
Fig.29. Comparison of data from marine box cores (Hamilton, 1971) (black crosses) and LOMROGIII data of whole core PC10 (purple squares) and split core PC06 (forest blue triangles)	47
Fig.30. The P-wave velocity-porosity relationships calculated by Wyllie et al. (1956) and Raymer et al.(1980)equations using the minimum and maximum of shale matrix velocities (2130 m/s (black square)and 5180m/s (black cross)respectively, and various matrix velocities calculated from the Wyllie and Raymer equation. The calculated velocity was plotted versus range of porosities (black star).	51
Fig.31. Normal consolidation relationship for prediction of velocity from Lomonosov Ridge sediments with the whole and split cores. The top and bottom curves represent shale fraction ($V_{sh}=1$) and shale ($V_{sh}=0$) respectively. The curves in the middle represent shale fractions 0.2, 0.4, 0.6,	

and 0.8. The velocity and porosity for split and whole core are plotted against depth, porosities calculated using different grain density are plotted (green, purple, and blue colors).....	54
Fig.32 Comparisons of global empirical relationship data compared to a wide range of velocity-porosity ranges from different regions. The heavy black lines exhibit the normal- and high-consolidation global relationship used in the model after (Erickson and Jarrad, 1998). Circle18 represent the range of normal consolidated sediments used in the Erickson and Jarrad model.....	55
Fig.33 Relationship of velocity (red color) and porosity (black color) for all split and whole cores versus depth (mbsf)	56
Fig. A2-1.The compressional velocity, bulk density, and magnetic susceptibility for the Lomonosov Ridge from LOMROGIII PC03 core plotted against depth (mbsf). The physical properties records were carried out using hard transducer.....	67
Fig. A2-2. The compressional velocity, bulk density, and magnetic susceptibility for the Lomonosov Ridge from LOMROGIII PC05 core plotted against depth (mbsf). The physical properties records were carried out using hard transducer.....	68
Fig. A2-3. The compressional velocity, bulk density, and magnetic susceptibility for the Lomonosov Ridge from LOMROGIII PC06 core plotted against depth (mbsf). The physical properties records were carried out using hard transducer.....	69
Fig. A2-4. The compressional velocity, bulk density, and magnetic susceptibility for the Lomonosov Ridge from LOMROGIII PC07 core plotted against depth (mbsf). The physical properties records were carried out using hard transducer.....	70
Fig. A2-5.The compressional velocity, bulk density, and magnetic susceptibility for the Lomonosov Ridge from LOMROGIII PC08 core plotted against depth (mbsf). The physical properties records were carried out using hard transducer.....	71
Fig. A2-6.The compressional velocity, bulk density, and magnetic susceptibility for the Lomonosov Ridge from LOMROGIII PC09 core plotted against depth (mbsf). The physical properties records were carried out using hard transducer.....	72
Fig. A2-7.The compressional velocity, bulk density, and magnetic susceptibility for the Lomonosov Ridge from LOMROGIII PC10 core plotted against depth (mbsf). The physical properties records were carried out using hard transducer.....	73
Fig. A2-8.The compressional velocity, bulk density, and magnetic susceptibility for the Lomonosov Ridge from LOMROGIII PC11 core plotted against depth (mbsf). The physical properties records were carried out using hard transducer.....	74

Fig. A2-4. The compressional velocity, bulk density, and magnetic susceptibility for the Lomonosov Ridge from LOMROGIII PC12 core plotted against depth (mbsf). The physical properties records were carried out using hard transducer.....75

Table1. Gamma ray calibration data.....18

Table2. Gamma ray calibration coefficient used in linear equation.....19

Table3. Calculated P-wave velocity using different core thickness and travel time scales.....28

Table4. Calculated bulk density using different core thickness and travel time scales....29

Table5. The confidence intervals and t-test values for average P-wave velocity, \overline{VP} is the average velocity for split and whole cores, $\overline{X}-\mu$ column is the differences between the average velocity of the whole and average velocity for each split core, Min and Max column represent the confidence interval of split cores, T-statistic value represents the calculated t-value from equation (21), and t-value is the value obtained from a standard t-table for normal distribution value with unknown standard deviation.....36

Table6. The confidence intervals and t-statistic values of density for the split and whole core samples. The symbols represent the same variables as in table 5 but in this case for the t bulk density values.....37

Table7. Calculated error introduced by 1 mm core thickness error expressed as a function of the measured data range for velocity and density of cores PC03, PC05 and PC09.....38

Table 8. The calculated differences, errors, and the corrections of the measured P-wave velocity, bulk density, and core thickness. The red values represent PC03, PC05, and PC09 that deviate from PC10.....39

TableA1-1. Depth. Length and locations for cores collected from Lomonosov Ridge during LOMROGIII.....63

Table A1-2. Core loggings notes for the measurements of split core samples using acoustic soft transducer.....64

Table A1-3. Core loggings notes for the measurements of split core samples using hard transducer.....65

1-Introduction

Physical properties of marine sediments represent one of the most widely used groups of evidence in understanding the composition and environmental conditions of sediments. High resolution measurements of physical properties can be used as proxies in paleoceanographic studies. Recent developments in the field of physical property measurement have shown an increased interest in using these properties in lithological identification, correlation, and the internal structures of sediments (Hamilton, 1970, 1971; Weber et al. 1997; Rider 2000; Breitzke, 2006). In marine geochemistry, physical properties serve as good indications of the porosity, permeability, and the composition of marine sediments (Rider 2000; Breitzke, 2006). In addition, these properties are of high interest in engineering applications, offshore surveying, interpretation of seismographic profiling (Rider, 2000; Breitzke, 2006; Moran et al. 2007), and paleoenvironmental and paleoclimatic studies (Weber et al. 1997; Breitzke, 2006).

Gamma ray attenuation provides a non-destructive and alternative method for determining bulk density which can be described as a mass of sample over the volume of sample.

$$\rho = \frac{m}{v} \quad (1)$$

where

ρ =bulk density (g/cm³)

m=mass (g)

v= volume (cm³).

Bulk density is influenced by many factors such as porosity of the sediments, particles grain size, compaction, and organic matter content. As bulk density is largely dependent on the porosity, the relation of these parameters can be used to estimate porosity from density and vice versa (Rider, 2000). For any discrete volume of sediments, the bulk density can be described by two phase components: the density of the mineral grains comprising the sediments (ρ_g) and the density of fluid filling the pore spaces in these sediments (ρ_f) (Hamilton, 1970, 1971; Weber et al. 1997; Rider, 2000; Breitzke, 2006). The bulk density can then be derived as follows:

$$\rho_B = \phi \cdot \rho_f + (1 - \phi) \cdot \rho_g \quad (2)$$

where

ρ_B = Bulk density g/cc

Φ =Porosity

ρ_f =Bulk density of fluid (g/cc)

ρ_g =Bulk density of solid (g/cc) (Best and Gunn, 1999).

The compressional velocity is calculated by measuring the travel time needed for a sound pulse to travel across the core. The first arrival of the sonic pulse represents the compressional wave whereby particles move perpendicular to the direction of the sonic pulse, followed by shear and Stoneley waves (Rider, 2000).

The compressional velocity is defined by:

$$V_p = \sqrt{\frac{K + \frac{4}{3}\mu}{\rho_b}} \quad (3)$$

where

V_p = the compressional wave velocity (m/s)

K = the bulk modulus (kN/m²)

μ = shear modulus (kN/m²)

ρ_b = bulk density (Mg/cm²) (Hamilton and Bachman, 1982, Moran et al. 2007).

The bulk modulus is defined as the ratio of applied pressure to the decrease of the volume in response to applied pressure

$$k = -\sigma_N / (\Delta V/V) \quad (4)$$

where

σ_N = the applied stress (N/m²)

$\Delta V/V$ = the decrease in the volume (Gassmann, 1951).

As the bulk modulus increases, the compressibility of material increases resulting in increasing the compressional velocity. On the other hand, the shear modulus is concerned with the deformation of material when it undergoes an applied stress. It is the stress divided by the strain

$$\mu = \tau / \theta \quad (5)$$

where

μ =shear module (N/m²)

τ = the stress (N/m²)

θ = the strain.

As the shear modulus increases, the elasticity of materials decreases (Gassmann, 1951).The compressional velocity is an elastic property of the mineral grains and water content in the pore space of the medium through which it propagates. The transmission

of the sound velocity is influenced by the effect of porosity and grain size on the elasticity of the sediments (Hamilton, 1970, 1971, 1972, 1980; Erickson and Jarrad, 1998; Moran et al. 2006, 2007). The empirical porosity-velocity relationship can be determined in the same way as that used in measuring the density-porosity relationship because the density is proportionally related to porosity (Hamilton, 1970).

Additionally, the temperature, salinity, and the pressure influence the propagation of sound velocity through the sediments. A change of 1°C temperature results in approximately 3 m/s increase in the velocity, while change of 1‰ salinity results in ~1 m/s change in velocity (Wiedicke and Weber, 1996). Further, other factors such as degree of fracturing (Kahraman, 2002; Paoletti, 2012), the presence of clay and water content (Wyllie et al. 1956; Tosaya and Nur, 1982; Han et al. 1986; Goldberg and Gurevich, 1989), depth and age of the materials (Paoletti, 2012) have also effect on the propagation of sound velocity through the sediments.

Among the factors influencing the compressional velocity and bulk density, porosity and grain size are considered the most important parameters. The influence porosity and grain size have on these properties is represented by their effect on the rigidity (bulk modulus and shear modulus). The relationship between porosity and elasticity of sediments was a main topic of many previous studies (Birch, 1961, 1966; Brace, 1965; Simmons and Brace, 1965; Christensen, 1966; Anderson and Liebermann, 1968). Marine sediments are totally saturated with water; a decrease in porosity reduces the influence of water on the bulk modulus. The compressional velocity is proportionally related to the stiffness of sediments. Thus increasing the bulk modulus causes an increase in the compressional velocity. Similarly, porosity influences bulk density of sediments, a decrease in porosity increases bulk density and vice versa (Sutton et al. 1957; Hamilton and Bachman, 1982; Moran et al. 2007).

Grain size influences the velocity by its influence on the bulk and shear modulus (Moran et al. 2007). This influence depends largely on the way in which particles comprising the sediments are arranged and shaped. In fine-grained sediments such as clay and silt, the intergrain contact decreases resulting in a decrease in the bulk modulus thus decreasing the velocity. In contrast, grain-to grain contact increases in coarse and sphere-shaped sediments causing an increase in the bulk modulus which in turn causes an increase in the compressional velocity (Hamilton, 1979; Breitzke, 2006; Moran et al. 2007; Schnack-Friedrichsen et al. 2010). The compressional velocity is also controlled by

increasing the overburden (effective) pressure. Increased effective stress decreases the porosity and increases the rigidity of sediments. Thus the compressional velocity and bulk density of the system increase (Hamilton, 1979).

The history of the laboratory measurements of the physical properties such as sound velocity began in the early 1950s (as described in Hamilton, 1970). The information on the compressional velocity was obtained from relatively inadequate datasets made by explosive seismology, and no practical records were obtained from fine and unconsolidated sediments of the seafloor. Early in the 1950s, several laboratories began to make empirical measurements of sound velocity in marine sediments including Cambridge, the Navy Electronics Laboratory (Hamilton, 1956; Hamilton et al. 1956; Shumway, 1960), and the Lamont Geological Observatory (Sutton et al. 1957; Nafe and Drake, 1957). Over the 1960s, the publishing of the data obtained from the laboratory measurements increased (Hamilton, 1963, 1965; Nafe and Drake, 1963; Ryan et al. 1965; Horn et al. 1968).

Over the last two decades, there was a sharp increase in using nondestructive techniques to measure acoustic velocity and other properties of sediments such as gamma ray attenuation and magnetic susceptibility. As these nondestructive measurement techniques have become more readily available and accurate, it is possible to correlate these measurements with grain size properties of sediments. Moreover, these systems are less time and cost consuming (Moran et al. 2007) in comparison with traditional manual measurements. For example, determining bulk density requires a known volume of sample to be accurately weighed, a process that is time consuming and destroys the sample.

Geotek's Multi Sensor Core Logger (MSCL) provides a variety of non-destructive sensors and logging tools for physical properties measurements. It represents a rapid, automated and provides high-quality measurements. It is a multipurpose technique because of its modular design that enables the user to adapt it to be used for individual testing requirements. The modern MSCL provides high resolution measurements of gamma ray attenuation bulk density, P-wave velocity, natural gamma, and magnetic susceptibility. The whole and split cores can be processed by the MSCL. In addition, it is capable of measuring cores at rate of 12m/h and down to 1 mm scale (Gunn and Best, 1998).

The goal of the studies for this thesis was to quantitatively evaluate the MSCL measurements of the compressional velocity and bulk density of split core sediments in particular those collected from the Lomonosov Ridge during expedition III cruise (2012/07/31-2012/09/13) using piston and gravity coring methods (Fig.1). The measurement was carried out using the Multi-Sensor Core Logger (MSCL) system. The quality of the P-wave velocity and bulk density measurements is directly related to the quality of the measured core thickness. Obtaining good measurements requires accurate knowledge of core thickness variation during the core logging process. When cores remain unsplit, the assumption is that the core fills the entire liner, and the core thickness does not vary. When cores are split, there is more variation in the thickness, and this needs to be directly measured.

The travel time of acoustic velocity across core was measured using two types of P-wave transducer (PWT): Oil filled (soft) Acoustic Rolling Contact (ARC) and stainless steel piston (hard) transducer (HT). Results from these two types of transducers are compared and an evaluation of the quality of the measured data is made. It is found that core thickness errors during split core logging significantly affect the magnitude of the velocity-density relationship. Finally, the variables influencing the density and velocity of central Arctic Ocean sediments are evaluated by comparing the results obtained from this study with those of three published models.

2. Study area

The core samples used in this study were collected from the Lomonosov Ridge in the central Arctic Ocean. The length of the Ridge is about 1700km (Kristoffersen, 1990) and the width varies from 50 to 70 km. It elevates about 3000m from the seabed. The ridge divides the Arctic Ocean into two separate basins: the Eurasian and the Amerasian basin (Jokat et al. 1992) and extends from the continental margin of Northern Greenland to the Laptev Sea shelf (Fig.1). The current activity and sediment movements are quite high over the summit of the Lomonosov Ridge (Morris et al. 1985). Quaternary Sediments from the region of the Lomonosov Ridge visited during LOMROGIII are hemipelagic silty clays composed mainly of >80% fine texture material (St. John, 2008).

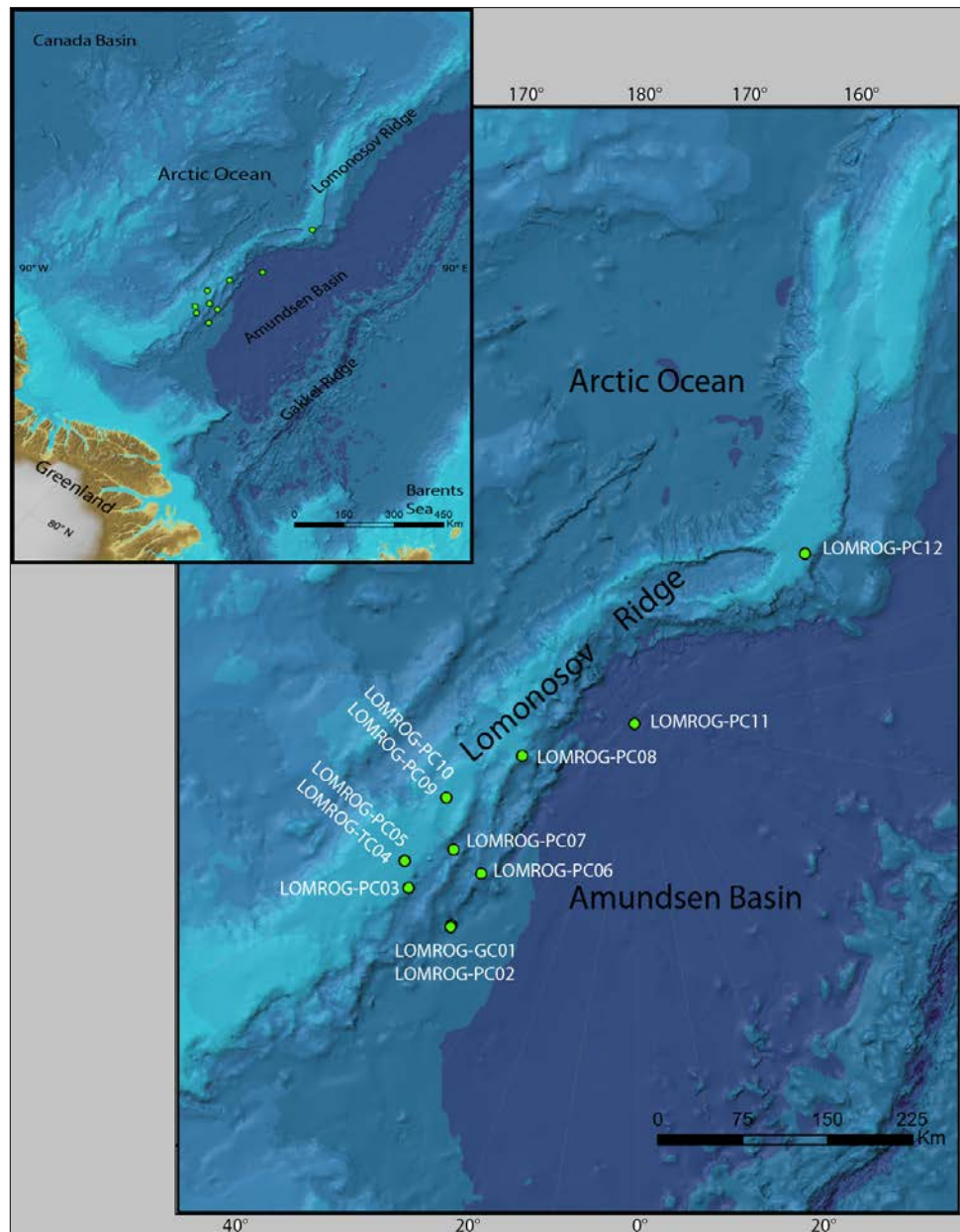


Fig.1. Map shows the Bathymetry of the central Lomonosov Ridge and the locations of the collected cores during the LOMROGIII cruise 2012.

3. Methods¹

Nondestructive, high resolution physical property measurements are made using the MSCL system. This system has a number of attractive characteristics: it has high resolution, it is rapid, continuous, and automated, and it yields high quality and accurate datasets that can be used in a broad spectrum of geological and geotechnical applications (Breitzke, 2006).

¹ The description of the techniques used in measuring the compressional wave velocity and bulk density and the features used is based on the instructions in the manual provided by the Geotek, 2000, and experimental notes documented during the logging of the core samples.

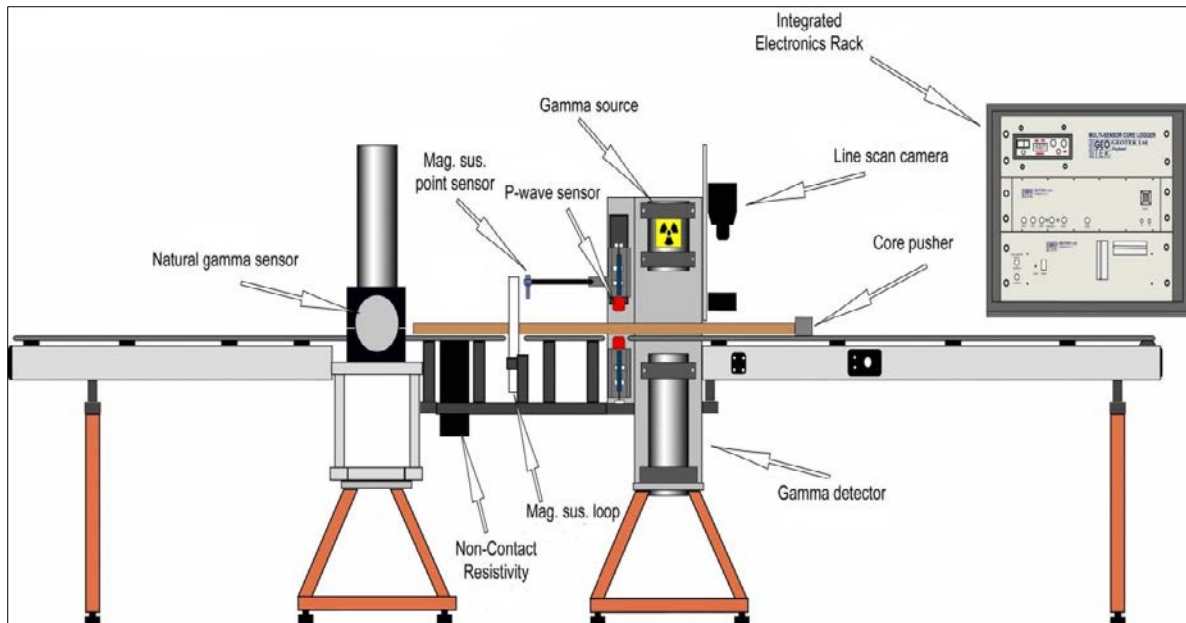


Fig.2. Typical vertical MSCL configuration used in split core logging modified after Geotek, 2000.

To date various methods have been developed and introduced to measure the physical properties of marine sediments. The (MSCL) is one of the most practical techniques used in this field, because it is a non-invasive, automatic, and rapid method. In addition, it gives high-resolution measurements on the centimeter-scale (Fig.2).

The versatile design of the Multi Sensor Core logger instrument is presented in figure 2. For split core logging, the configuration of MSCL is vertical (Figs.3 and 4). Throughout the split core logging process, the core samples move horizontally by means

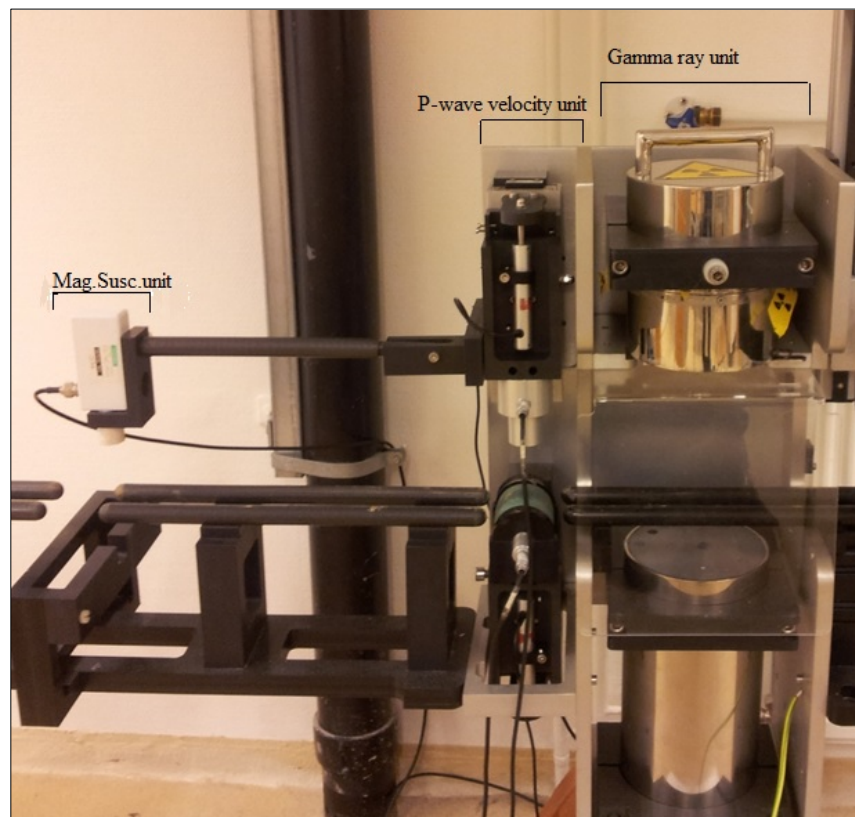


Fig.3. The vertical configuration of the compressional velocity, bulk density, and magnetic susceptibility units used in split core logging.

of a core pusher. This pusher transfers core samples across diverse stationary sensors by a horizontal motorized core conveyor system driven by a stepper motor.

The sensors used in this system can be mounted vertically or horizontally on the central stand either within or around the conveyor system. These sensors are controlled by a central electronic rack. The configuration of the MSCL is horizontal when logging the whole core.

The design of the MSCL system enables measuring both the whole and split core samples encased in plastic liners and exposed rock samples as well. On the system at Stockholm University the MSCL currently is used to measure P-wave velocity, gamma ray attenuation,

magnetic susceptibility, core thickness, and core imaging. The length of the MSCL system is about 4 m. The maximum length of a section that can be logged in this system is up to 150 m.

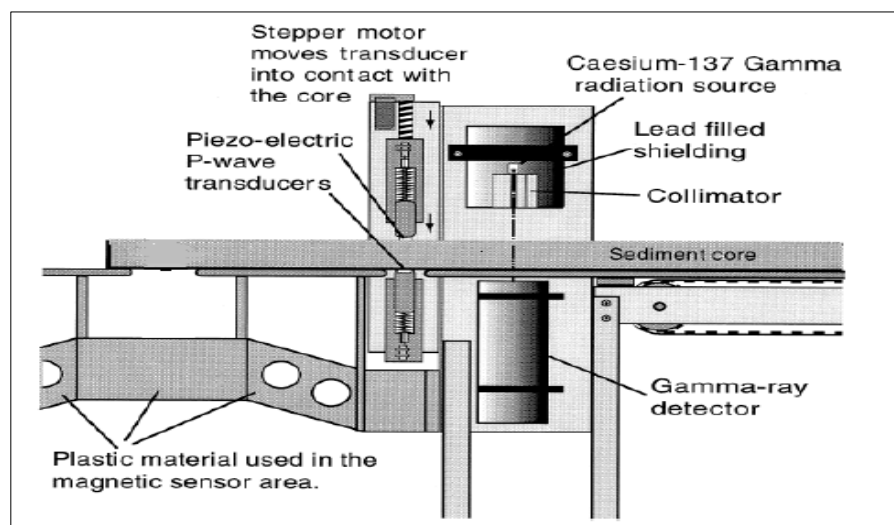


Fig.4. Schematic view of the vertical configuration of the P-wave velocity and gamma ray sensors used with the MSCL modified after Gunn and Best, 1998.

3.1 Sample preparation

The core logging was made on about 60 m of cores collected from 12 sites on the Lomonosov Ridge during the LOMROGIII cruise (2012/07/31-2012/09/13) using piston and gravity core methods (Table. A1-1). The cores were cut into 1.5 m sections, and then split into a working half and an archive half. Before logging, the samples were left to equilibrate to room temperature to obtain accurate measurements mainly for P-wave velocity and magnetic susceptibility. During the logging process, the samples were wrapped in plastic. After the measurements, the half-cores were kept in plastic tubes at 4°C.

3.2 Bulk density measurements

Bulk density is an important indicator of several sedimentological factors such as porosity, mineralogy, and can be used to define local acoustic impedance, correlate data from different locations and aid in seismographic modeling (Blum, 1997).

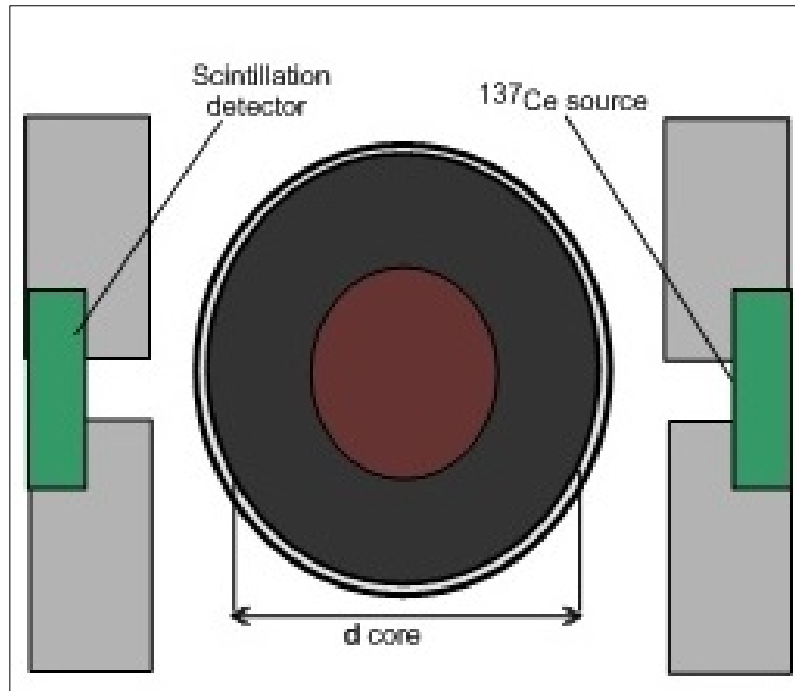


Fig.5. Schematic view of gamma ray logging modified after Geotek, 2000.

3.2.1 Principle of operation

Bulk density can be measured using gravimetric, volumetric, and the MSCL systems. The measurements are occasionally referred to as gamma ray attenuation porosity evaluator (GRAPE). The determination of gamma density is carried out by measuring the attenuation of gamma rays emitted from a constant source and detected on the other side of the core. Usually Caesium-137 (¹³⁷Cs) is used as gamma ray source with energies mainly at 0.662 MeV (million electron volts). The choice of the ¹³⁷Cs as a gamma ray source is related to its half-life of 30.2 years which provides a good balance between the level of used energy (0.662 MeV) and operating time. According to (Geotek, 2000), the basic principle in measuring bulk density depends on the Compton scattering and attenuation of gamma rays. A thin beam of gamma ray (¹³⁷Cs) is transmitted through a core. When gamma beams pass through the core, some of them are absorbed and scattered and undergo a partial loss of energy and direction. The scintillation counter detects only gamma beams that pass across the core without energy and direction loss.

The detector consists of a scintillator and integral photomultiplier tube located in the center of the housing (Fig.5). Gamma ray attenuation is dependent on the source intensity, the sediment bulk density, the thickness of sediments through which gamma rays are transmitted and the Compton attenuation coefficient (Fig.6). The intensity of an

attenuated gamma ray is mostly determined by identifying the intensity of gamma ray source and the intensity of gamma ray beam when passing across the core without direction and energy loss. The intensity is used as a proxy of gamma density and can be calculated according to equation (6).

$$I = I_0 \cdot e^{-\mu\rho d} \quad (6)$$

where

ρ = sediment bulk density(Mg/m³)

μ = the Compton attenuation coefficient (m²/Mg)

d = the sediment thickness (m)

I_0 = the gamma source intensity (counts/sec)

I = the measured intensity through the sample (counts/sec).

When photons pass through the core, they attenuate and undergo a partial loss of energy through a process known as Compton scattering. During this process, some of the photons are absorbed and scattered when they collide with the electrons in the core section. Only the photons that pass through the core without energy and direction loss are detected by the scintillation counter. The derivation of bulk density can be inferred from the measured density of electrons (Blum, 1997).

3.2.2 Calibration and processing

Owing to difficulty in determining the Compton mass absorption coefficients of the sediment minerals and water, an empirical approach is used to calibrate and obtain

appropriate bulk density measurements. In this technique a two-phase system model is suggested for sediments and rocks representing the mineral and interstitial water respectively. An aluminum standard is used to calibrate the system. Because of the similarity in

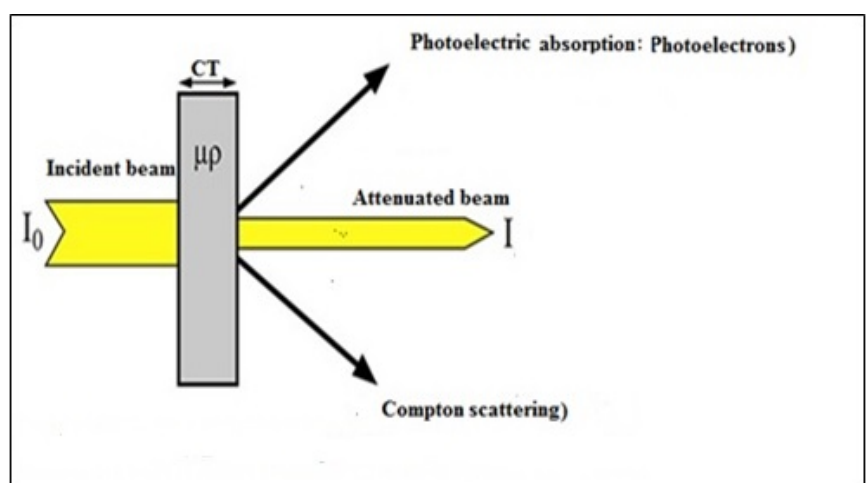


Fig.6.Schematic diagram of gamma ray and core thickness.

the attenuation coefficient of aluminum and ordinary minerals, aluminum is used as mineral phase in the form of different cylindrical pieces of different diameters surrounded by pure water.

Gamma Calibration	Al Thickness (cm)	Average Density (g/cc)	Ave Den * Thickness	Intensity (cps)	Ln(cps)
90 second count time	3.55	2.55	9.97	6435	8.76
Internal Thickness =3.90 cm	3.05	2.33	9.11	6774	8.82
Aluminum Density =2.70 g/cc	2.55	2.11	8.26	7163	8.87
Water Density =1.00 g/cc	2	1.87	7.32	7552	8.92
	1.55	1.67	6.55	8004	8.98
	1	1.43	5.61	8479	9.04
	0.55	1.24	4.84	8985	9.10
	0	1	3.9	9426	9.15

Table1. Gamma ray calibration data.

The bulk density of aluminum (2.70 g/cm³) is represented by the first element with porosity 0%, while the bulk density of pure water at laboratory temperature (1.00g/cm³) is represented in the last element which has 100% porosity. In the calibration process, the gamma counts for all aluminum pieces and water were measured with 90 sec as the count time (Table.1).

The average density of aluminum and water is calculated using equation (7).

$$\rho_{av} = \left(\frac{di}{D}\right) * \rho_{Al} + \frac{D-di}{D} * \rho_{water} \quad (7)$$

where

D= total thickness (m)

di= thickness of aluminum (m)

ρ_{Al} = density of aluminum(Mg/m³)

ρ_{water} = density of water(Mg/m³).

A linear or 2nd order polynomial can be used to define the relationship between density and the number of gamma rays that pass through the standard. Table2 presents

the intercepts, slopes, and the coefficients of determination used to calculate bulk density by the linear equation in this study.

These coefficients are substituted later in equation (8) to convert cps to density value.

$$Y = Ax^2 + Bx + C \quad (8)$$

where

y= ln (Intensity)

x=density* sediment thickness.

To obtain the bulk density for the core sample, equation (8) can be substituted for Y by the equation (9) as follows:

$$\ln(\text{counts}/\text{ts}) = (A * (\rho_{BC} * \text{ds}))^2 + B * (\rho_{BC} * \text{ds}) + C \quad (9)$$

where

ρ_{BC} = the bulk density calculated from gamma account (Mg/m³)

A, B, C= constants

ts= The sampling period (sec)

Counts= the actual measured counts on the sample

ds= the actual sediment thickness (m).

The coefficients A, B, and C in equation (9) are determined from linear regression during calibration. Either linear or 2nd order polynomial relationships are used to calibrate the bulk density. The A value is set to zero when using the linear relationship. A linear model enables fixing the intercept while fitting the points and examining the correction between two variables. However, the formula in a polynomial model contains the root square and requires using the quadratic formula to be solved.

Core	m	b	R ²
PC03	-0.0629	9.4392	0.999
PC05	-0.0629	9.4392	0.999
PC06	-0.0629	9.4392	0.999
PC07	-0.0629	9.4365	0.998
PC08	-0.0629	9.4365	0.998
PC09	-0.0625	9.4494	0.997
PC11	-0.064	9.4051	0.998
PC12	-0.0625	9.4494	0.997
PC10	-0.0655	10.572	0.99

Table2. Gamma ray calibration coefficients used in linear equation.

The calibration process for the split core is carried out by placing the aluminum pieces of different thicknesses below the level of distilled water between gamma ray source and detector (Fig.7). The equation used to calculate corrected gamma ray counts is

$$\text{Corrected (cps)} = \text{Raw counts}/\text{time} \quad (10)$$

This equation is used to normalize the detected counts. The quality and resolution of gamma density are influenced by the time needed to account for gamma ray attenuation; therefore the integration of gamma counts has to be performed at the appropriate time interval. Using a low count time (e.g.1 sec) results in increasing the deviation of true gamma ray values from the mean gamma density value, and provides inaccurate bulk density measurements. In contrast, using a high value of counting time (e.g.90 sec) provides good balance between the counting time and the accuracy of the measured bulk density. The occurrence of voids along the split core caused by gas or air reduces the quality of estimated density.

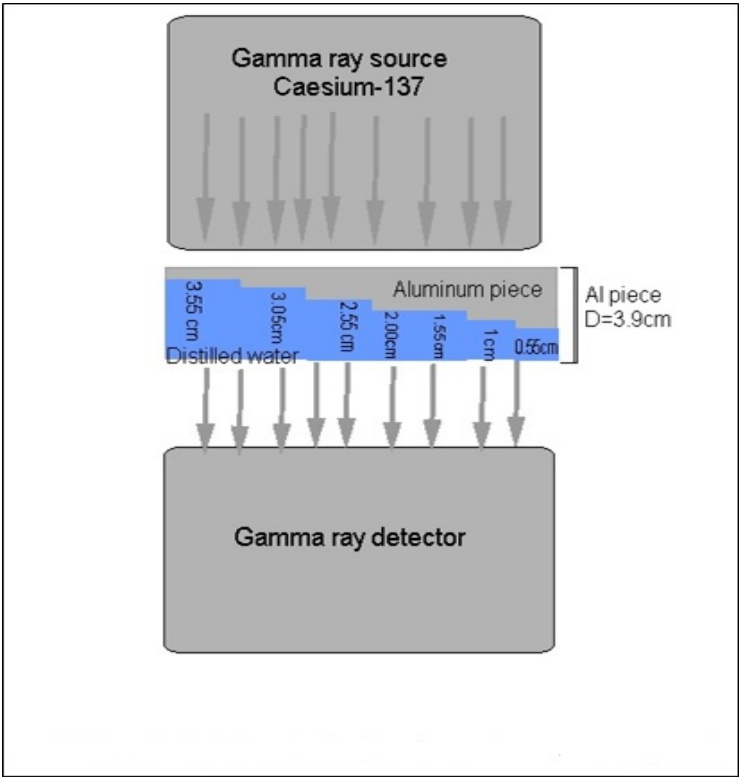


Fig.7. Schematic illustration of calibration piece and gamma ray components.

During the calibration process, the calculated densities of different aluminum pieces and water are correlated with the logarithm of gamma rays that pass through the calibration piece (Fig.8). A graph of the average density multiplied by the core thickness (internal diameter of the liner) versus the natural logarithm of normalized gamma counts is used to obtain the calibration curve.

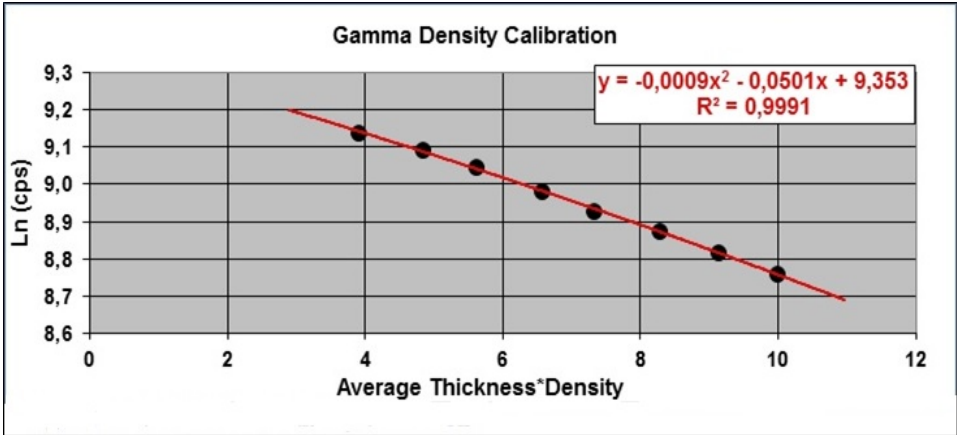


Fig.8. Schematic view of gamma ray calibration.

3.3. P-wave velocity measurements

P-wave velocity is widely used to indirectly determine the porosity and permeability of sediments. Velocity provides a good indicator for identifying source rocks and the composition of sediments. Combined with the density log, it can be used to produce the acoustic impedance (the product of acoustic velocity and density) which can be used to construct a synthetic seismic profile (Blum, 1997).

3.3.1 Principle of operation

A short P-wave signal (230 kHz-500 kHz) is produced by an ultrasonic pulse transmitter. This signal excites the piezo-electric element contained in the transmitter and a P-wave at 500 kHz is launched. The produced pulse is propagated through the core and is detected by the receiver on the opposite side. After passing through the sample, the propagated wave is detected by the receiver and improved by an automatic gain control (AGC). The total travel time (TOT) of the pulse from the transmitter through the core and to the receiver is measured using pulse timing software. Specialized software automatically picks the arrival time of the P-wave pulse. The accuracy of this automatic picking is influenced by the strength (amplitude) of the received P-wave. The velocity is calculated by dividing the sediment thickness by the travel time

$$V_p = \frac{d}{t} \quad (11)$$

where

d=travelled distance (m)

t=travelled time needed to pass d (sec).

3.3.2 Device

In the MSCL, the compressional velocity unit consists of two different types of the P-wave transducers (PWT) and two rectilinear displacement transducers (DT). This unit is mounted on the central stand of the MSCL. In this study, two types of the PWT were used: 1) the ACT and 2) the HT (Fig.9). In both transducers, the essential part is a piezoelectric crystal included in the stainless steel container and sheathed in epoxy resin. In HT, the epoxy resin is in direct contact with the sediment surface. In the ACT the element is surrounded by oil in a rotatable, soft, and deformable diaphragm. When subjected to an applied electrical signal this piezoelectric crystal deforms and generates an ultrasonic vibration. The travel time of the p-wave pulse through the rubber and oil in the transducer, core liner, sediments, and finally through the rubber and oil in the receiver is measured with an accuracy of approximately 50 ns.

The orientation of the P-wave transducers depends on the configuration of the system. For split core logging, the orientation is vertical. In order to obtain excellent ultrasonic connect between the core and the upper transducer, both PWT are spring loaded to be pushed



Fig.9. View of stainless steel piston (hard) transducer (left), acoustic filled oil rolling (soft) transducer (right).

against the core. For a piston (hard) transducer which is only used for split core logging, this coupling can be improved by wetting the lower end of transducer or the surface of the core with water. The soft transducer does not need to be moistened because it has already good connection with the core due to the oil-filled diaphragm.

When logging the split core, the receiver is normally placed within the conveyor path and directly touches the lower part of the core section. While the upper transducer is placed on the upper vertical slide and can be moved up and down by means of a stepper motor. During the logging process, the upper surface of the split core section is wrapped with plastic and wetted to avoid contamination of the upper P-wave transducer. The logging notes for the split core obtained from using two types of the PWTs are displayed in tables A1-10 and 11.

The upper transducer is lowered to the surface of the core using the vertical stepper motor. Both P-wave transducers work as spring-loaded pistons against the core section. The pressure exerted by the transducer on the sediment surface is influenced by the load of the spring. In some instances this can deform the upper surface of the core. In the vertical mode the spring can be removed from the upper transducer housing to reduce the risk of core disturbance.

In the MSCL, The detection of the P-wave signal requires that the amplitude of the processed signal must be above a minimum threshold level (Fig.10). A good coupling between the PWT and the core surface provides high amplitude value. In contrast, when the connection is bad, the sonic pulse is either scattered in air or reflected to the transmitter.

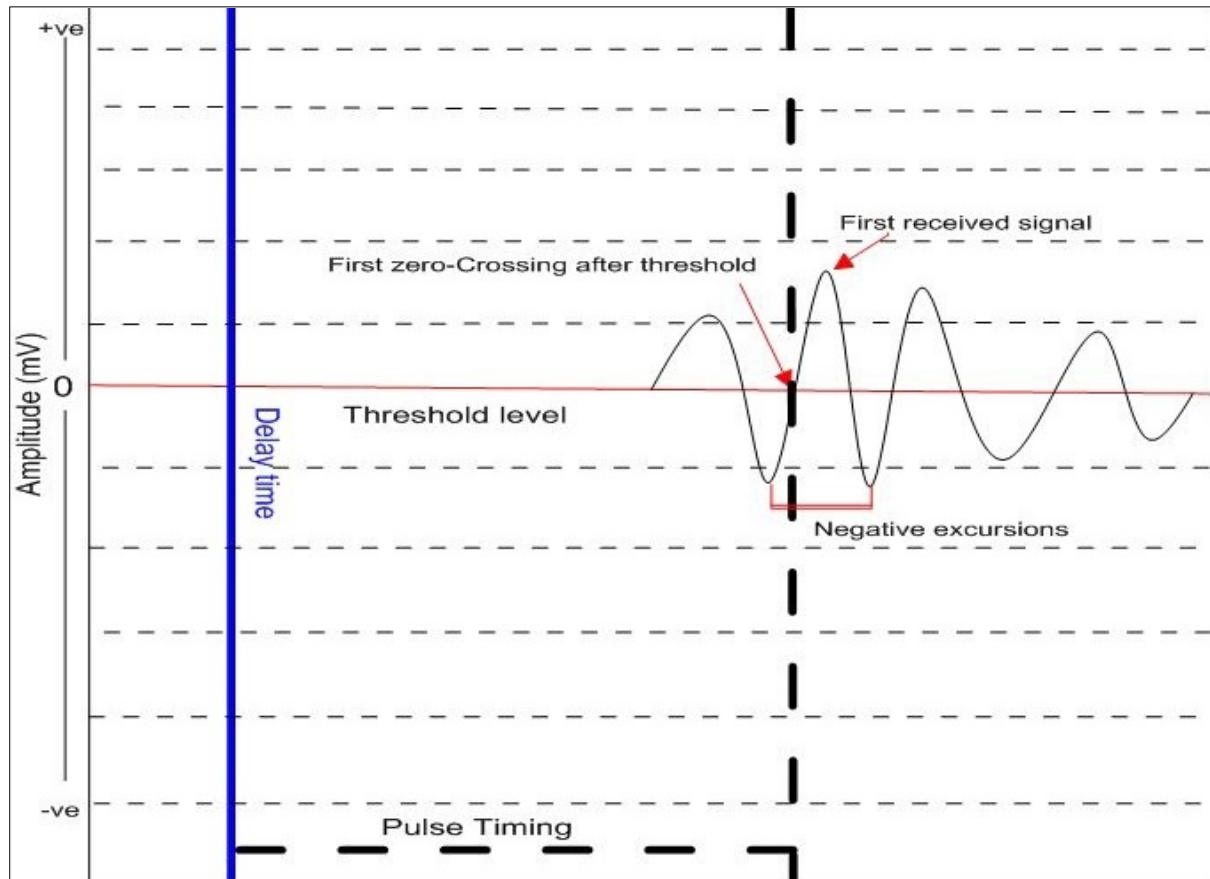


Fig.10.Pulse timing window for P-wave level system.

3.3.3 Calibration and processing

The compressional velocity through the sediments is calculated from

$$V_P = \left(\frac{X}{100}\right) / \left(\frac{TT}{1000000}\right) \quad (12)$$

where

X=the sediment thickness (cm) inside the core liner as measured

TT=the pulse travel time in the sediment (μsec).

The same plastic liner containing aluminum pieces filled with water is used to calibrate the P-wave velocity. When the upper transducer touches water surface, the travel time (TOT) of P-wave pulse through water is measured. The measured total travel time (TOT) presents as

$$TOT = TT - PTO \quad (13)$$

where

TOT is the total travel time from transmitter to receiver (μ sec)

TT is the travel time through the sediments (μ sec). It is determined by subtracting the travel time offset (PTO) from the total travel time (TOT)

PTO= the P-wave travel time offset including travel time through liner, transducer, receiver, and membrane (μ sec).

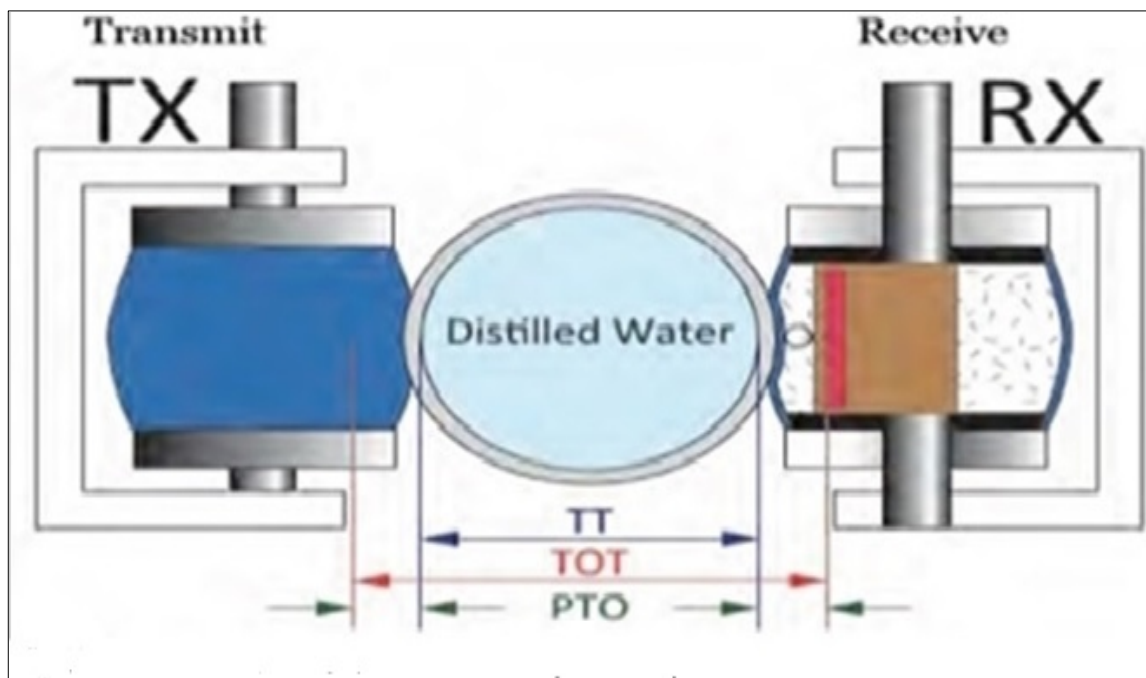


Fig.11. Schematic view of the P-wave calibration system after Geotek, 2000.

To calibrate the system, the delay time of the travelled P-wave pulse is measured including : (a) the time taken by P-wave to travel through core liner walls, (b) time needed to travel the pulse across a distance between transducers faces and the active elements, (c) delay resulting from taking a point on the wave shape equivalent to about 1 cycle after its launching, and (d) the system circuitry delay resulting from the time taken by the transmitter pulse to reach the active elements and vice versa (Fig.11). This time is influenced by core liner thickness and the type of core (split or whole core) being logged.

Temperature is an important factor affecting the quality of obtained P-wave velocity measurements, therefore the measured temperature should be taken into account when calibrating the system. Temperature measurements are performed using a standard

Platinum Resistance

Thermometer (PRT). This probe is coupled with a long lead that can be inserted into water in the standard calibration liner or the end of each core section. The recorded temperature values are

later inserted into the calibration file to provide

accurate velocity measurements for sediments being logged (Fig.12).

The equations used to account for different sound speed through the sediments and water are

$$VP = (1000 * X)/TT \quad (14)$$

$$TT = TOT - PTO \quad (15)$$

where

VP=p-wave velocity (m/s)

X=sediment thickness (processed data, cm)

TT=sediment travel time (μ sec)

PTO= p-wave travel offset (μ sec)

TOT= total travel time (raw data, μ sec).

3.4 Core thickness measurements

Accurate measurements of core thickness are critical for calculating bulk density and compressional wave velocity. In the MSCL system, core thickness measurements are carried out by measuring the distance taken by the displacement transducers mounted on the PWTs during core logging. For the split core, the configuration of MSCL is vertical so the upper (DT) touches the upper PWT at the top end, whereas the lower (DT) touches the lower PWT at the bottom end. This coupling enables each displacement transducer to follow the movement of each PWT during the core logging process. As a result, the core thickness is provided by equation (16)

$$Ds = dref - dw + \frac{CTD}{10} \quad (16)$$

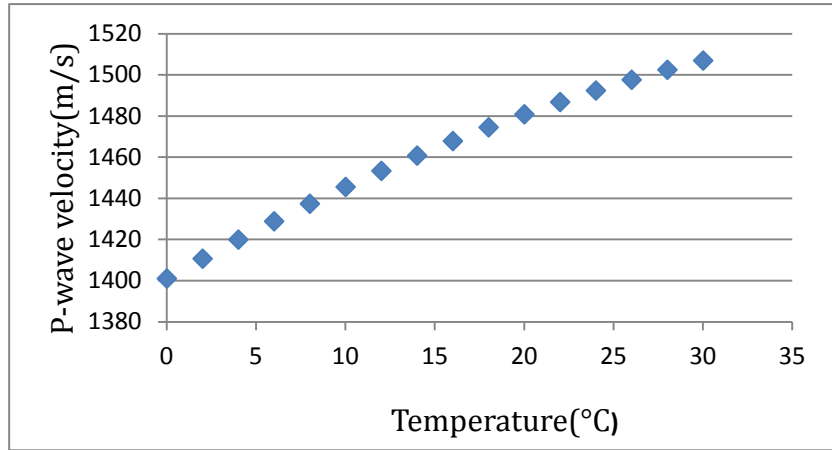


Fig.12. Temperature dependence of P-wave velocity through distilled water based on equation of Leroy (1969).

where

D_s = core thickness of the sample (cm)

d_{ref} = reference core thickness (cm)

CTD= deviation in core thickness (mm)

d_w = total wall thickness (cm).

Before logging each core, a reference thickness is set by placing a semi-cylindrical aluminum piece between the transducers. This reference piece is slightly thinner than the split cores with a thickness of 3.9 cm (Fig.13). When setting the reference core

thickness (RCT), the motion of upper P-wave transducer is controlled manually by moving the transducer down until it just touches the surface of aluminum piece. During logging, a deviation of the sediment thickness above the RCT is measured by the displacement transducers. The use of the different types of the PWT can provide different core thickness measurements.



Fig.13. A semi cylindrical aluminum piece used as a reference core thickness point.

Reasons for this are 1) the soft-filled oil may deform when touching the surface of the core, resulting in inaccurate core thickness measurements. In contrast, the hard transducer does not suffer from this problem since it touches the surface of the core directly and thus provides more accurate core thickness measurements (Fig.14).

Another possible explanation for the difference can be attributed to user errors in selection of the reference point on the core surface. The estimation of this point is usually done visually and thus it varies between the cores. A third potential error in core thickness measurements is due to the fact that the motion of each P-wave transducer is affected by the spring mounted within the plastic housing. The load of this spring influences the pressure exerted by the transducers on the sediments surface

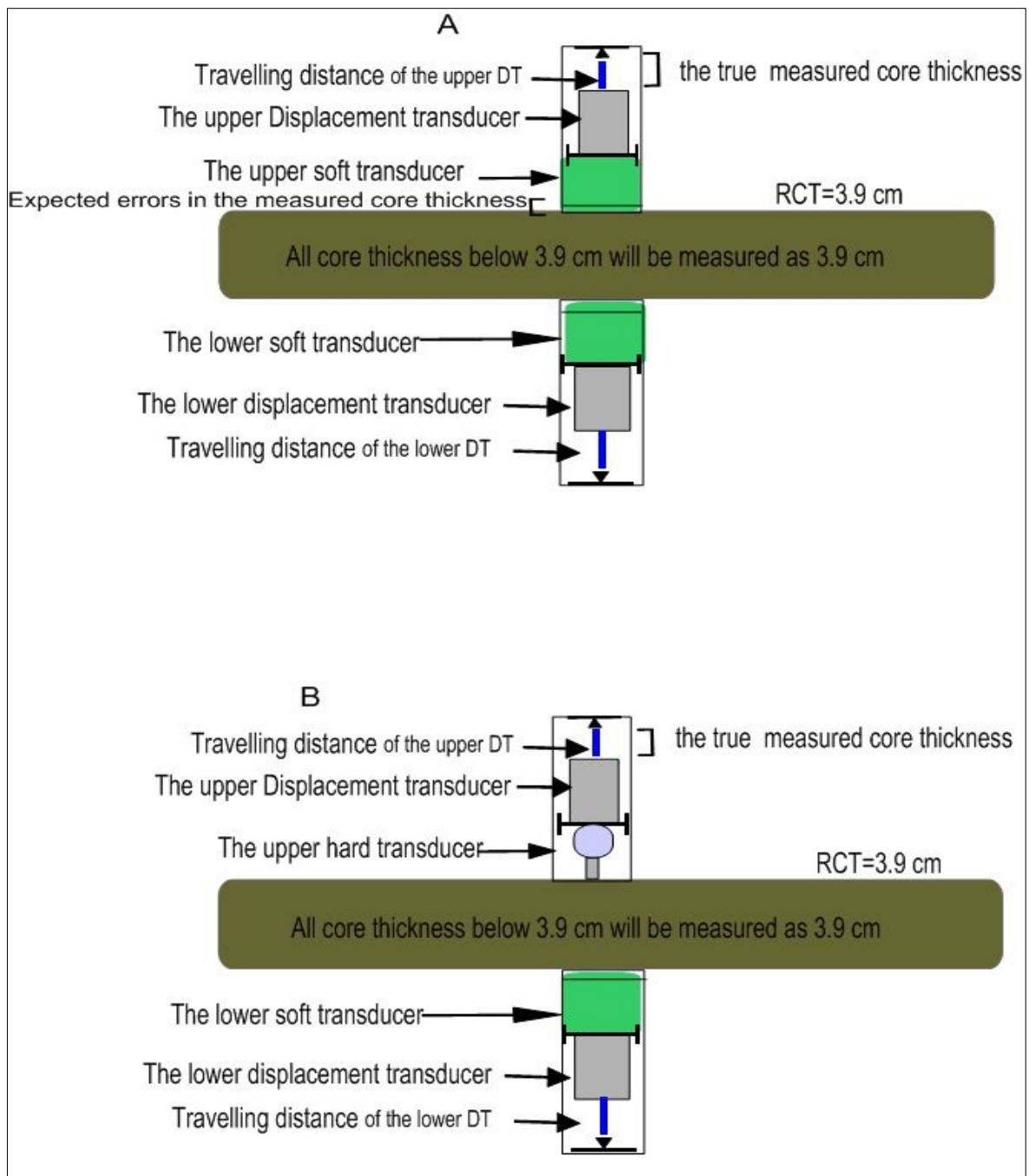


Fig.14.Schematic illustration of the core thickness measured using ACT (A) and HT (B) with illustration of core thickness errors expected when using soft transducer.

particularly when using the acoustic rolling transducer. In soft sediments, the transducer may press into the sediments instead of causing the displacement transducer to retract.

3.4.1 The quantitative influence of core thickness errors on the P-wave velocity and bulk density measurements.

One of the most complicated problems face split core logging is that the core samples are contained in different sections with different thicknesses .In addition, the split surface is not always smooth along the length of the section. If not accurately measured, these

variations in core thickness result in wide-ranging deviations in the quality of measured P-wave velocity and bulk density.

To better understand the influence of thickness errors on the measured velocity and density, a quantitative evaluation was conducted. For velocity measures, different travel times (TT) (e.g.28, 29, 30 μ sec) were used to calculate p-wave values for hypothetical cores with thicknesses ranging between 3.2 to 4.6 cm. (Table.3). On average, a change of 1mm core diameter results in an increase in the P-wave velocity of approximately 34 m/s. The trend of P-wave values shows a linear relationship with core thickness and the P-wave velocity (Fig.21)

TT (μ sec)	CT (mm)	Calculated Vp(m/s)	TT (μ sec)	CT (cm)	Calculated Vp(m/s)	TT (μ sec)	CT (cm)	Calculated Vp(m/s)
28	3.2	1142	29	3.2	1103	30	3.2	1066
	3.4	1214		3.4	1172		3.4	1133
	3.6	1285		3.6	1241		3.6	1200
	3.8	1357		3.8	1310		3.8	1266
	4.0	1428		4	1379		4	1333
	4.2	1500		4.2	1448		4.2	1400
	4.4	1571		4.4	1517		4.4	1466
	4.6	1642		4.6	1586		4.6	1533

Table 3. Calculated P-wave velocity using different core thickness and travel time scales.

Similarly, using the average linear relationship between gamma ray attenuation and core thickness (Table 4), it is found that a change of 1 mm core thickness results in~ 0.05g/cc change in bulk density (Fig.22). In summary, the results of this test indicate that 1) erroneous core thickness measurements are proportionally related to the compressional velocity and inversely related to the bulk density. Therefore it is expected that a thickness error would cause an increase in bulk density and a decrease in the compressional velocity or vice versa. 2) Small errors in core thickness (1-2 mm) can potentially introduce significant errors in measured density and velocity.

AG (cps)	Ln (cps)	CT (cm)	ρ_B (g/cc)	AG (cps)	Ln (cps)	CT (cm)	ρ_B (g/cc)	AG (cps)	Ln (cps)	CT (cm)	ρ_B (g/cc)
7500	8.922	3.2	2.68	8000	8.987	3.2	2.33	8500	9.047	3.2	2.15
		3.4	2.52			3.4	2.19			3.4	2.03
		3.6	2.38			3.6	2.07			3.6	1.91
		3.8	2.25			3.8	1.96			3.8	1.81
		4	2.14			4	1.86			4	1.72
		4.2	2.04			4.2	1.78			4.2	1.64
		4.4	1.94			4.4	1.69			4.4	1.56
		4.6	1.86			4.6	1.62			4.6	1.50

Table 4. Calculated bulk density using different core thickness and travel time scales. The data symbols in column AG represent the attenuated gamma rays, CT (core thickness), Ln (logarithm of gamma ray value), and ρ_B is calculated bulk density.

4. Results

4.1 Overview

The results obtained from the preliminary measurements of physical properties on the split core using the MSCL system are displayed in (Figs. 15-A, B, and 16). In these analyses, the P-wave velocity measurements were carried out using two types of PWTs: ACT (Fig.15. A) and HT (Fig15.B). For the whole cores, the physical properties were measured on core PC10 (Fig.16). The purpose of using PC10 as a reference is because this core shows more accurate and consistent core thickness measurements. From the data in figure15-A, it is apparent that the ranges of the compressional velocity and bulk density from the ACT data are greater than that from the HT data (fig.15-B). This variation is attributed to the inaccuracy in core thickness measurements caused by the ACT.

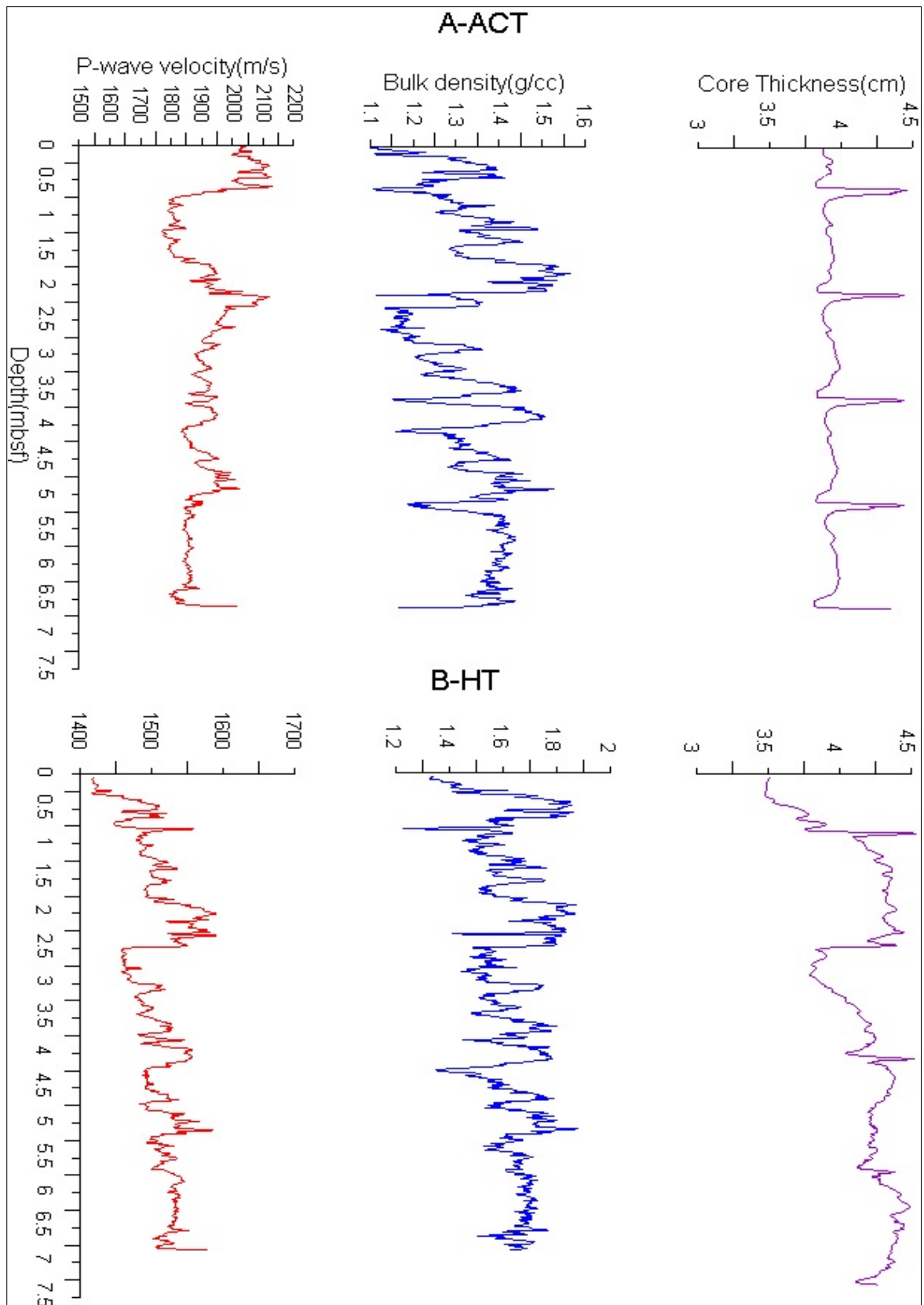


Fig.15. Sediment physical properties and core thickness of PC07 from Lomonosov Ridge measured in the upper ~7 m below seafloor using the HT (A) and ACT (B).

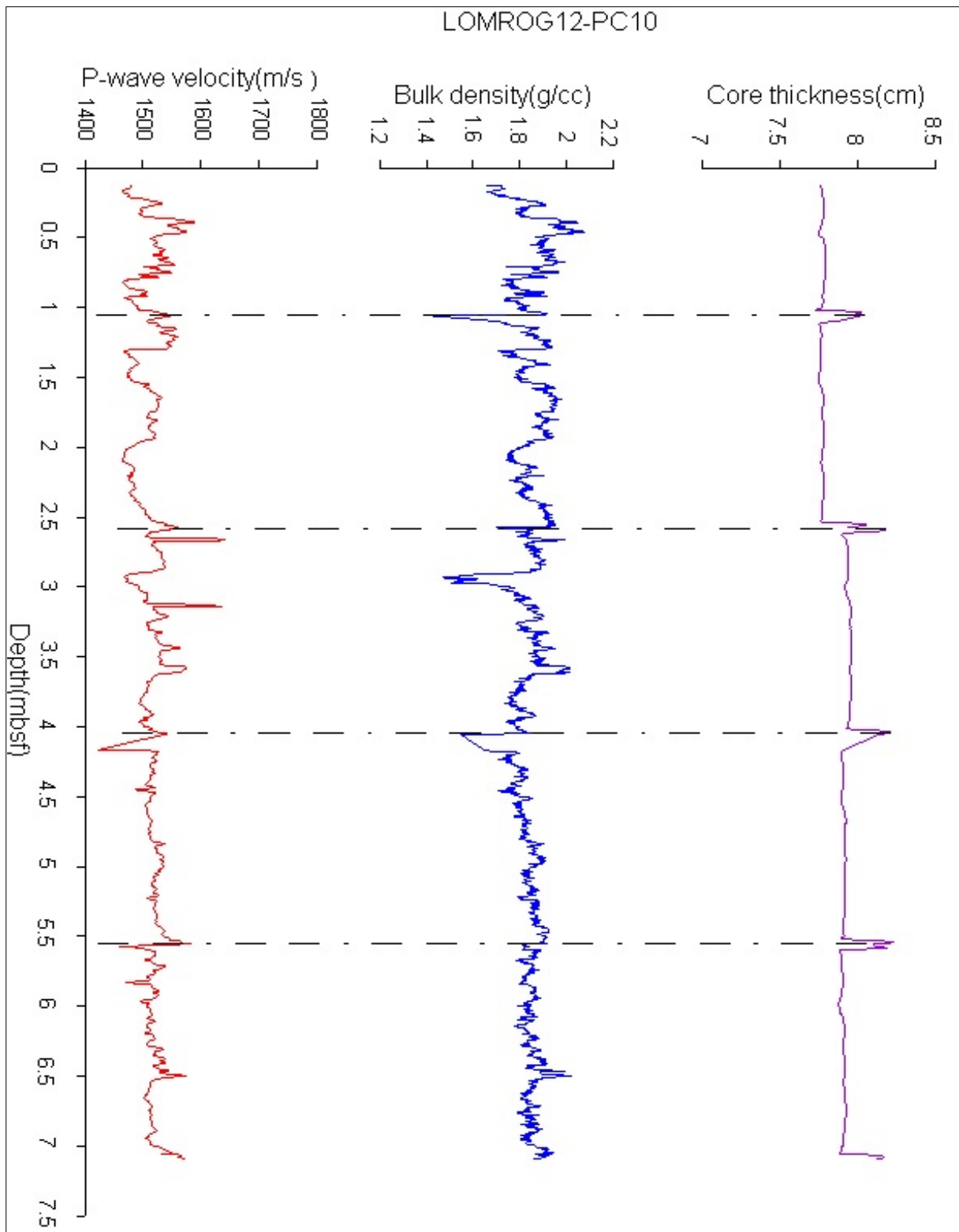


Fig.16. Sediment physical properties and core thickness of PC10 from the Lomonosov Ridge measured in the upper ~7 m below seafloor.

4.2 Comparison of ACT and HT data

To assess the influence of core thickness deviation on the measured P-wave and bulk density values, the results from eight split cores were compared and contrasted with whole core measurements on PC10(Fig.17). Since PC10 was measured as a whole core it was used as a reference core to avoid bias in core thickness errors.

The results illustrate that there is a clear tendency towards higher density and P-wave velocity for individual cores, but scatter between them is huge when using the ACT (Fig.17). This finding supports the previous observations which indicated that the

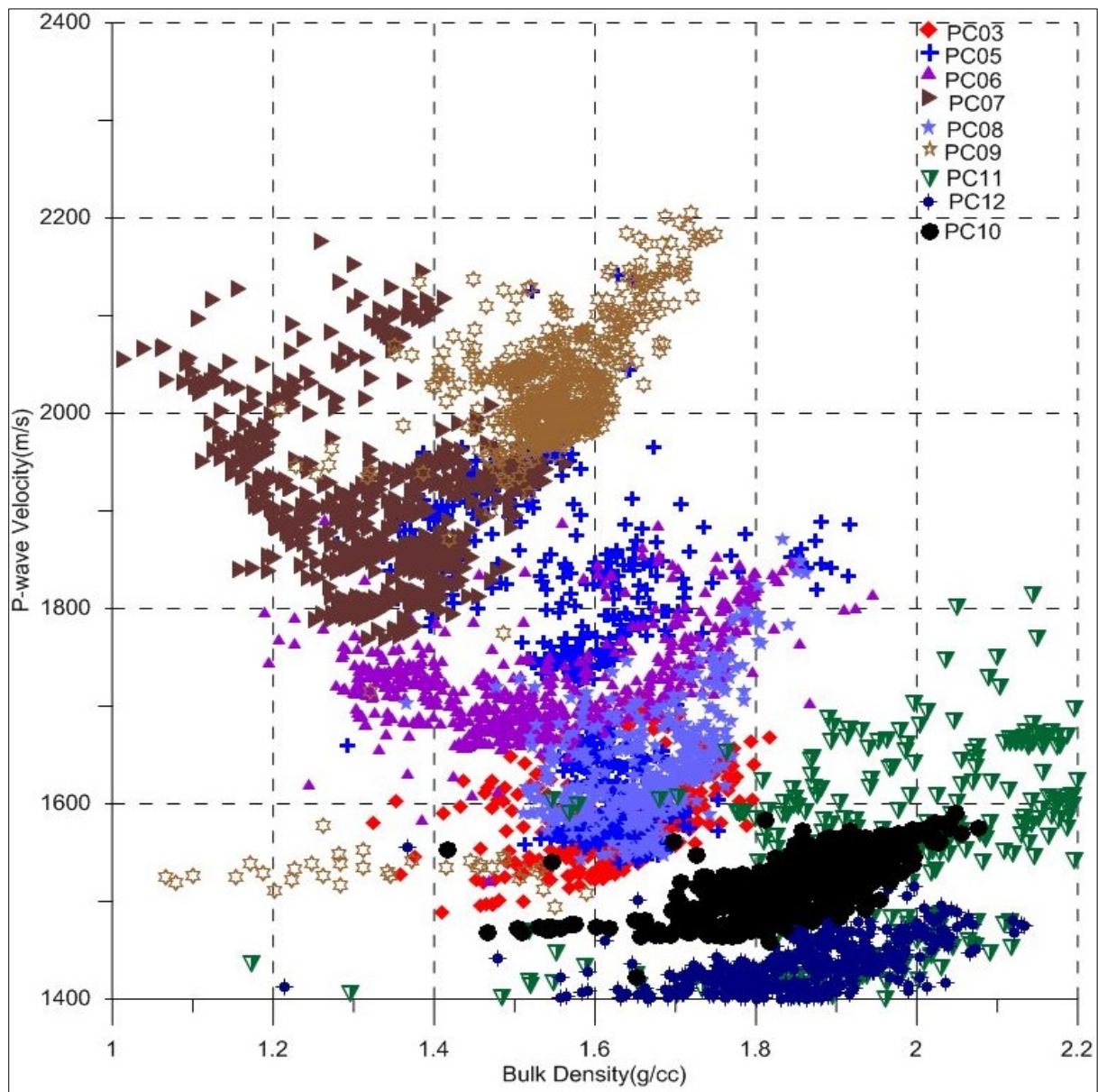


Fig.17. Cross-plot velocity-density relationships of split and whole cores from Lomonosov Ridge measured using the acoustic oil-filled rolling (soft) transducer.

expected core thickness errors are higher when using the oil-filled PWT. When the soft membrane of this transducer presses against the sediments, it can deform and this

causes errors in the measured core thickness. In addition, the load of the upper spring encased in the plastic housing affects the stress exerted by the soft transducers on the core. As the lower end of the upper soft transducer touches the core surface, the sediment surface can be disturbed resulting in inaccurate core thickness measurements along the core section. Despite the fact that the expected errors in the measured core thickness can be as small as 1-2 mm, they would result in deviations and yield unrealistic velocity and density measurements. As a result, this method showed a huge shift in the velocity and density values for some split cores in comparison with the PC10 data.

In comparison to the ACT data, the cross-plot relationship between P-wave velocity and bulk density using the hard transducer also show a clear tendency towards

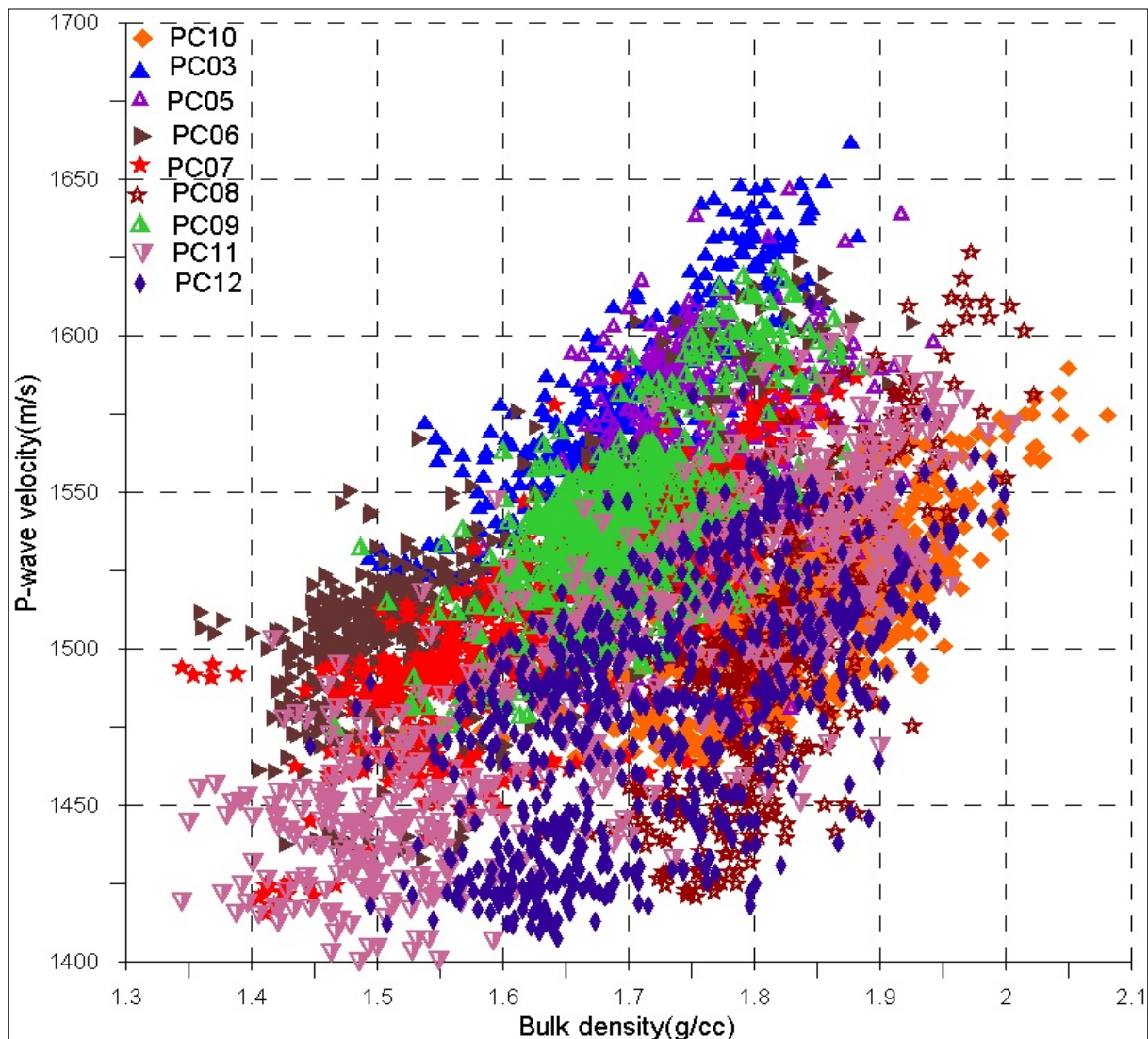


Fig.18 Cross-plot velocity-density relationships of split and whole cores from Lomonosov Ridge measured using the piston (hard) transducer.

increasing p-wave velocity and bulk density for individual cores but with far less scatter between cores than that observed in the ACT data (Fig.18). All hard transducer data showed a more consistent p-wave velocity-density relationship, except PC03, PC05, and PC09 cores, which are more offset from the PC10 data.

A possible explanation for this deviation is also attributed to the effect of core thickness errors on the calculated velocity and density. These errors can be attributed to the visual mismatch in selection of the reference point on the core surface. However, the trend of other split cores showed less increase and less average scattering in the P-wave velocity and bulk density in comparison with the reference core, indicating good evidence that hard transducer provides more accurate measurements than the soft one.

4.3 Statistical analysis of differences in density and velocity

The average P-wave velocity and bulk density for each core were scattered with more pronounced offset from the main trend in the PC03, PC05, and PC09 cores(Fig.19). In addition, there was a significant difference among the split core samples where the PC06, PC07, PC08, PC11, and PC12 showed low average velocity and density in

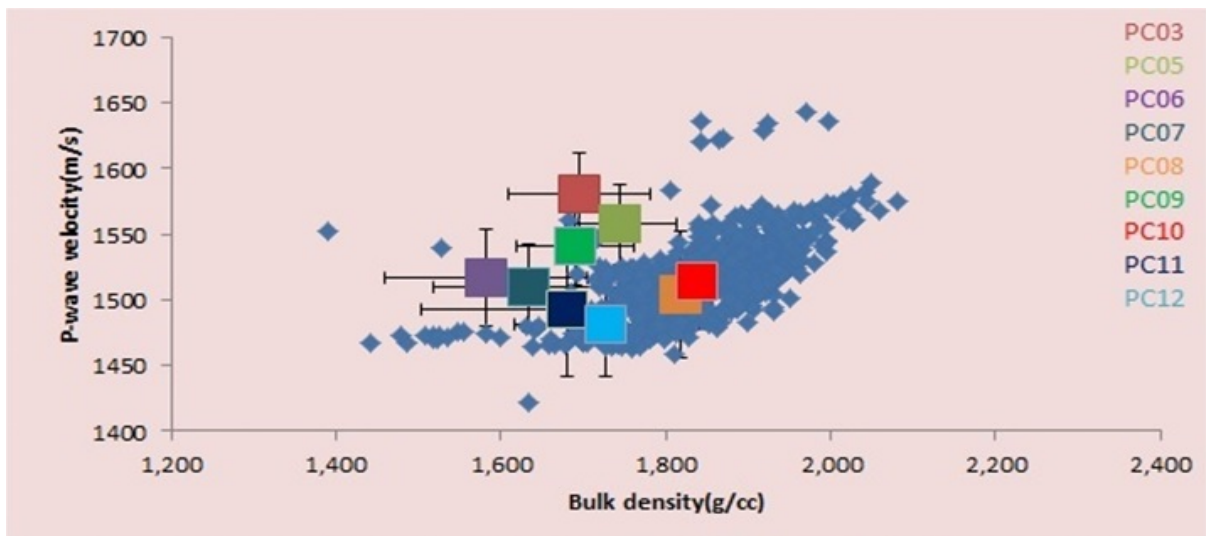


Fig.19. Average velocity, density data for split cores compared to spread of data from the whole core PC10. Black bars represent standard deviation. The processed velocity–density data of the PC10 are displayed in blue squares.

comparison with the reference core. All split core velocity and density variability is shown in figure 19. The general distribution indicates that PC03, PC05, and PC09 showed higher velocity but lower density values in comparison to PC10. This observation indicates that this deviation may be related to errors in the measured core thickness which should impact the calculated velocity and density in opposite ways. In contrast, PC06 and PC07 show lower velocity-density values than PC10 (Fig.19).

To test whether average offsets in the velocity and density are significant in comparison to PC10, variance and t-test were used. In these tests, the sample mean for each core was computed as

$$\mu = \sum x/n \quad (17)$$

where

x= the measured velocity or density

n= number of x.

The variance was calculated as

$$S^2 = \frac{\sum(\bar{X}-\mu)^2}{n-1} \quad (18)$$

where

\bar{X} =sample mean

μ =population mean (1515 m/s).

The standard deviation of the population was determined, taking the root square of the variance in equation (18)

$$S = \frac{\sqrt{(\bar{X} - \mu)^2}}{(n - 1)} \quad (19)$$

where

S=variance (m/s)

μ = the sample mean (m/s).

Confidence intervals of 95% were tested using a population mean of reference core for velocity and assuming the standard deviation is unknown .The results obtained from this test showed that the confidence intervals of the cores PC03, PC05, and PC09 lie away from PC10. In contrast, the confidence intervals of other cores are included within the range of PC10. In this test, the confidence intervals for a population mean were found as follows

$$\bar{X} - t_{\alpha/2} * S / \sqrt{n} \quad \text{to} \quad \bar{X} - t_{(\alpha/2)} * S / \sqrt{n} \quad (20)$$

where

α = significance level (0.05).

Further tests were performed to prove a hypothesis test for one population mean when the population standard deviation is unknown. This test was based on the assumption that the variable x (average velocity) is normally distributed with mean μ for the sample

of size n , and the studentized version of \bar{X} has the t-distribution with $n-1$ degrees of freedom

$$t = (\bar{X} - \mu)/(s/n) \quad (21)$$

To test the results, the null and alternate hypothesis was stated, where the null hypothesis is the claim that mean average velocity of each core is equal to the average velocity of PC10 (1515m/s). The alternative hypothesis is that the average velocity of the cores is different from PC10. This hypothesis test is two tailed. The t-value having area α under the t-curve on both sides is $t_{\alpha/2}$ with degree of freedom (DF) = $n-1$, that is $8-1=7$, thus $t_{\alpha/2}=t_{0.05/2}=0.025$. Since the hypothesis test is two tailed this means that values which are higher than 2.365 or lower than -2.365 lie in the rejection area. In response to the confidence interval test, the three cores indicated that the range of the P-wave velocity obtained from the logged core is greater than that of PC10 (Table5).

Core	\overline{VP} (m/s)	$\bar{X}-\mu$	$(\bar{X}-\mu)^2$	Variance (S ²)	STD (S)	MIN	MAX	T- statistic	T-value
PC03	1580	65.87	4339	1228	5	1576	1585	4.65	2.365
PC05	1558	43.52	1894			1558	1562	3.07	-2,365
PC06	1517	2.51	6			1517	1521	0.18	
PC07	1509	-5.09	26			1509	1514	-0.36	
PC08	1504	-10.23	105			1504	1508	-0.72	
PC09	1541	26.08	680			1541	1545	1.84	
PC11	1493	-21.02	442			1493	1498	-1.48	
PC12	1481	-33.19	1102			1481	1485	-2.34	
PC10	1515					1510	1519		
		sum	8593						

Table 5. The confidence intervals and t-test values for average P-wave velocity, \overline{VP} is the average velocity for split and whole cores, $\bar{X}-\mu$ column is the differences between the average velocity of the whole and average velocity for each split core, Min and Max column represent the confidence interval of split cores, T-statistic value represents the calculated t-value from equation (21), and t-value is the value obtained from a standard t-table for normal distribution value with unknown standard deviation.

4.3.1 Interpretation of results

A correct decision occurs either if the means and standard deviations of the split cores are significantly different from those of PC10 or if they are not significantly different. At

the 5% significance level, the data provide sufficient evidence to conclude that the means and standard deviations of compressional velocity were not significantly different with all cores except PC03 and PC05. At the same significance levels, the data provide sufficient evidence to conclude that the means and standard deviations were significantly different at PC03 and PC05 cores so we reject the null hypothesis.

The same tests were performed using the average bulk density of PC10 as 1.84 g/cc. Following the same procedures used with the average velocity, the confidence intervals and t-values were calculated for bulk density (Table .6).

Core	$\overline{\rho B}$ (g/cc)	$\overline{X}-\mu$	$(\overline{X}-\mu)^2$	Variance (S ²)	STD (S)	MIN	MAX	T- statistic	T-value
PC03	1.70	-0.14	0.02	0.02	0.02	1.68	1.72	-2.10	2.365
PC05	1.75	-0.09	0.00			1.73	1.76	-1.37	-2.365
PC06	1.58	-0.25	0.06			1.56	1.60	-3.79	
PC07	1.63	-0.20	0.04			1.61	1.65	-3.03	
PC08	1.82	-0.02	0.0004			1.80	1.84	-0.30	
PC09	1.69	-0.14	0.02			1.67	1.71	-2.20	
PC11	1.68	-0.15	0.02			1.66	1.70	-2.33	
PC12	1.73	-0.11	0.01			1.71	1.75	-1.63	
PC10	1.84					1.82	1.86	0	

Table 6. The confidence intervals and t-statistic values of density for the split and whole core samples. The symbols represent the same variables as in table 5 but in this case for the t bulk density values.

The results showed that the means and standard deviations were significantly different with all cores except PC06 and PC07. At the same confidence level, data provide good evidence to conclude that the means and standard deviations of PC06 and PC07 cores are significantly different from that of PC10, and thus the null hypothesis was rejected (Fig.20).

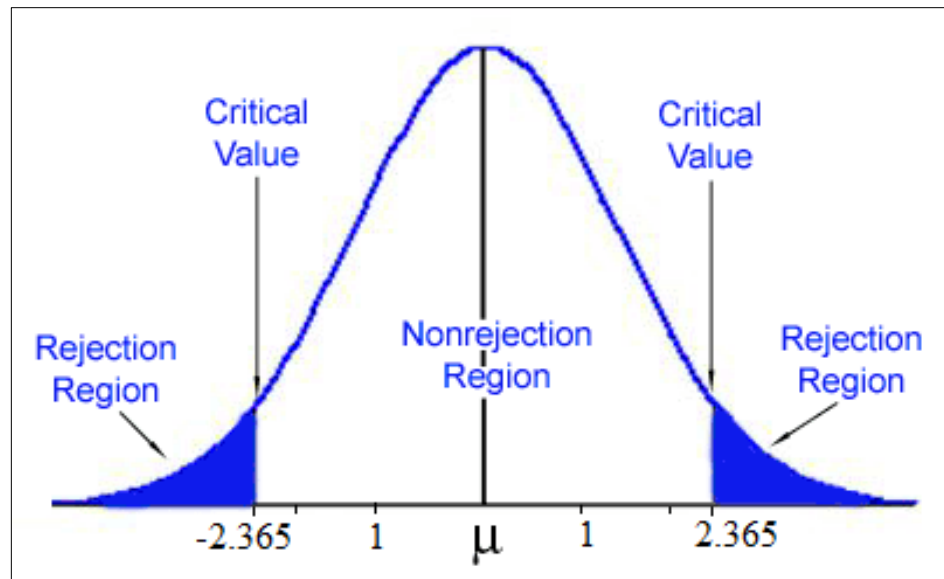


Fig.20: Graphical display for rejection regions for two-tailed test.

To evaluate the sensitivity of changes in velocity and density to a change in core thickness, average changes in velocity (34 m/s) and density (0.05 g/cc) (Figs. 21 and 22) that arise from a 1 mm error in the thickness measurement, were divided by the range of velocity and density from the corrected cores (Figs. A2- 1, 2, and 6). The results showed that the velocity is more sensitive to errors in core thickness than bulk density, with a 1 mm thickness error resulting in a ~27-30% error in the velocity, compared to ~17% in bulk density (Table.7).

Core	ΔV_p (m/s)	Range (m/s)	ΔV_p %	ΔP_B (g/cc)	Range (g/cc)	$\Delta \rho_B$ %
PC03	34	1510-1635	27.2	0.05	1.50-1.80	16.6
PC05	34	1475-1600	27.2	0.05	1.60-1.90	16.6
PC09	34	1460-1570	30.9	0.05	1.50-1.80	16.6

Table7. Calculated error introduced by 1 mm core thickness error expressed as a function of the measured data range for velocity and density of cores PC03, PC05 and PC09.

4.4 Correcting for errors in core thickness

To evaluate if the core errors caused the offsets in the mean velocity and density of some split cores, the thickness deviation that would account for offsets in calculated density and velocity values was calculated. First, the average velocity and density for each split core was subtracted from the average velocity (\overline{Pv}) and density (\overline{PB}) of PC10 (Table 8). Second, the differences in the average velocity ($\Delta \overline{Pv}$) and density ($\Delta \overline{PB}$) between PC10 and split cores were determined (Table 8). The average errors in the velocity (\overline{Pv} errors)

and density (\overline{PB} errors) for each core were calculated by dividing the average differences in these values by the average differences in the velocity (~ 34 m/s) and density (~ 0.05 g/cc) respectively, for a change of 1 mm in core thickness (Figs. 21 and 22). Taking the differences in the average velocity-density errors for each core, the average core thickness errors (\overline{CT} error) were determined (Table 8).

Core	\overline{CT}	Ln (cps)	\overline{Pv} (m/s)	\overline{PB} (g/cc)	ΔVp (m/s)	ΔPB (g/cc)	\overline{Pv} error (mm)	\overline{PB} error (mm)	\overline{CT} error
PC03	4.03	9.01	1580	1.70	-65	0.14	-1.94	3.07	2.51
PC05	3.97	9.00	1558	1.75	-43	0.09	-1.28	2.01	1.64
PC06	4.08	9.03	1517	1.58	-2	0.25	-0.08	5.93	3.00
PC07	4.18	9.01	1509	1.63	5	0.20	0.15	5.37	2.76
PC08	4.09	8.97	1504	1.82	10	0.02	0.31	0.43	0.37
PC09	4.16	9.01	1541	1.69	-26	0.15	-0.77	2.85	1.81
PC11	3.78	9.00	1493	1.68	21	0.16	0.64	3.83	2.23
PC12	3.89	9.03	1481	1.73	33	0.11	1.01	2.19	1.60
PC10	7.88	9.62	1515	1.84	0	0.00	0.00	0.00	0.00

Table 8. The calculated differences, errors, and the corrections of the measured P-wave velocity, bulk density, and core thickness. The red values represent PC03, PC05, and PC09 that deviate from PC10.

Average densities for all cores were lower than those for PC10 (Table 8). While the average velocity for PC03, PC05, and PC09 are higher than PC10. This finding suggests that an overestimation of core thickness may have caused the decrease in bulk density and increase in the average velocity for these cores. While the underestimated core thickness will increase bulk density and decrease velocity.

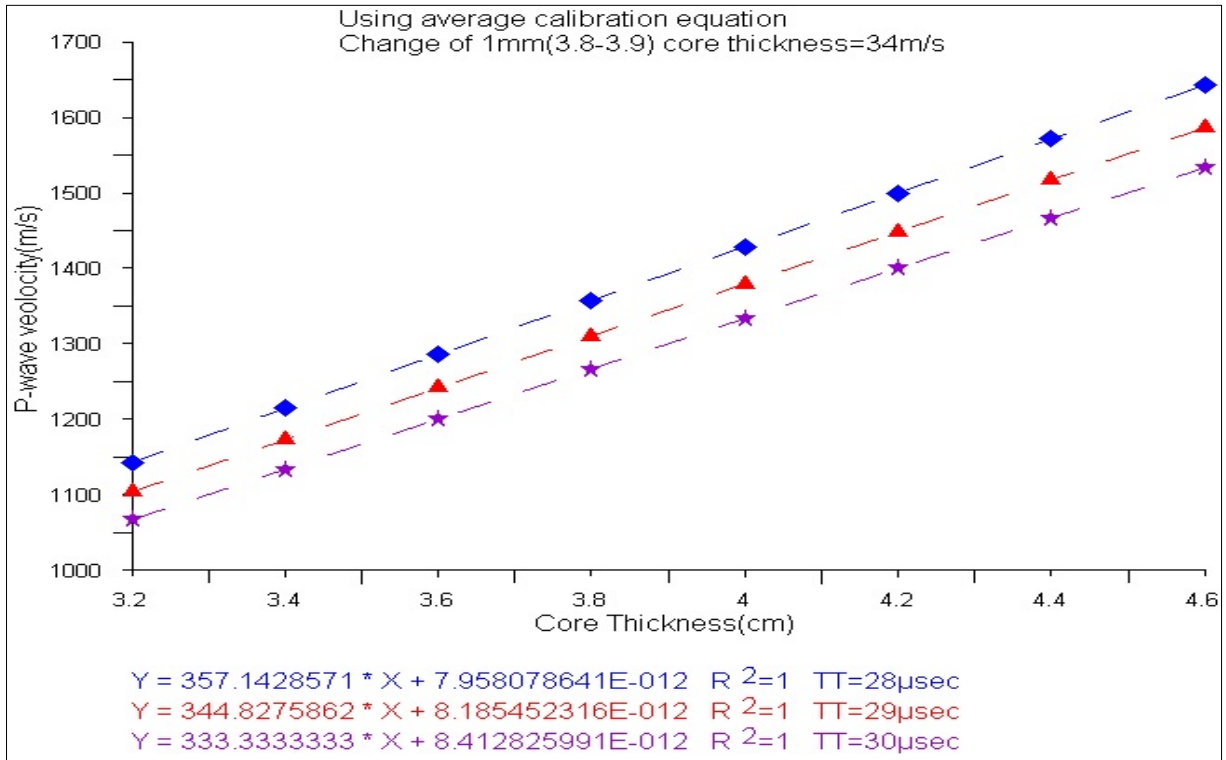


Fig.21. An example of P-wave velocity and core thickness relationship.

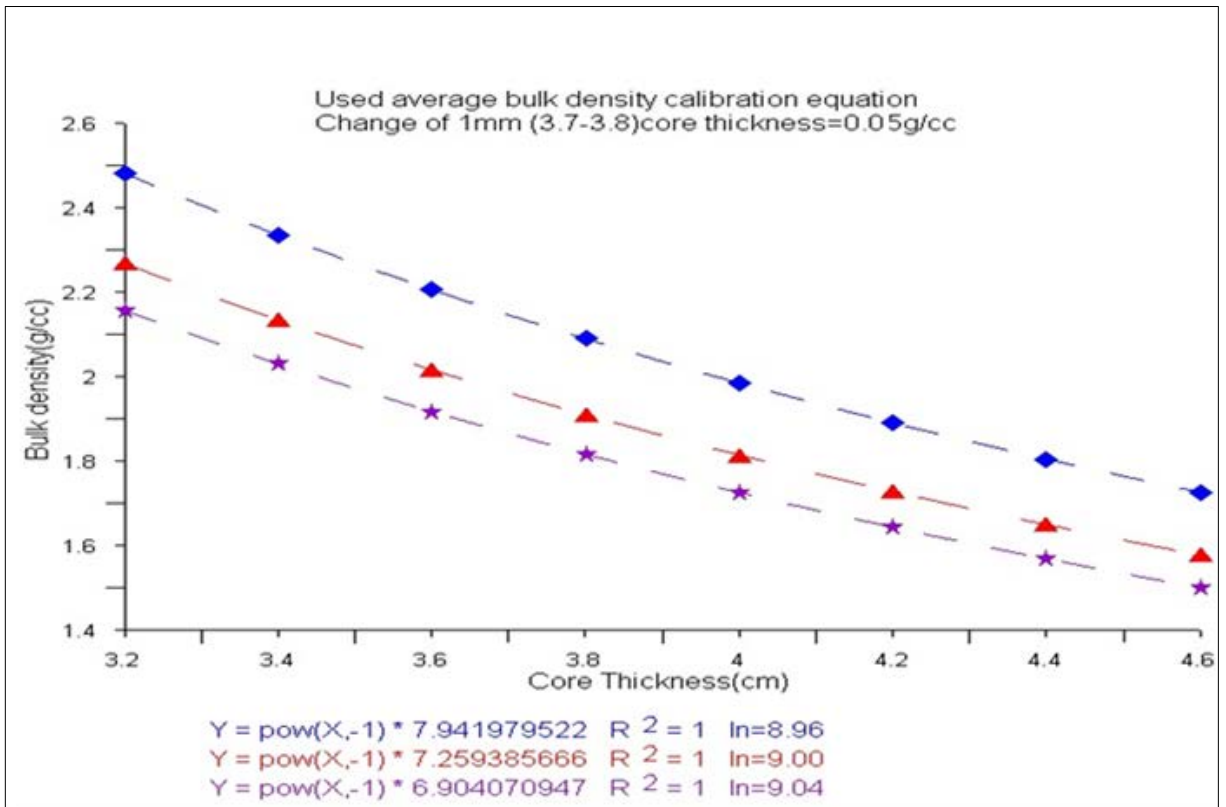


Fig.22. An example bulk density and core thickness relationship.

In order to estimate the best indicator for the resulted errors in the measured physical properties, a comparison between the corrected velocity, density, and the average thickness errors was performed. The calculated errors (Table 8) were used to correct velocity and density for PC03, PC05, and PC09. This correction is based on the fact that increases density and decreases velocity will result in a good fit between the average velocity-density of the corrected values with PC10. Error bars represent one standard deviation for the corrected velocity and density values for the PC03, PC05, and PC09 (Fig.23).

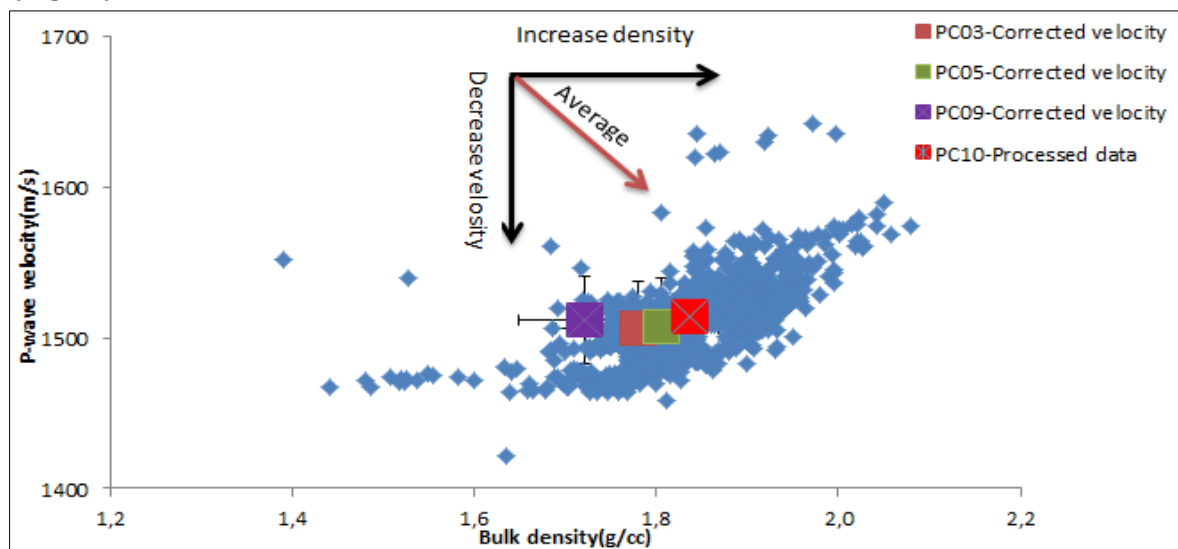


Fig.23. Velocity-density relationships of corrected PC03, PC05, and PC09 velocity correlated with PC10 core using the correction based on increasing density and decreasing velocity values. Black bars represent the standard deviations.

From the data in figure 23, it is apparent that the distribution of the corrected data is close to the processed data points of PC10. The uncorrected split cores showed generally low average velocity and density in comparison with the reference core (Fig.24). No correction was made on these cores.

The results obtained from the correction of the calculated errors showed that the velocity error is the best indicator that can be used to predict the core thickness deviations in the PC03, PC05, and PC09 (Figs.25 and 26). The distribution of the corrected velocity and density using velocity errors show very close normal distribution to that of the PC10 data. On the other hand, the normal distribution of the corrected data from the average density and core thickness errors lie away from the mean velocity and density of PC10. The results obtained from average thickness errors, however were shown to be not of use in correcting the thickness errors. The corrected velocity and

density using density errors showed very low decrease in velocity for the PC09 core with less increase in velocity for both PC03 and PC05. The average density was very high in the PC09 and rather high for PC03 and PC05.

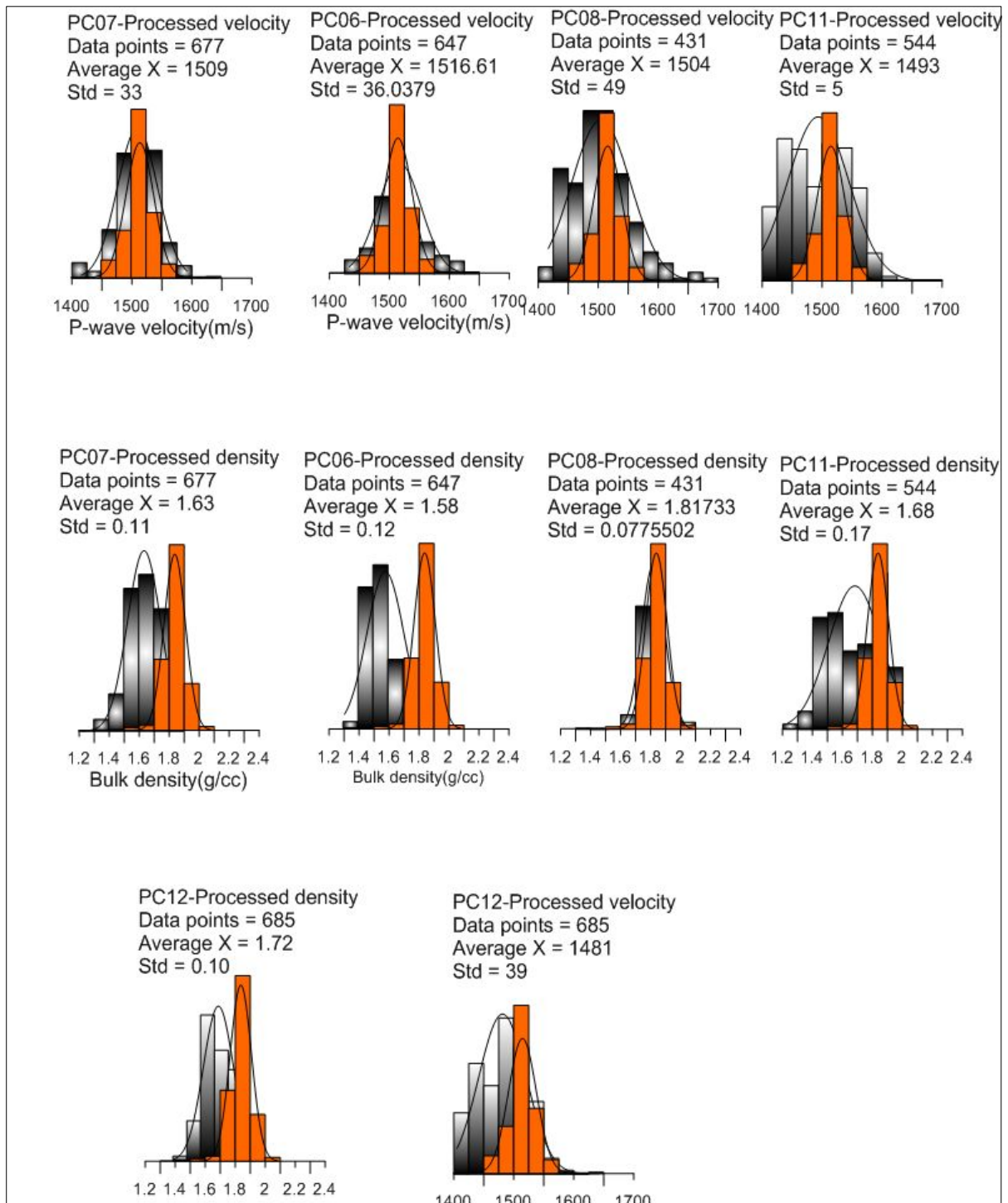


Fig.24: Bar diagrams illustrate the corrected and processed velocity-density relationships (gray bars) of PC06, PC07, PC08, PC11, and PC12 correlated with the processed data of PC10 (orange bars). The distribution curves (black) represent the Gaussian distribution of the data.

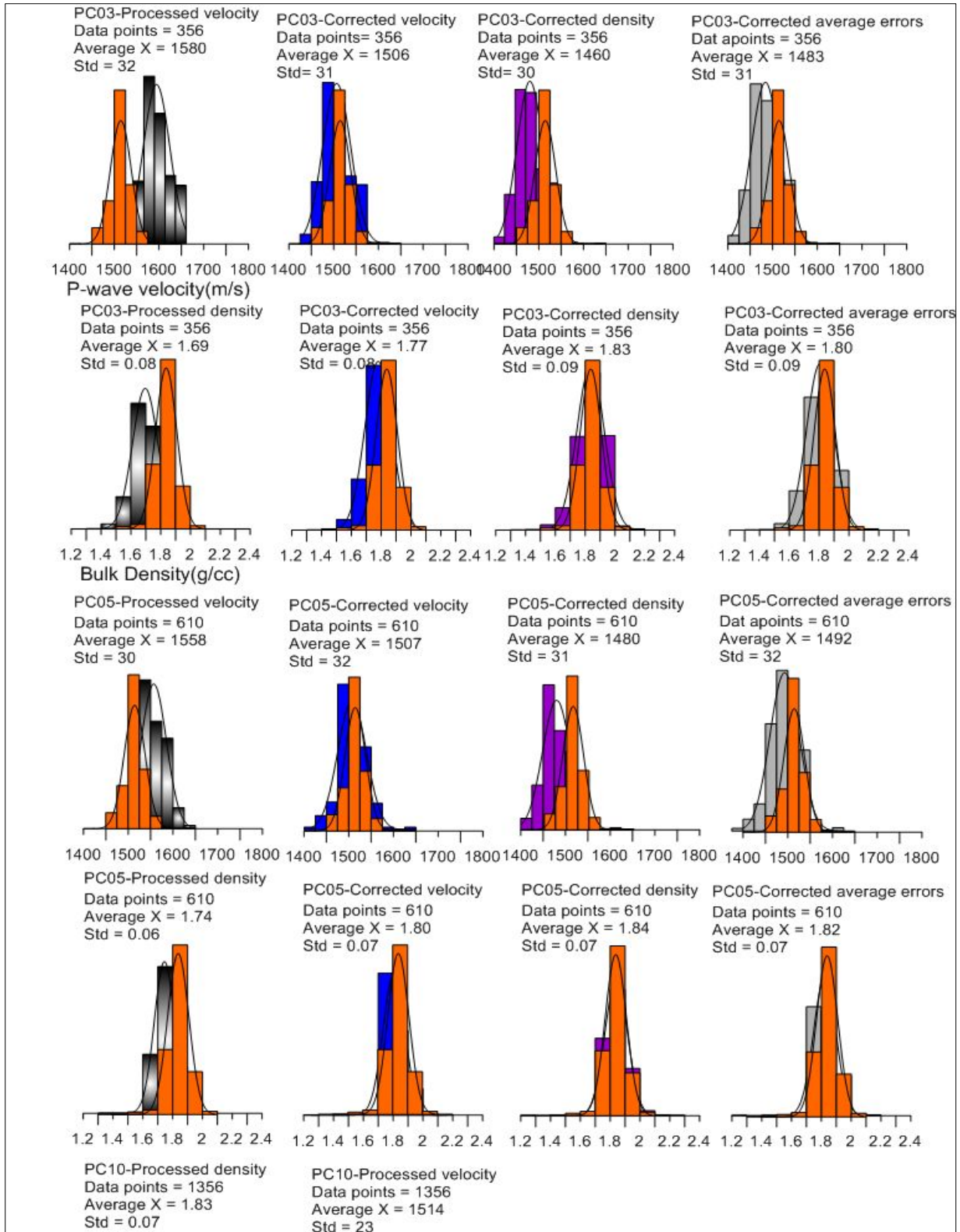


Fig.25. Bar diagrams illustrate the corrected and processed velocity-density relationships of PC03 and PC05 compared with the PC10 data. The corrected velocity and density used velocity, density, and core thickness errors are represented in the blue, purple, and gray colors respectively. The corrected physical properties were compared with the processed velocity and density of PC10 (orange). The distribution curves (black) represent the Gaussian distribution of the data.

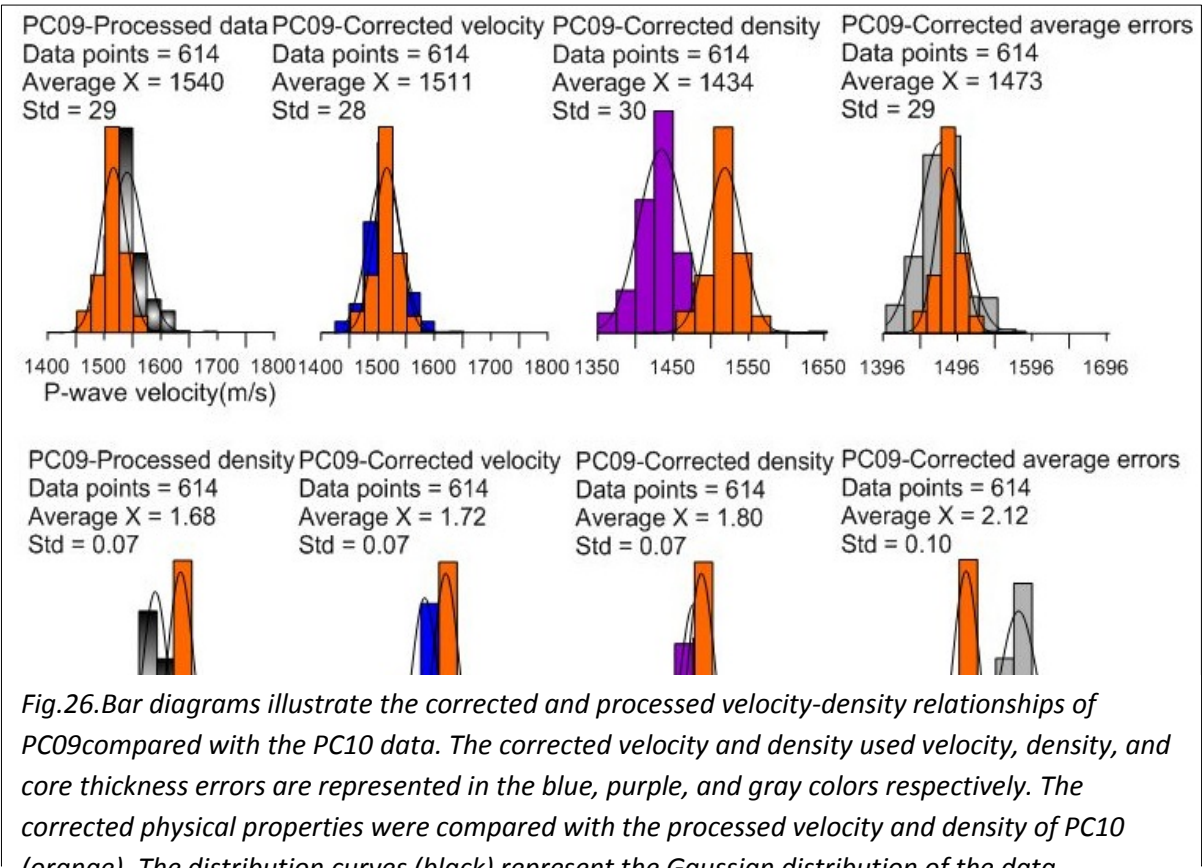


Fig.26. Bar diagrams illustrate the corrected and processed velocity-density relationships of PC09 compared with the PC10 data. The corrected velocity and density used velocity, density, and core thickness errors are represented in the blue, purple, and gray colors respectively. The corrected physical properties were compared with the processed velocity and density of PC10 (orange). The distribution curves (black) represent the Gaussian distribution of the data.

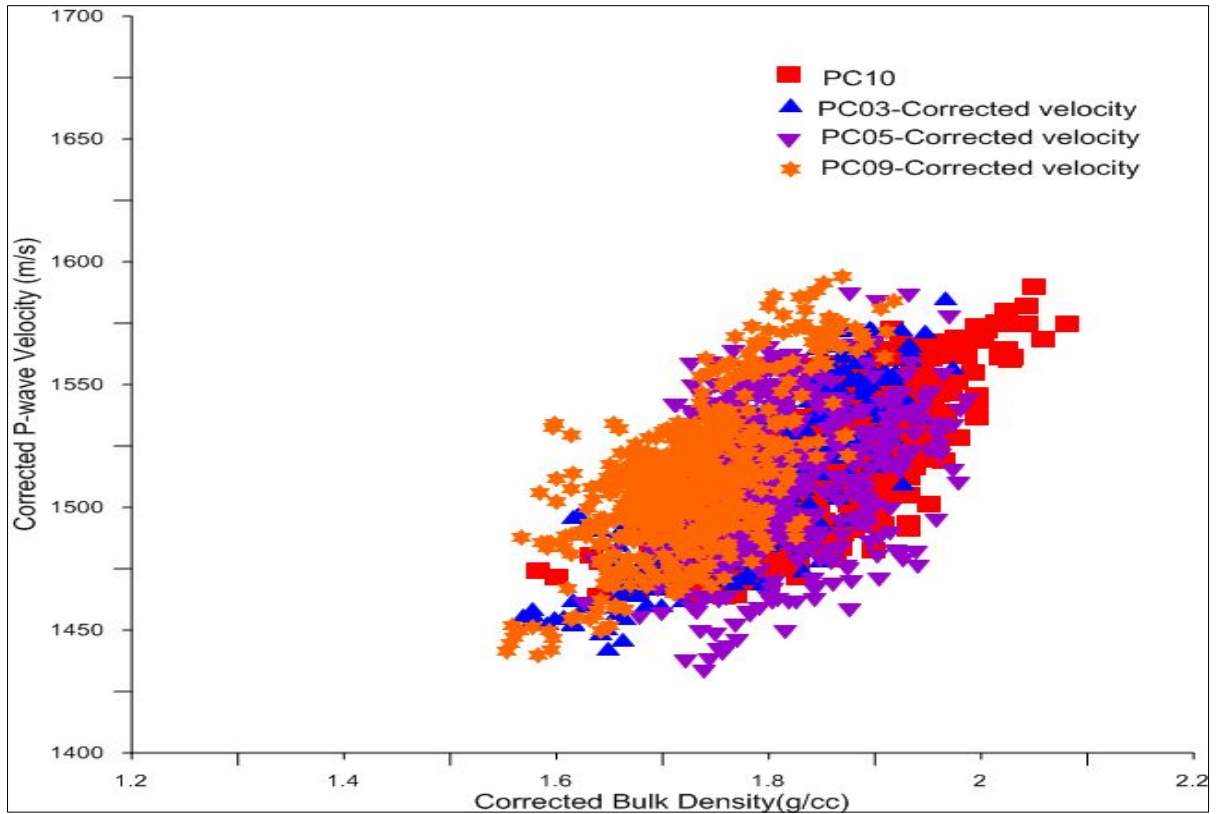


Fig.27 Cross-plot of corrected velocity-density relationships obtained by using the corrected velocity of PC03, PC05, and PC09 cores correlated with PC10 data.

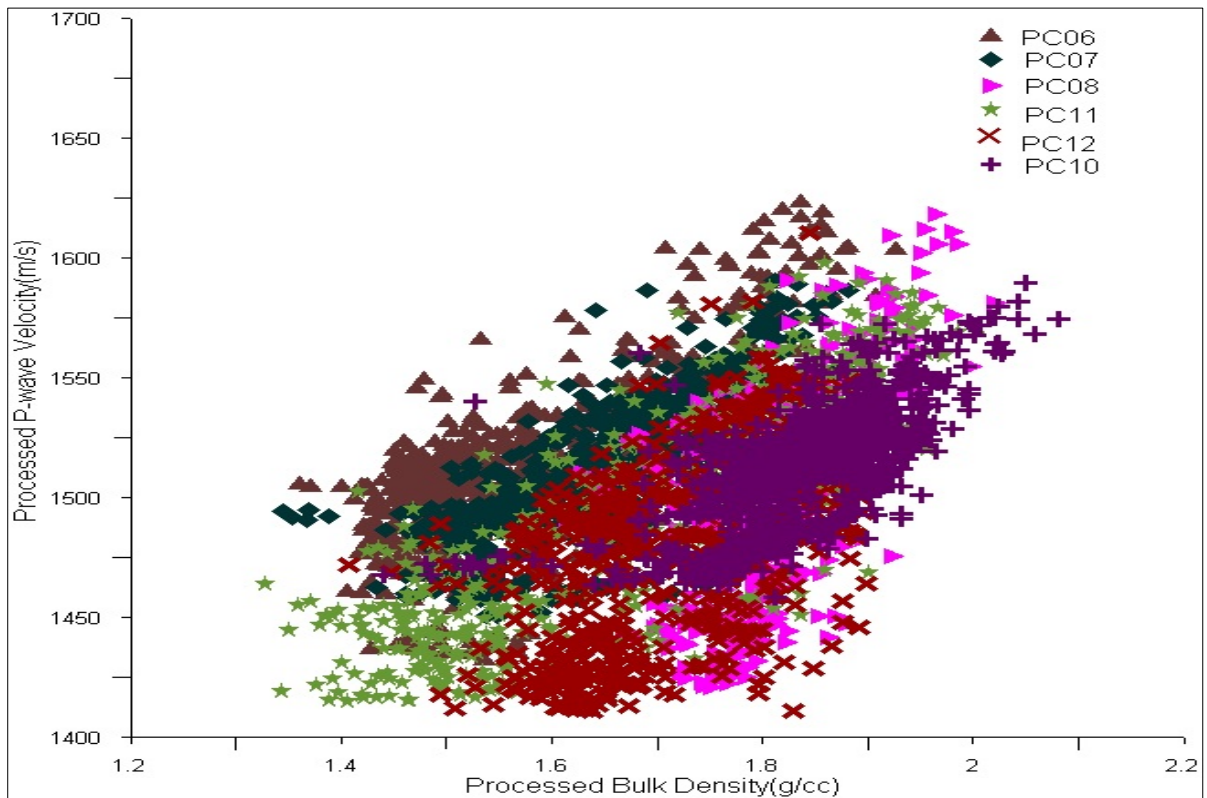


Fig.28. Cross-plot of velocity-density relationships of PC06, PC07, PC08, PC11, and PC12 cores correlated with the PC10 core.

5. Discussion

Cross-plots between the corrected P-wave velocity and bulk density for PC03, PC05, and PC09 show an improved correlation to measurements from the whole core PC10 (Fig. 27). Data from corrected split cores, uncorrected split cores, and the whole core (PC10) show a clear trend towards increasing compressional wave velocity with increasing bulk density (Figs. 27 and 28). These results corroborate the findings of a great deal of previous work in this field (Hamilton, 1970; Hamilton and Bachman, 1982; Bachman, 1985, 1989; Richardson and Briggs, 1993; Richardson et al. 1997; Schnack-Friedrichsen et al. 2010). These researchers found that an increase in the compressional velocity is associated with increasing the bulk density with the depth. However, substantial scatter exists around this trend in the current study (Figs. 27 and 28), with some split cores such as PC06, PC07, PC08, PC11, and PC12 exhibiting lower P-wave velocity and bulk density in comparison to the reference core. Variability in the velocity-density trend can be explained by many factors which include porosity, grain size, sediments composition, and the associated influence on the elastic moduli (rigidity and compressibility) of the sediments.

5.1. Velocity-density and porosity relationships:

Overburden pressure increases during burial. As a result, sediments compact and their porosity decreases. This increases the rigidity of the sediments (Erickson and Jarrad, 1998). Porosity is expressed as the ratio of the volume of all pore space with respect to the entire volume (Hamilton, 1970). It is considered a sensitive indicator of the behavior of the compressional velocity in marine sediments because compressional velocity is largely dependent on the compressibility of pore water rather than on the compressibility of the solid fraction. The compressibility of water is relatively larger than that of mineral grains (Hamilton and Bachman, 1982). As effective pressure increases, water in pore spaces is expelled towards the seafloor, porosity is reduced and sediments become denser. At shallow depths, porosity is high where sediments are unconsolidated. From 0 to 2.5-3 km, a negative exponential relationship between depth and porosity is presumed (Wood, 1989). Mechanical compaction is considered to be the dominant factor that controls the reduction of porosity at these depths with less significant effects of time and temperature (Ramm, 1992).

As porosity is decreased, the bulk and shear moduli ($K+4/3\mu$) in equation (3) increase, resulting in an increase in the rigidity of the grain frame. This increase in turn results in a more rapid transmission of sound waves through the sediments. Because the compressional velocity increases with the increase in the rigidity (compressibility) of sediments, an increase in the compressional velocity requires that the relative increase

in the elastic moduli should be greater than that of bulk density. Hamilton (1970) argued that the rigidity is controlled by many factors such as the relationships between van der Waal and Coulombic forces, geochemical alterations, mineralogy, and chemistry of interstitial water.

In summary, as effective pressure increases during burial, porosity decreases because pore water is expelled towards the seafloor, and rigidity increases because of increased grain-to-grain contact resulting in an increase in velocity and density.

Although downcore reductions in porosity will generate higher velocity and density of the sediments, there is substantial scatter in the logged data, with intervals of increased velocity and density followed by intervals of decreased velocity and density (Figs.A2-1-9). This discrepancy is explained by the fact that the sediments used in this study are composed of grains of different sizes (Fig.29). Hamilton (1971) has shown that

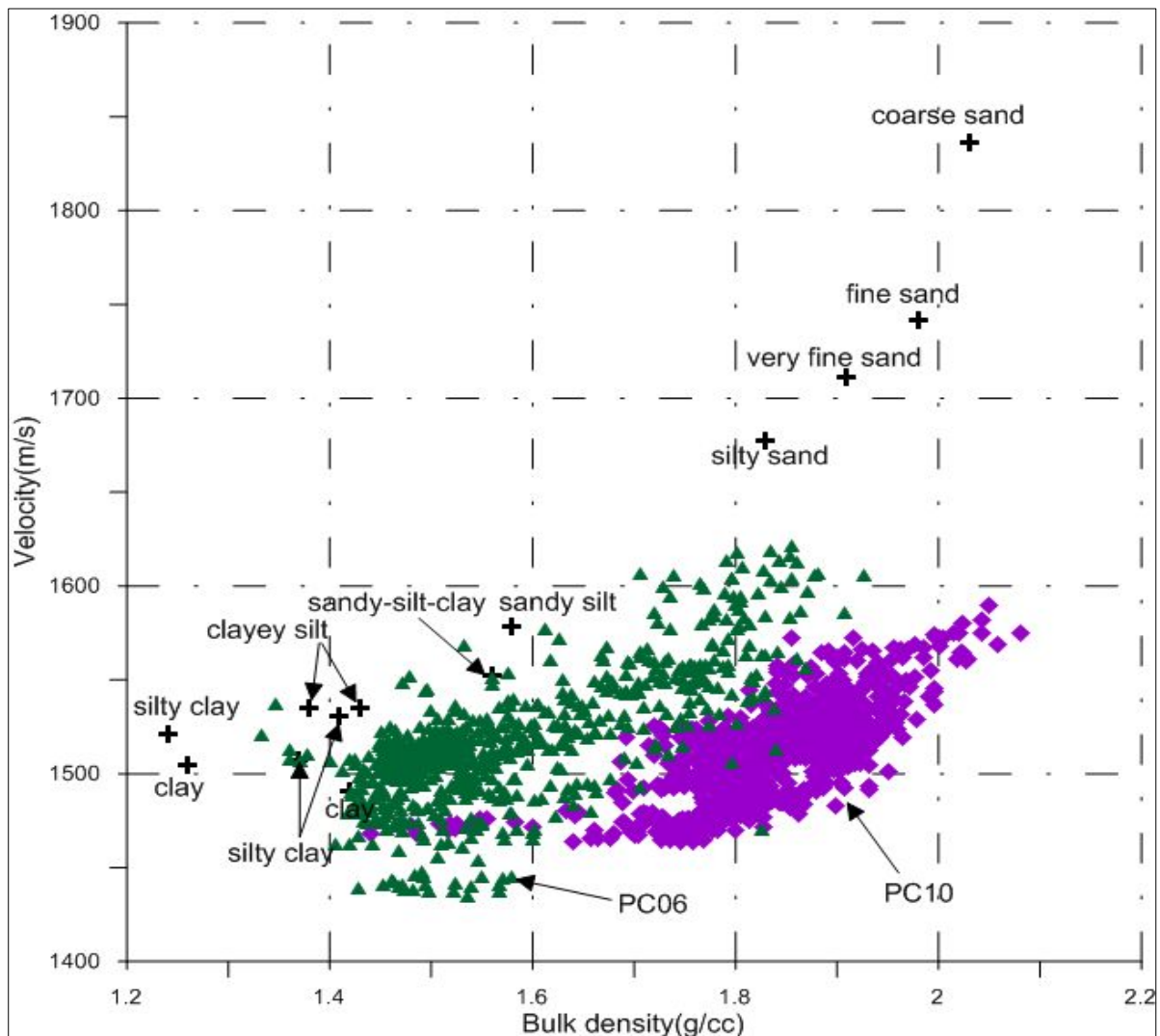


Fig.29. Comparison of data from marine box cores (Hamilton, 1971) (black crosses) and LOMROGIII data of whole core PC10 (purple squares) and split core PC06 (forest blue triangles).

increasing the bulk grain size of siliciclastic sediments results in increased compressional wave velocity and bulk density. For instance, clay has a velocity of 1505 m/s, silty clay 1521 m/s, and coarse sand 1836m/s (Hamilton, 1971) (Fig.29). Thus the differences in the velocity-density trend could be explained by intervals of coarser sediments.

In general, the results obtained from this study show that the average compressional velocity and bulk density lies within the range of clay to fine sand sediments with some expectations above this range (Fig.30). The overall trends toward higher velocity and density in the measured cores mirror increases expected as the average grain size increases (Figs. A2-1-9).

5.3 Comparison between Lomonosov Ridge sediments and Porosity-Velocity models

The corrected velocity and density data from the LOMROGIII cores indicate a similar, albeit scattered, relationship between P-wave velocity and bulk density. Because porosity decreases with increase in bulk density and grain size of sediments, this result supports the idea that for most of the sediments the variance in porosity is inversely related to the compressional velocity and bulk density. These results are consistent with those of Hamilton (1970, 1971), Hamilton and Bachman (1982), and Schnack-Friedrichsen et al. (2010), who suggested that an increase in porosity of marine sediments is often associated with a decrease in the compressional velocity and bulk density.

The relationship between porosity and compressional wave velocity from the LOMROGIII cores was compared to global empirical models for siliciclastic marine sediments, including Wyllie et al. (1956), Raymer et al. (1980), and Jarrad and Erickson, (1998). The first step in this comparison was to convert the LOMROGGIII bulk density measurements to porosity. Equation (2) was used for this, and grain densities of quartz (2.65 g/cc), silt (2.72 g/cc), and clay (2.75 g/cc) were assumed (Geotek, 2000) because the LOMROGIII sediments are mostly composed of clay and silty clay with some sandier intervals. The effect that grain density has on the measured velocity-porosity values is somewhat small. Using different grain densities in the porosity calculation shows slight increase in porosity. For example for a bulk density of 1.7 g/cc, calculated porosities for a given grain density (2.65,2.72, and 2,75 g/cc) and a water density of 1.024 g/cc result in porosities of 0.58,0.60, and 0.61g/cc respectively. However, this increase does not affect the trend of velocity-porosity on the predicted velocity curve (Fig.30).

The Wyllie et al. (1956) time averaged equation expresses the relationship between the compressional velocity and porosity by

$$\Delta t = \phi \Delta t_f + (1 - \phi) \Delta t_{ma} \quad (22)$$

where

Δt =the travel time of sonic velocity ($\mu\text{sec}/\text{ft}$)

Δt_f =the travel time of pore fluid ($\mu\text{sec}/\text{ft}$)

Δt_{ma} = the travel time of the solid material ($\mu\text{sec}/\text{ft}$)

ϕ =porosity

or in terms of sound velocity equation

$$\frac{1}{V} = \frac{\phi}{V_f} + \frac{(1 - \phi)}{V_{ma}} \quad (23)$$

where

V = sonic velocity (ft/sec)

V_f =the P-wave velocity of the pore fluid (ft/sec)

V_{ma} =the P-wave velocity of the solid material (ft/sec)

ϕ =porosity.

The selection of suitable matrix velocity to transform the acoustic velocity to porosity is rather tricky due to the large range in published values. For instance, limestone matrix velocity may range from 6400m/s to 7010 m/s, and sandstone from about 4586m/s to more than 5943 m/s (Raymer et al., 1980). To apply the Wyllie time-average equation to the LOMROGIII data, matrix velocities were calculated using various grain density values (2.65, 2.72, and 2.75 g/cm³), the maximum and minimum matrix velocity of shale (2013, 5180; Rider and Kennedy, 2011), sound velocity of water of 1480 m/s, and water density (distilled water) of 1 g/cc. The matrix velocities of the LOMROGIII sediments were calculated by rearranging the time-average equation and solving it for matrix velocity

$$V_{ma} = (1 - \phi) / ((1/V_{measured} - (\phi/V_f))) \quad (24)$$

where

V_{ma} = matrix velocity (m/s)

$V_{measured}$ =measured velocity from the LOMROGIII cores (m/s)

V_f = water velocity (m/s)

ϕ = calculated porosity.

The maximum and minimum matrix velocities of shale were used to predict the velocity in the Wyllie equation. These were compared to the calculated matrix velocities from the Wyllie equation (1568m/s, 1576m/s, and 1581m/s). The resulted velocities were plotted over a range of porosity between 0.2 to 0.8 (Fig.30-A). In addition, the measured compressional velocity from MSCL was plotted against the calculated porosity using a grain density of 2.72 g/cc. The highest value of the calculated P-wave velocity using a high grain density (2.75) g/cc was obtained at the low porosity value of 0.2. Using shale matrix velocities in predicting the velocity shows large scatter from the measured velocity of the LOMROGIII sediments.

The measured velocities from this study do not follow the velocities predicted by the Wyllie equation. The results of this study suggest that the Lomonosov Ridge sediments do not adhere to the Wyllie equation. This finding may be explained by the fact that the composition of sediments used in the time average equation is different from that involved in the core retrieved from Lomonosov Ridge. The Wyllie equation is only valid for homogenous, non-clayey and normally consolidated sediments with low porosities less than 0.25. Above this range, the error in predicting velocity from porosity increases. These characteristics are very different from those of the high porosity, clayey sediments from the Lomonosov Ridge.

In order to increase the reliability of the porosity-to-velocity transformation in higher porosity siliciclastic sediments, Raymer et al. (1980) suggested an improvement to Wyllie's time averaged equation. This new model was based on extensive comparisons between the travel time of sonic waves over different sediment porosities. The values of matrix velocities were considered to be consistent over the total porosity range for a given rock such as a value of 5440 m/s for pure quartz sandstones, 6248 m/s for limestone, and 6934 m/s for dolomite. The Raymer et al. model is intended to provide an accurate prediction of sonic velocity in siliciclastic rocks and be diversely used for different range of porosities (Dvorkin, 2001). The Raymer et al. non-linear equation is expressed as

$$V_p = (1 - \Phi)^2 V_{PS} + \Phi V_{PF}, \Phi < 0.37 \quad (25)$$

where

Φ = porosity

V_p = the measured P-wave velocity (m/s)

V_p and V_s = the P-wave velocity in (m/s) for solid and pore fluid respectively.

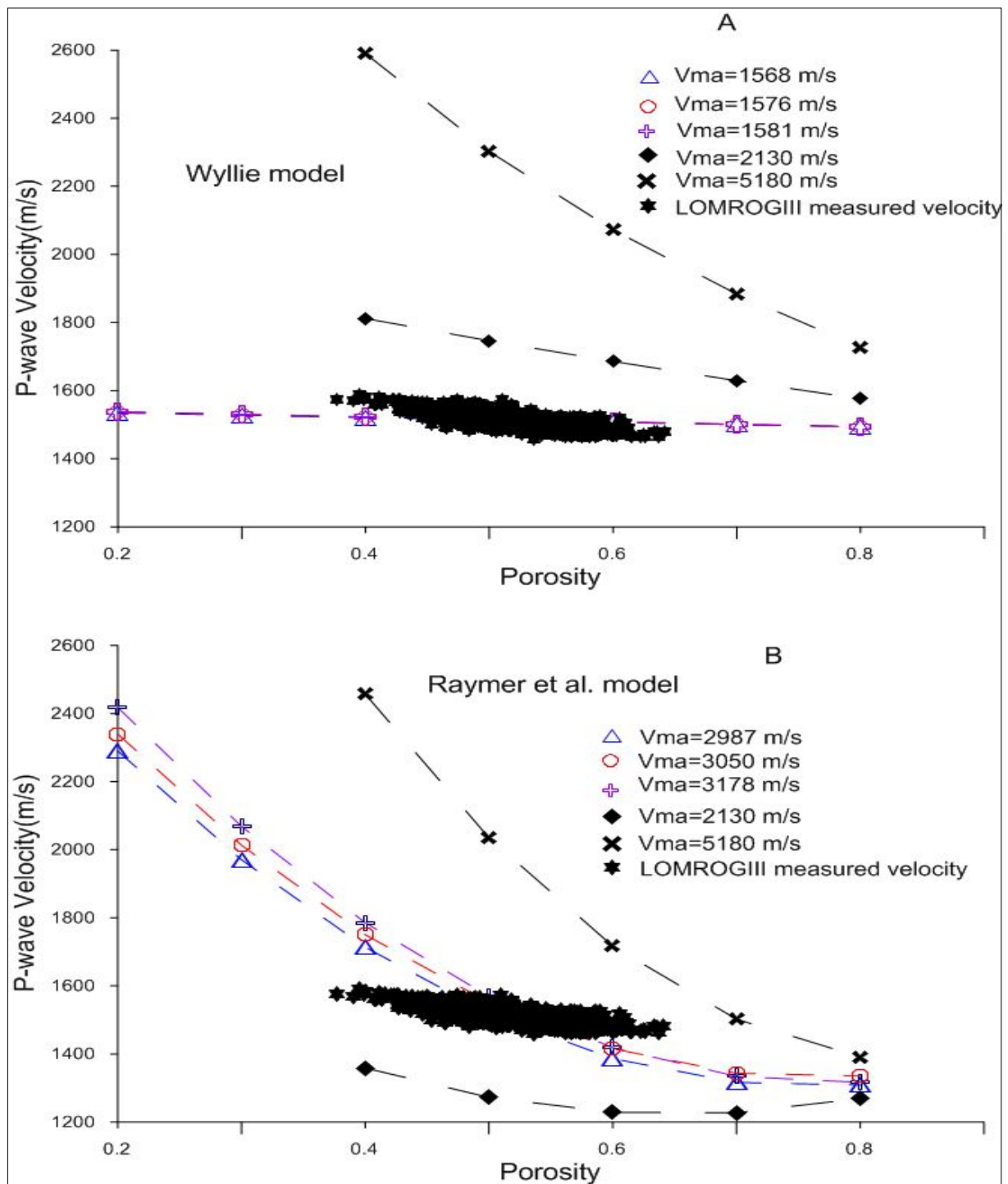


Fig.30. The P-wave velocity-porosity relationships calculated by Wyllie et al.(1956) and Raymer et al.(1980) equations using the minimum and maximum of shale matrix velocities (2130 m/s (black square) and 5180 m/s (black cross) respectively, and various matrix velocities calculated from the Wyllie and Raymer equation. The calculated velocity was plotted versus range of porosities (black star).

The same maximum and minimum shale matrix velocities as were used in the Wyllie analysis were used to predict the velocity in the Raymer equation. These were compared

to the calculated matrix velocities (2987, 3050, and 3178 m/s) derived by inverting the Raymer equation and solving it for matrix velocities for the LOMROGIII cores.

$$V_{ma} = (V_{measured} - \phi * V_f) / (1 - \phi)^2 \quad (26)$$

The results were plotted against a range of porosities from 0.2 to 0.8, and the measured velocities from the LOMROGIII were plotted against the same range of porosities (Fig.30.B).

The results illustrate that the calculated velocities using the limits of shale matrix velocities (2030m/s and 5180 m/s) show large scatter above and below the measured velocities from the LOMROGIII sediments. In addition, the calculated matrix velocities from the Raymer equation using the measured velocities from this study show a poor fit between the two datasets. Porosity trend is not captured because the Raymer model increases more quickly than the measured data or vice versa. This finding could be explained by the fact that the porosity used in the Raymer equation does not work with sediments with porosities above 0.37 which includes all the sediments in this study. The findings using the Raymer and Wyllie studies suggest that the Lomonosov Ridge sediments do not adhere to these models.

The final velocity-porosity model that was compared was the global empirical relationship proposed by Erickson and Jarrad (1998). The principle of this approach is based on using different empirical relationships to predict the compressional velocity in siliciclastic sediments saturated with water over a wide range of porosities. The compressional velocity was tested in both unconsolidated and in highly consolidated sediments. In this model, there is no matrix velocity variable. Instead, Erickson and Jarrad (1998) identify three variables as the dominant parameters that control the compressional velocity. These include porosity, shale fraction, and consolidation history. Depending on the degree of consolidation, two equations were proposed: one for normally consolidated and the other for highly consolidated sediments (Erickson and Jarrad, 1998).

Moran et al. (2006) concluded that Lomonosov Ridge sediments should be classified as hemiplegic sediments dominated by high amounts of fine- grained sediments such as clay and silty- clay at depths lower than 163 m below the seafloor. As depth increases, these sediments include small amounts of ice-rafted remains which are indicators of coarse sediment such as sand. Therefore, the normal consolidation relationship

proposed by Erikson and Jarrad (1998) is appropriate to be used with Lomonosov Ridge sediments. Because these sediments are largely fine grained, a shale fraction of 1 can be assumed.

The equation of Erikson and Jarrad for normally consolidated sediments is

$$V_p = 0.739 + 0.552\phi + \frac{0.305}{[(\phi + 0.13)^2 + 0.0725]} + 0.61(V_{sh} - 1.123) * [X_1 - abs(X_1)] \quad (27)$$

where

$$X_1 = \tan [40(\phi - 0.31)]$$

abs = absolute values of X_1 .

Using the normal consolidation equation to predict the compressional velocity shows that for sediments with a fractional porosity higher than 0.40, a change of 0.1(0.4-0.5; fig.31) fractional porosity causes a decrease of ~36m/s in the compressional velocity. This finding correlates inversely with that from figure 21 which showed that a change of 1 mm core thickness results in an increase of ~34 m/s. At porosities greater than 0.40, a decline from a high consolidated relationship at low porosities to the normal consolidated relationship at high porosities is observed.

Porosity-Velocity relationships from the LOMROGIII cores follow the velocities predicted by the Erickson and Jarrad equation at porosities between ~0.50 and 0.60 (Fig. 31). The measured velocities of the whole and the corrected split cores are lower than those predicted at porosities lower than 0.50 (Fig.31). The correction of the errors in the split cores was tested using the whole core as a reference core thickness; thus the velocity-porosity trend of these cores is similar.

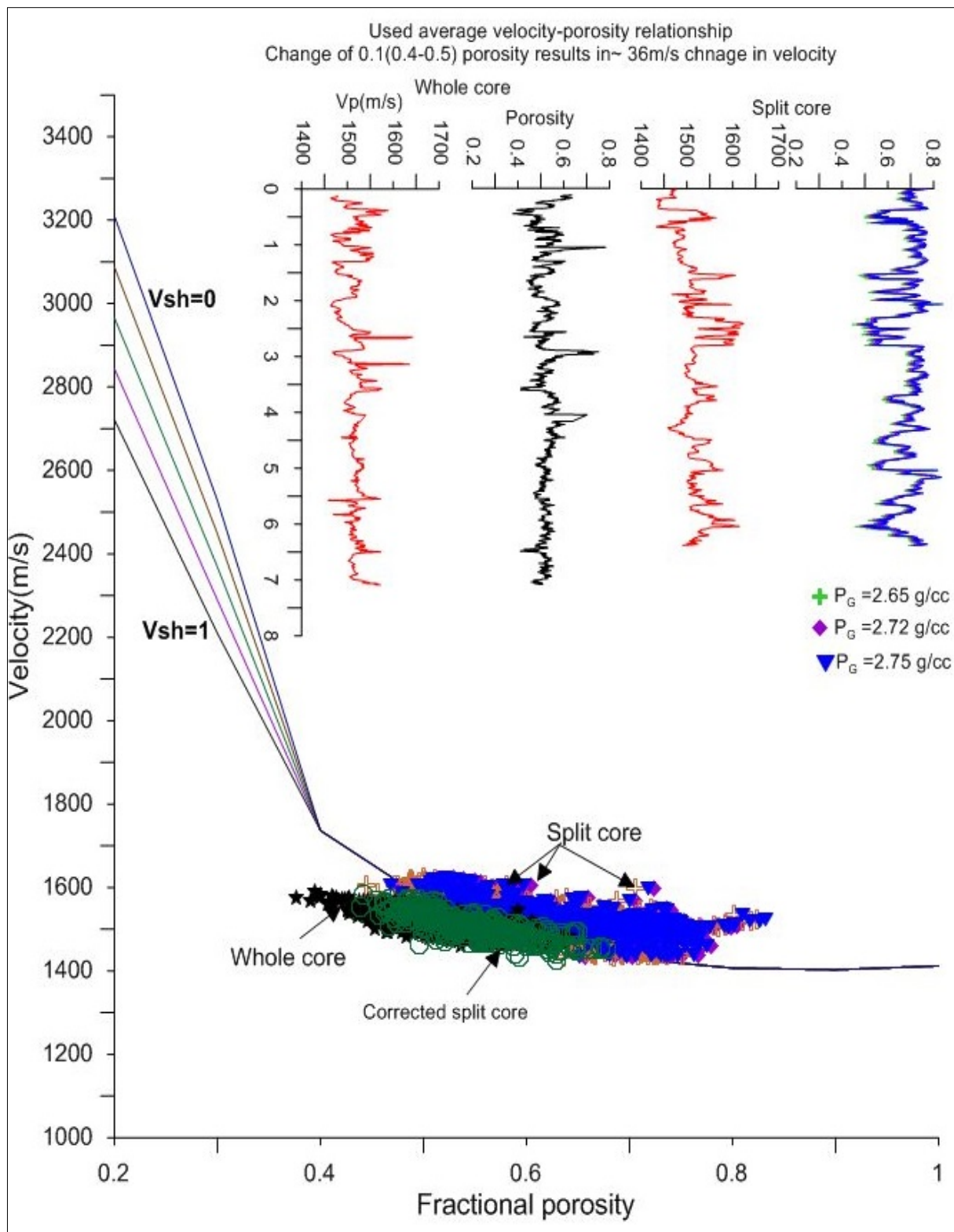


Fig.31. Normal consolidation relationship for prediction of velocity from Lomonosov Ridge sediments with the whole and split cores. The top and bottom curves represent shale fraction ($V_{sh}=1$) and shale ($V_{sh}=0$) respectively. The curves in the middle represent shale fractions 0.2, 0.4, 0.6, and 0.8. The velocity and porosity for split and whole core are plotted against depth, porosities calculated using different grain density are plotted (green, purple, and blue colors)

However, the measured velocities from this study do not fall exactly on the line predicted by the Erickson and Jarrad equation but the decreasing velocity fits the trend of increasing porosity along the predicted curve where velocity of the LOMROGIII sediment decreases rapidly with increasing porosity. The range of velocities from the Erickson and Jarrad equation for unconsolidated sediments is between ~ 1550 m/s and 2400 m/s at 0.40 porosity (Fig.32). Thus the measured data fall within this range. As porosity increases to 0.70 , the measured data still fits with the spread of velocity from the Erickson and Jarrad model ($1600 - 1800$ m/s). There is no data with porosity < 0.40 from LOMROGIII to correlate with the lower porosity from Erickson and Jarrad data.

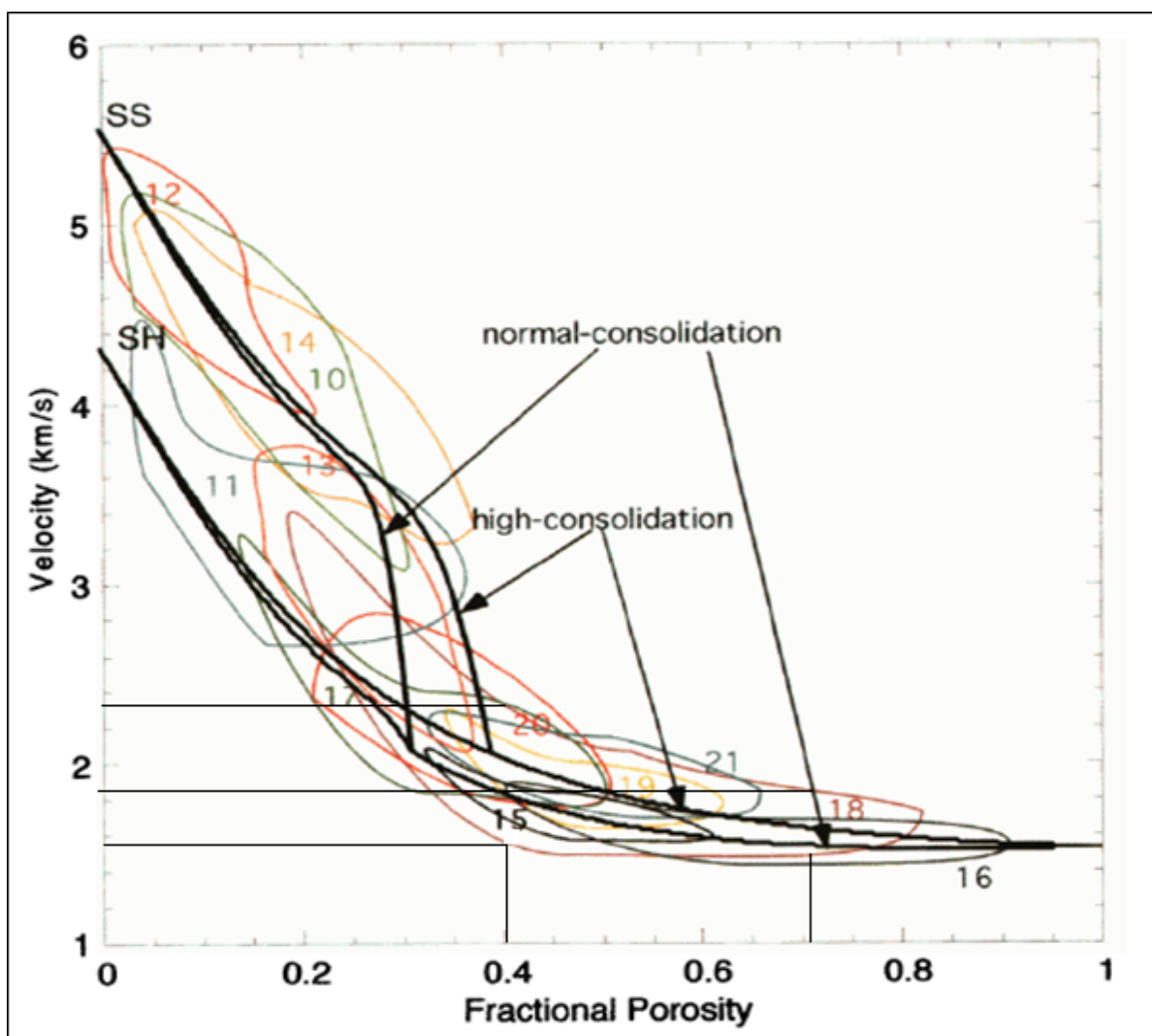


Fig.32. Comparisons of global empirical relationship data compared to a wide range of velocity-porosity ranges from different regions. The heavy black lines exhibit the normal- and high-consolidation global relationship used in the model after (Erickson and Jarrad, 1998). Circle 18 represents the range of normal consolidated sediments used in the Erickson and Jarrad model.

The overall velocity-porosity trend of sediments from the LOMROGIII shows an increase in the velocity associated with a decrease in porosity for all split and whole cores used in this study with some exceptions (Fig.33).

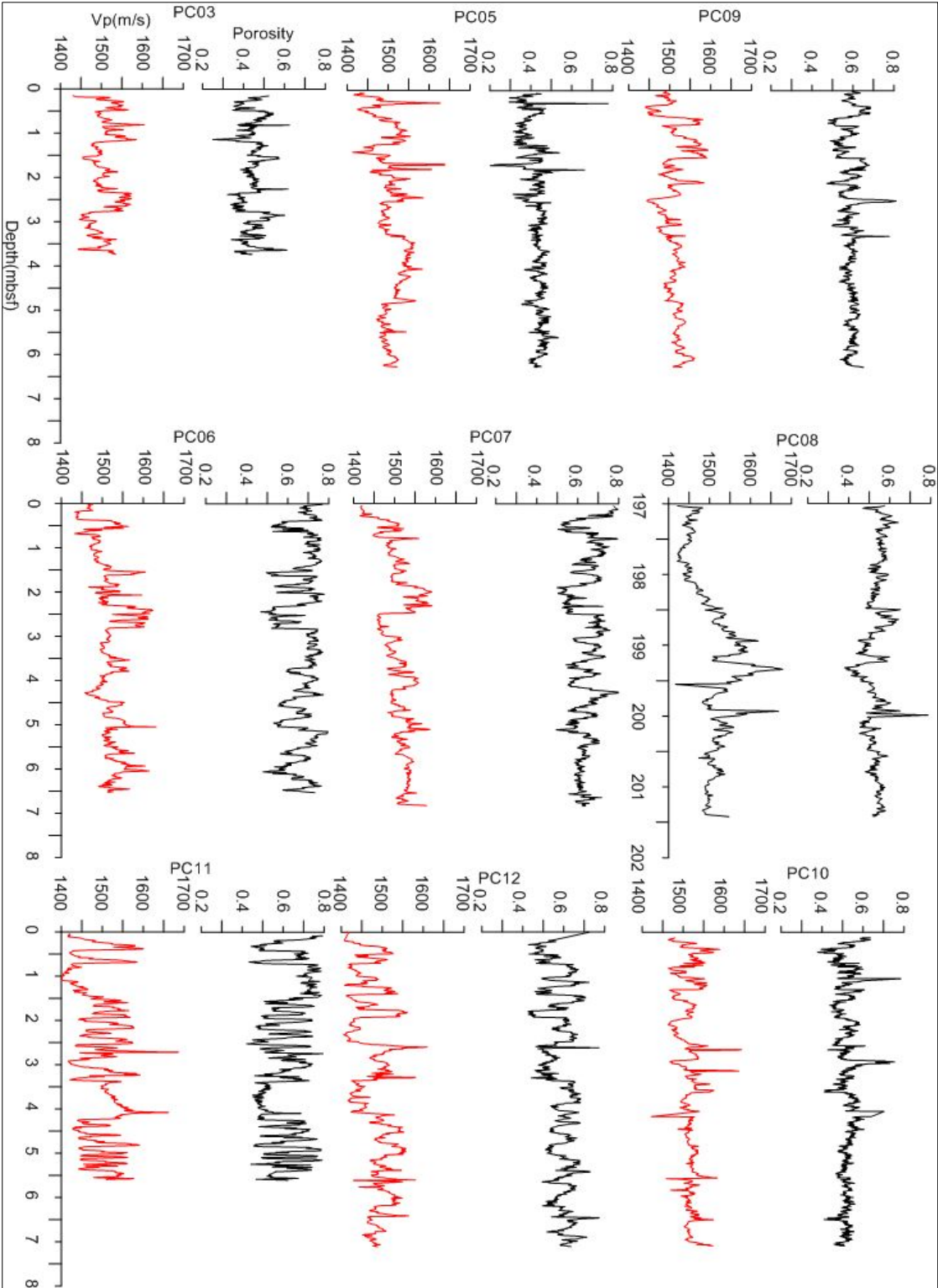


Fig.33 Relationship of velocity (red color) and porosity (black color) for all split and whole cores versus depth (mbsf).

6. Conclusion

The purpose of this study was to quantitatively assess the quality of compressional wave velocity and bulk density data obtained from using the Multi Sensor Core logger on split cores collected from Lomonosov Ridge. On the MSCL system, bulk density was calculated by measuring the intensity of attenuated gamma rays emitted from a constant source like Caesium-137 and detected on the other side of the core. The travel time needed for an acoustic pulse to pass through the sediments was measured using both the hard and soft P-wave transducers. The calibration of the compressional wave velocity and bulk density was carried out using a semi-cylindrical piece of aluminum with different diameters filled with water. The sediment core thickness was also measured by determining the distance taken by the upper (DT) to move up and down during core logging process.

One of the most significant problems facing split core logging is that the cores have uneven surfaces along the core section and are contained in different liners with different thicknesses. Because the quality of the compressional velocity and bulk density measurement is directly related to the quality of the measured core thickness, this variation in core thickness provides inaccurate core measurements which in turn affect the magnitude of the measured compressional velocity and bulk density data.

An evaluation of the results from the two types of P-wave transducers was made by comparing and contrasting the results from eight split cores with whole core measurements on PC10. It was found that data obtained from the hard transducer is more accurate than the soft transducer because it provides more precise core thickness measurements. The sources of weakness which could affect the quality of the measured properties using a soft transducer are the following: deformation of the oil-filled membrane surrounding the p-wave transducer, deformation of sediments caused by the load of the spring mounted in the plastic housing of the transducers, and incorrect selection of the reference point. However, removing the spring from the upper transducer housing improves the quality of obtained results.

The relevance of core thickness errors for the measured physical properties is clearly supported by the findings of this work. The average velocity and density with a range of core thickness were corrected for predicting the average change in these variables. Different travel time values and average logarithm of gamma ray were used. The results showed that a change of 1 mm core thickness results in ~ 34 m/s increase in velocity and ~ 0.05 g/cc decrease in bulk density. This finding provides that thickness errors would result in an increase in the compressional velocity and a decrease in bulk density or vice versa.

Detailed statistical analyses were performed to calculate differences in average velocity, density, and core thickness of split core in comparison with PC10. The findings from the linear velocity-core thickness and density-core thickness relationships were used to estimate average changes in the three variables. A correction based on increasing bulk density and decreasing velocity values was made. This study provides strong evidence that corrected velocity is the best indicator that can be used to correct offsets in core thickness. The influence on the velocity-density relationship of variables such as porosity and grain size within the LOMROGIII data was evaluated. The findings of this study indicated that the velocity and density increase generally with increasing grain size and decreasing porosity of sediments.

A comparison with three published models was performed to evaluate the accuracy of the data from LOMROGIII sediments. The Wyllie and Raymer models do not capture the porosity-velocity relationship of the Lomonosov Ridge sediments. Because the two models are applicable to low and intermediate porosities less than 0.37, the high porosity of sediments in this study (>40%) is the probably reason for the poor predictions of velocity from porosity trend. A global empirical relationship proposed by Erickson and Jarrad (1998) for siliciclastic sediments with normal consolidation provided the best prediction of compressional velocity from porosity. In the Erickson and Jarrad model, a change of 0.1 fractional porosity results in ~36 m/s decrease in velocity, which is similar to the predicted change in velocity if a core thickness error of 1 mm exists (34 m/s). This highlights the significance of accurate core thickness measurements in order to obtain high quality compressional velocity and bulk density datasets.

The present study confirms previous findings about the role of porosity as an indicator for checking the compressional velocity value. It also contributes evidence for the importance of grain size in controlling the velocity-density relationship of fine-grained siliciclastic sediments. More research is needed to develop a model that can be used to more accurately predict the velocities from a wide range of sediments including the LOMROGIII sediments.

Acknowledgements

First of all I would like to thank my supervisor Dr. Matt O'Regan for giving me the opportunity to start on this exciting study. Your advice, the discussion we have had, and your support helped me solve the challenges I have faced during my research. I am forever grateful. There is another person who I leaned on particularly heavily while trying doing my master project. This is my mother, who encouraged and supported me from the day one. My brother Abbas, my family in Iraq and Sweden I would like to express my deepest appreciation for all support and encourage you gave me. Furthermore I would also like to acknowledge with much appreciation to all those who provided me the possibility to complete this thesis particularly Elisabeth Däcker, Hildred Crill, Helena Pentinsaari, and all staff of the department of Geological Science at Stockholm university.

References

- Anderson, O.L., Schreiber, E., Liebermann, R.C., Soga, N., 1968. Some elastic constant data on minerals relevant to geophysics. Reviewed. *Geophysics*. 6:491-524.
- Bachman, R.T.1985. Acoustic and physical property relationships in marine sediments. *Journal of the Acoustic Society of America* 78:616-321.
- Bachman R.T., 1989. Estimating velocity ratio in marine sediment. *Journal of the Acoustical Society of America* 86:2029-2032.
- Best, A.I., Gunn, D.E., 1999. Calibration of marine sediment core loggers for quantitative acoustic impedance studies. *Marine geology* 160:137-146
- Birch, F., 1961. The velocity of compressional waves in rocks to 10 kilobars, 1, *Journal of Geophysics Research* 65: 1083-1102, 1960; 2, 66: 2199-2224.
- Birch, F., 1966. Compressibility: *Elastic constants, in handbook of Geophysical Constant*, edited by S.P. Clark, J.R., *Journal of Geological Society of America* 97:98-174.
- Blum, P., 1997. Physical properties handbook: a guide to the shipboard measurement of physical properties of deep-sea cores. *Ocean Drilling Program. Note, 26* [Online].
- Brace, W. F., 1965. Some new measurements of linear compressibility of rocks. *Journal of Geophysics Research* 70(2): 391-398.
- Breitzke, M., 2006. Physical Properties of Marine Sediments, *Journal of marine geochemistry*. pp. 27-71.
- Christenson, N.L., 1966. Compressional wave velocities in single crystals of alkali feldspar at pressure to 10 kilobars. *Journal of Geophysics Research* 71:3113-3116.
- Dvorkin, J., Amos, N., 2001. Time-Average Equation Revisited. *Geophysics*.

Erickson, S.N., Jarrad, R.D., 1998. Velocity-porosity relationship for water-saturated siliciclastic sediments. *Journal of Geophysical Research*, 103:30385-30460.

Gassmann, F., 1951. Über die elastizität poröser medien: Vierteljahrsschrift der Naturforschenden Gesellschaft in Zurich, 96,1-23. The English translation of this paper is available at <http://sepwww.stanford.edu/sep/berryman/PS/gassmann.pdf>.

GEOTEK MSCL Manual, 2000. (geotek.co.uk/downloads/)

Goldberg, I. Gurevich, B., 1989. A semi-empirical velocity-porosity clay model for petrophysical interpretation of P- and S-velocities. *Geophysics.Prospect.*46:271–285.

Gunn, D.G., Best, A.L., 1998. A new automated nondestructive system for high resolution multi-sensor core logging of open sediments cores. *Geo-Marine Letters* 18:70-77.

Hamilton, E.L., 1956. Low sound velocities in high-porosity sediments. *Journal of Acoustic Society of America* 28:16-19.

Hamilton, E. L., G. Shumway, H. W. Menard, Shipek, C.J., 1956. Acoustic and other physical properties of shallow-water sediments of San Diego. *Journal of Acoustic of Society of America* 128:1-15.

Hamilton, E. L., 1963. Sediments sound velocity measurements made in situ from Bathyscaph Trieste, *Journal of geophysics Research* 68:5991-5998.

Hamilton, E. L., 1970. Sound velocity and related properties of marine sediments, North Pacific. *Journal of Geophysical Research* 75(23):4423-4446.

Hamilton, E. L., 1971. Elastic properties of marine sediments. *Journal of Geophysics Research*, 76(2):579-604.

Hamilton, E. L., 1972. Compressional Wave Attenuation in Marine Sediments. *Geophysics* 37: 620-646.

Hamilton, E. L., Moore, D. G., Buffington, E. C., Sherrer, P. L., Curray, J.R., 1974. Sediment Velocities from Son buoys: Bay of Bengal, Bering Sea, and North Pacific. *Journal of Geophysics Research* 79:2653-2668.

Hamilton, E. L., 1980. Geoacoustic Modeling of the Sea Floor. *Journal of Acoustic Society of America* 68: 1313-1340.

Hamilton, E.L. 1979. Sound velocity gradients in marine sediments. *Journal of the acoustical Society of America* 65:909-922.

Hamilton E.L., Bachman R.T., 1982. Sound velocity and related properties of marine sediments. *Journal of the Acoustical Society of America* 68:1891-1904.

- Han, D. H., Nur, A., Morgan, D., 1986. Effect of porosity and clay content on wave velocities in sandstones. *Geophysics* 51: 2093–2107.
- Horn, D. R., Horn, B. M., Delach. M. N., 1968. Correlation between acoustical and other geophysical properties of deep- sea cores. *Journal of Geophysical research* 73:1939-1957.
- Jokat, W., Uenzelmann-Neben, G., Kristoffersen, Y., Rasmussen, T.M., 1992. Lomonosov Ridge-A double-sided continental margin. *Geology* 20:887-890.
- Kahraman, S., 2002. The effects of fracture roughness on P-wave velocity. *Engineering Geology* 63:347–350.
- Kristoffersen Y (1990) Chapter 21: Eurasia Basin: in The Arctic ocean region, v. L, (Eds) Grantz, A., Johnson, L., Sweeney, J.F., Boulder, Colorado, *Geological Society of America*, 365–378.
- Leroy, C.C., 1969. Development of simple equations for accurate and more realistic calculation of the speed of sound in seawater. *Journal of Acoustic Society of America*, 46(1B):216–226.
- Moran, K., Backman., Brinkhuis, H., Clemens, S.C., Cronin T., Dickens, G.R., Eynaud, F., Gattacceca, J., Jakobsson, M., Jordan, R.W., Kaminski, M., King, J., Koc, N., Krylov, A., Martinez, N., Matthiessen, J., McInroy, D., Moore, T.C., Onodera, J., O'Regan, M., Pälike H., Rea, B., Rio, D., Sakamoto, T., Smith, D.C., Stein, R., John, K. St., Suto, I. , Suzuki, N. , Takahashi, K., Watanabe, M. , Yamamoto, M. , Farrell, J., Frank, M. , Kubik, P. , Jokat, W. Kristofferson, Y., 2006. The Cenozoic palaeoenvironment of the Arctic Ocean. *Nature* 441:601–605.
- Moran, K., Altmann, V., O'Regan, M., Ashman as, C., 2007. Acoustic Compressional Wave Velocity as a Predictor of Glacio-marine Sediment Grain Size. *Geotechnical Testing Journal* 30(4):1-7.
- Morris, H.T., Clark, D.L., BLASCO, S.M., 1985. Sediments of the Lomonosov Ridge and Makarov Basin: A Pleistocene stratigraphy for the North Pole. *Geological Society of America Bulletin* 96(7):901-910.
- Nafe, J. E., Drake. C. L., 1957. Variation with depth in shallow and deep water marine sediments of porosity, density, and velocities of compressional and shear waves. *Geophysics* 22:523-552.
- Nafe, J. E., Drake. C. L., 1963. Physical properties of marine sediments, in The Sea, edited by M. N. Hill, :794-815, Interscience, New York.
- Paoletti, V., 2012. Remarks on factors influencing shear wave velocities and their role in evaluating susceptibilities to earthquake-triggered slope instability: case study for the Campania area (Italy). *Journal of Natural Hazards of Earth System Society* 12:2147-2158.

Ramm, M., 1992. Porosity depth trends in reservoir sandstones; Theoretical models related to Jurassic sandstones offshore Norway. *Journal of Marine Petroleum Geology* 9: 553-567.

Raymer, L. L., Hunt, E. R., Gardner, J. S., 1980. An improved sonic transit time-to-porosity transform: SPWLA 21 *Annual Logging Symposium*: 1-13.

Rider, M.H., 2000. The geological interpretation of well logs, Rider-French Consulting Ltd. Progress Press Co Ltd., Malta.

Rider, M.H., Kennedy, M., 2011. The geological interpretation of well logs. Rider-French Consulting Limited.

Richardson M.D., Briggs K.B., 1993. On the use of acoustic impedance values to determine sediment properties. In: Pace NG, Langhorne DN (Eds.), *Acoustic Classification and Mapping the Seabed*. Institute of Acoustics, University of Bath, Bath, UK. 15-25.

Richardson, M. D., Lavoie D. L., Briggs, K. B., 1997. Geoacoustic and physical properties of carbonate sediments of the Lower Florida Keys. *Geo-Marine Letters* 17: 316-324.

Ryan, W. B. F., F. Workum, J.R., Hersey, J. B. 1965. Sediments on the Tyrrhenian Abyssal Plain. *Bulletin Geological Society of America* 76:1261-1282.

Schnack-Friedrichsen, A., Davis, A. M., Bennell, J. M., Huws, D. G., 2010: Assessing the validity of Seismo-Acoustic Predictor Equations for Obtaining seabed and Sub-Surface sediment physical Properties, *Marine Georesources and Geotechnology* 19(4): 221-243.

Shumway, G., 1960. Sound speed and absorption studies of marine sediments by a resonance method, 1 and 2. *Geophysics* 25: 451-467; 659-682.

St. John, K., 2008. Cenozoic ice-rafting history of the central Arctic Ocean: Terrigenous sands on the Lomonosov Ridge. *Paleoceanography* 23:1-12.

Simmons, G. Brace, W. F., 1965. Compaction of Static and Dynamic Measurements of Compressibility of Rocks. *Journal of Geophysical Research* 70(22):5649-5656.

Sutton, G. H., Bruckheimer, H., Nafe, J. E., 1957. Physical Analysis of Deep-Sea Sediments. *Geophysics* 22: 779-812.

Swarbrick, R.E., Osborne, M.J., 1998. Mechanisms that generate abnormal pressures; an overview. In: Law, B.E., Ulmishek, G.F., Slavin, V.I. (Eds.), *Abnormal pressures in hydrocarbon environments*. American Association of Petroleum Geologists, Tulsa, OK, United States, 13-34.

Tosaya, C. Nur, A., 1982. Effects of lack of parallelism in sample faces on measurements of ultrasonic attenuation. *Journal of Geophysics Research Letter* 9: 5–8.

Weber, M.E., Niessen, F., Kuhn, J., Wiedicke, M., 1997. Calibration and application of marine sedimentary physical properties using a multi-sensor core logger, *Journal of Marine Geology* 136:151-172

Wiedicke, M.H., Weber, M.E., 1996. Small –Scale variability of seafloor features in the Northern Peru Basin: results from acoustic survey methods, *Marine Geophysical Research* 18:507-526.

Wood, J.R., 1989. Modeling the effect of compaction and precipitation/dissolution on porosity. In short course in burial diagenesis (Hutcheon, I.E., editor) *Mineralogical Association of Canada* 15:311-362.

Wyllie, M.R.J., Gregory, A.R., Gardner, L.W., 1956. An experimental investigation of factors affecting elastic wave velocities in porous media, *Geophysics* 21:41-70.

Appendix 1

The locations, depth , and length of the collected cores during LOMROGIII and logging notes for split cores used in this study from the hard and soft transducers measurements.

Core Name	Date	Time_UTC	Latitude_DMS	Longitude_DMS	LatN_DD	LonE_DD	Depth_m	CoreLength_m
LOMROG12-GC01	2012.08.10	11:04:29	87°46'25N	42°47'53W	87.77361	-42.7986	3838	Empty (gravel)
LOMROG12-PC02	2012.08.10	19:01:42	87°47'20N	42°56'28W	87.788889	-42.9411	3274	0.525
LOMROG12-PC03	2012.08.11	19:53:51	87°43'29N	54°25'31W	87.72472	-54.42528	1607	3.73
LOMROG12-TC04	2012.08.12	08:32:50	87°49'10N	59°35'24W	87.81944	-59.59	1322	0.705
LOMROG12-PC05	2012.08.12	14:10:53	87°49'14N	59°37'55W	87.82056	-59.63194	1321	6.29
LOMROG12-PC06	2012.08.15	11:34:11	88°15'04N	46°23.'50W	88.25111	-46.3972	2923	6.595
LOMROG12-PC07	2012.08.15	19:44:08	88°11'51.5N	55°41'04.3W	88.19764	-55.68453	2522	6.8
LOMROG12-PC08	2012.08.16	11:20:37	88°20'22.4N	68°43'42.4W	88.33955	-68.7284	1355	7
LOMROG12-PC09	2012.08.18	19:56:48	89°01'36.2N	73°44'04.0W	89.02672	-73.7344	1318	6.48
LOMROG12-PC10	2012.08.19	09:44:51	89°01'20.8N	73°45'58.8W	89.02244	-73.7663	1312	7.11
LOMROG12-PC11	2012.08.23	02:05:01	89°58'06N	58°27'37.68W	89.96835	-58.4607	4228	6.04
LOMROG12-PC12	2012.08.24	22:12:17	88°06'30.8N	134°38'42.5E	88.10845	134.654	1366	7.27

TableA1-1. Depth. Length and locations for cores collected from Lomonosov Ridge during LOMROGIII.

Core	Section number	Shipboard interval (TOP)	Shipboard interval (BOTTOM)	Section Length (LINER)	Logged (mbsf)	Calibration file	File name	RCT (cm)
PC11	1	0	17	27	0.16	12-11-2012	LOMROG12-PC11-sec-1	3.2
	2	17	155.5	150	1.67	12-11-2012	LOMROG12-PC11-sec-2	4
	3	155.5	300	150	3.13	12-11-2012	LOMROG12-PC11-sec-3	4
	4	300	450	150	4.63	13-11-2012	LOMROG12-PC11-sec-4	4
	5	450	604	154	6.18	13-11-2012	LOMROG12-PC11-sec-5	4
PC12	1	0	127	135.5	1.09	13-11-2012	LOMROG12-PC12	3.9
	2	127	273.5	151	2.56	13-11-2012	LOMROG12-PC12	3.9
	3	273.5	423.5	150	4.07	13-11-2012	LOMROG12-PC12	3.9
	4	423.5	573	150	5.58	14-11-2012	LOMROG12-PC12	3.9
	5	573	727	155	7.12	14-11-2012	LOMROG12-PC12	3.9
TC09	1	0	15.5	23.5	0.14	14-11-2012	LOMROG12-TC09	3.9
PC09	1	0	43	51	0.51	12-11-2012	LOMROG12-PC09-sec-1	3.9
	2	43	193	151	2.01	14-11-2012	LOMROG12-PC09	3.9
	3	193	344	151	3.52	14-11-2012	LOMROG12-PC09	3.9
	4	344	494.5	151	5.02	14-11-2012	LOMROG12-PC09	3.9
	5	494.5	648	154	5.05	14-11-2012	LOMROG12-PC09	3.9
PC07	1	0	80.5	89.5	0.63	15-11-2012	LOMROG12-PC07	3.9
	2	80.5	230.5	151.5	2.13	15-11-2012	LOMROG12-PC07	3.9
	3	230.5	381.5	151.5	3.64	15-11-2012	LOMROG12-PC07	3.9
	4	381.5	532	151	5.14	15-11-2012	LOMROG12-PC07	3.9
	5	532	683	151	6.65	15-11-2012	LOMROG12-PC07	3.9
PC05	1	0	28.5	35	0.27	18-11-2012	LOMROG12-PC05-sec-1	3.36
TC06	1	0	55	61	0.52	18-11-2012	LOMROG12-TC06	3.9
PC06	1	0	58	67.6	0.57	18-11-2012	LOMROG12-PC06	3.9
	2	58	208	151	2.08	18-11-2012	LOMROG12-PC06	3.9
	3	208	355	147.7	3.56	18-11-2012	LOMROG12-PC06	3.9
	4	355	506	151	5.07	18-11-2012	LOMROG12-PC06	3.9
	5	506	659.5	153.7	6.62	18-11-2012	LOMROG12-PC06	3.9
PC05	3	179	326	148	3.26	18-11-2012	LOMROG12-PC05-sec-3	3.9
PC08	3	197	345.5	150.5	198.46	19-11-2012	LOMROG12-PC08	3.9
	4	345.5	494.5	152	199.97	19-11-2012	LOMROG12-PC08	3.9
	5	494.5	645	150	201.48	19-11-2012	LOMROG12-PC08	3.9
TC03	1	0	52.5	57.5	0.51	19-11-2012	LOMROG12-TC03	3.9
PC03	1	0	73	81.5	0.72	19-11-2012	LOMROG12-PC03	3.9
	2	73	233	150.8	2.22	19-11-2012	LOMROG12-PC03	3.9
	3	233	373	150.7	3.72	19-11-2012	LOMROG12-PC03	3.9
TC04	1	0	70.5	77.5	0.67	19-11-2012	LOMROG12-TC04	3.9
PC05	2	28.5	179	151	1.78	20-11-2012	LOMROG12-PC05-sec-2	3.9
TC05	1	0	29	41	0.29	23-11-2012	LOMROG12-TC05	3.9
PC05	4	326	476	151	4.76	23-11-2012	LOMROG12-PC05-sec-4	3.9
PC05	5	476	629	154	6.29	23-11-2012	LOMROG12-PC05-sec-5	3.9

TableA1-2 .Core loggings notes for the measurements of split core samples using acoustic soft transducer.

Core	Section number	Shipboard interval (TOP)	Shipboard interval (BOTTOM)	Section Length (LINER)	Logged (mbsf)	Calibration	File name	RCT (cm)
PC11	1	0	17	27	0.16	13-12-2012	LOMROG12-PC11-HT	3.9
	2	17	155.5	150	1.27	13-12-2012	LOMROG12-PC11-HT	3.9
	3	155.5	300	150	2.72	13-12-2012	LOMROG12-PC11-HT	3.9
	4	300	450	150	4.08	13-12-2012	LOMROG12-PC11-HT	3.9
	5	450	604	154	5.62	13-12-2012	LOMROG12-PC11-HT	3.9
PC12	1	0	127	135.5	1.12	16-12-2012	LOMROG12-PC12-HT	3.9
	2	127	273.5	151	2.59	16-12-2012	LOMROG12-PC12-HT	3.9
	3	273.5	423.5	150	4.10	16-12-2012	LOMROG12-PC12-HT	3.9
	4	423.5	573	150	5.61	16-12-2012	LOMROG12-PC12-HT	3.9
PC09	1	0	43	51	0.26	16-12-2012	LOMROG12-PC09-HT	3.9
	2	43	193	151	1.78	16-12-2012	LOMROG12-PC09-HT	3.9
	3	193	344	151	3.29	16-12-2012	LOMROG12-PC09-HT	3.9
	4	344	494.5	151	4.80	16-12-2012	LOMROG12-PC09-HT	3.9
	5	494.5	648	154	6.26	16-12-2012	LOMROG12-PC09-HT	3.9
PC12	5	573	727	155	7.15	16-12-2012	LOMROG12-PC12-sec 5-HT	3.9
PC08	3	197	345.5	150.5	198.49	17-12-2012	LOMROG12-PC08-HT	3.9
	4	345.5	494.5	152	199.98	17-12-2012	LOMROG12-PC08-HT	3.9
	5	494.5	645	150	201.44	17-12-2012	LOMROG12-PC08-HT	3.9
PC07	1	0	80.5	89.5	0.79	17-11-2012	LOMROG12-PC07-HT	3.9
	2	80.5	230.5	151.5	2.30	17-11-2012	LOMROG12-PC07-HT	3.9
	3	230.5	381.5	151.5	3.81	17-11-2012	LOMROG12-PC07-HT	3.9
	4	381.5	532	151	5.32	17-11-2012	LOMROG12-PC07-HT	3.9
	5	532	683	151	6.85	17-11-2012	LOMROG12-PC07-HT	3.9
PC06	1	0	58	67.6	0.56	18-12-2012	LOMROG12-PC06-HT	3.9
	2	58	208	151	2.07	18-12-2012	LOMROG12-PC06-HT	3.9
	3	208	355	147.7	3.54	18-12-2012	LOMROG12-PC06-HT	3.9
	4	355	506	151	5.05	18-12-2012	LOMROG12-PC06-HT	3.9
	5	506	659.5	153.7	6.52	18-12-2012	LOMROG12-PC06-HT	3.9
PC05	1	0	28.5	35	0.28	18-12-2012	LOMROG12-PC05-HT	3.9
	2	28.5	179	151	1.79	18-12-2012	LOMROG12-PC05-HT	3.9
	3	179	326	148	3.26	18-12-2012	LOMROG12-PC05-HT	3.9
	4	326	476	151	4.77	18-12-2012	LOMROG12-PC05-HT	3.9
	5	476	629	154	6.31	18-12-2012	LOMROG12-PC05-HT	3.9
PC03	1	0	73	81.5	0.72	18-12-2012	LOMROG12-PC03-HT	3.9
	2	73	233	150.8	2.17	18-12-2012	LOMROG12-PC03-HT	3.9
	3	233	373	150.7	3.67	18-12-2012	LOMROG12-PC03-HT	3.9

TableA1-3. Core loggings notes for the measurements of split core samples using hard transducer.

Appendix 2

Physical properties *measurements for whole and split cores*

In general, the core samples can be described as mottled silty clay sediments. Grain size of the most samples lies in clay and silt range with considerable amounts of fine-course sand including some pebbles. The cores show broad color variations from very dark in some samples to light in others. The boundaries are generally indistinct but can be easily distinguished in some samples. In this study, the measured physical properties on the split core samples are: the compressional P-wav velocity (m/s), bulk density (g/cc), and magnetic susceptibility MS1 (SI x 10⁻⁵). These properties were plotted against depth (mbsf). Magnetic susceptibility logging was ignored in this study. Core thickness was plotted against depth to follow the trend of physical properties along the core samples being logged.

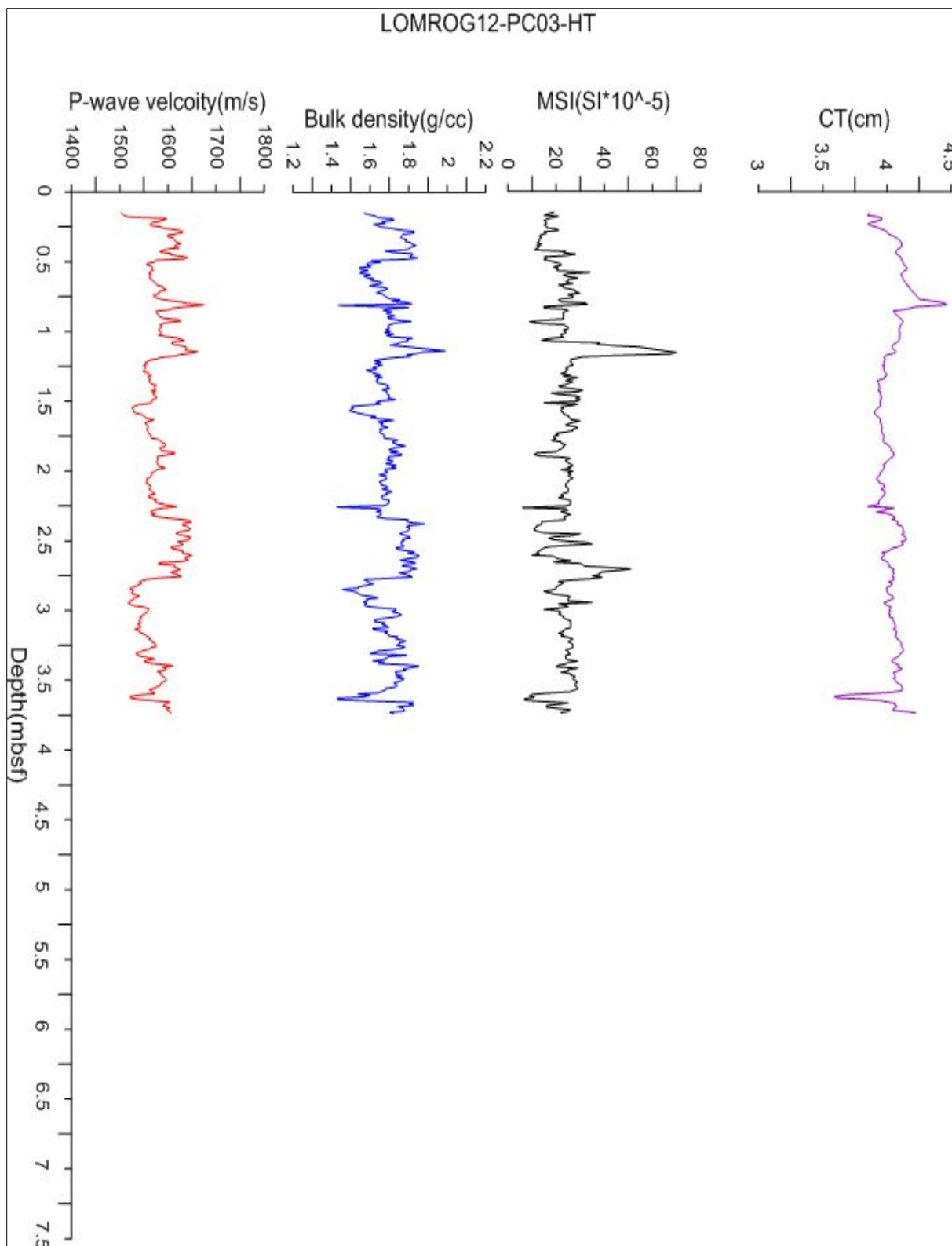


Fig.A2-1 The compressional velocity, bulk density, and magnetic susceptibility for the Lomonosov Ridge from LOMROGIII PC03 core plotted against depth (mbsf). The physical properties records were carried out using

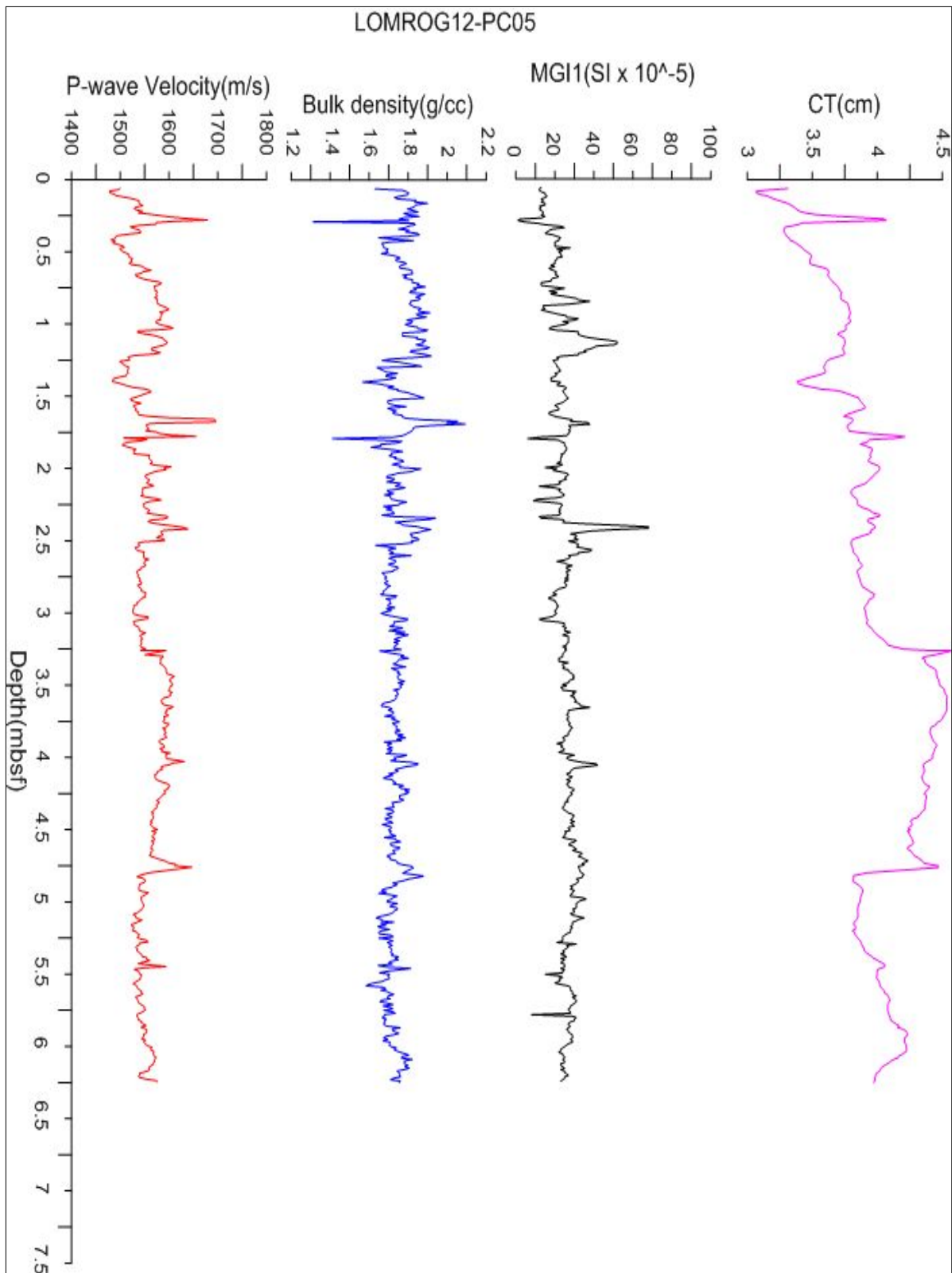


Fig.A2-2. The compressional velocity, bulk density, and magnetic susceptibility for the Lomonosov Ridge from LOMROGIII PC05 core plotted against depth (mbsf). The physical properties records were carried out

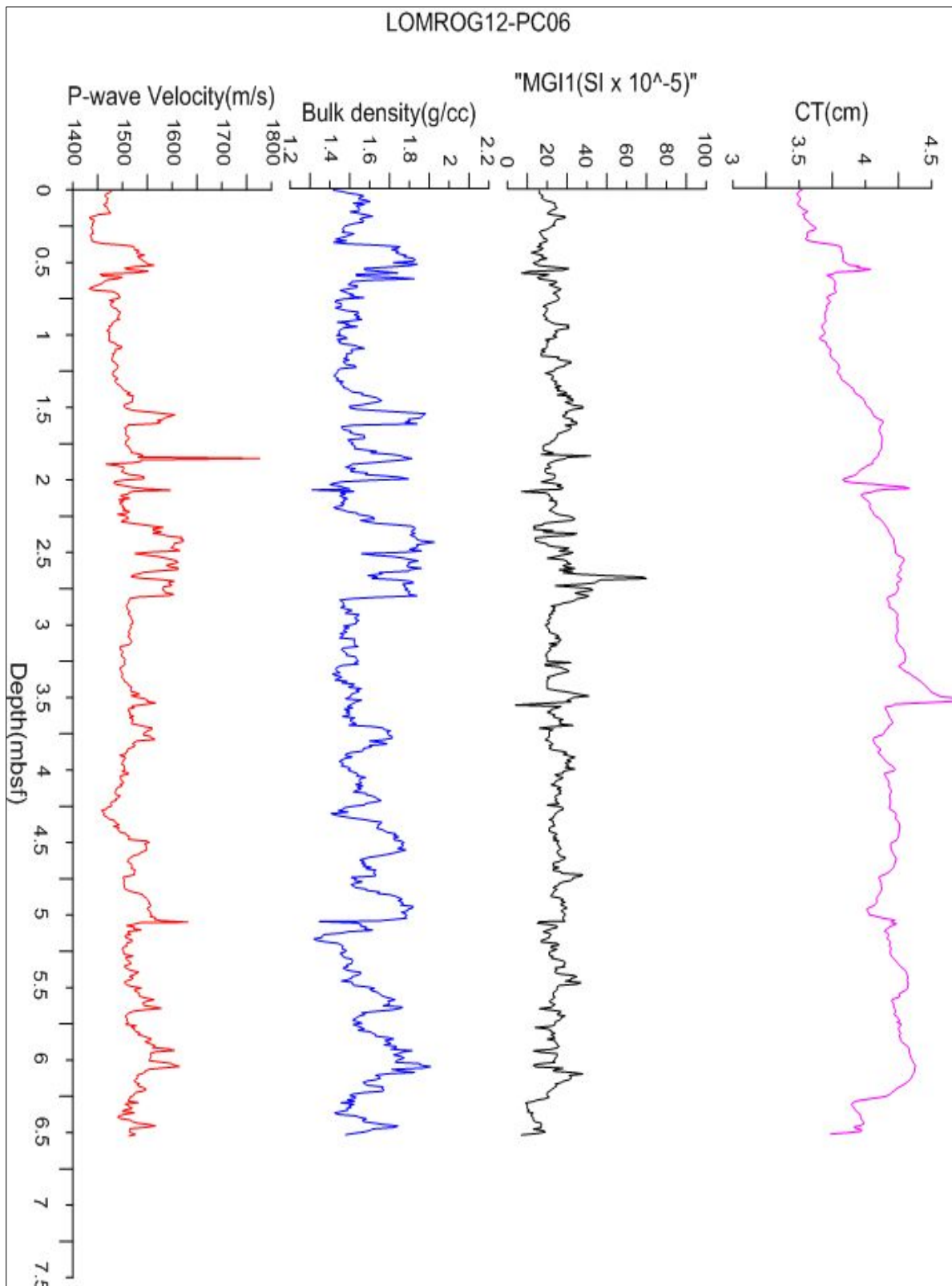


Fig.A2-3. The compressional velocity, bulk density, and magnetic susceptibility for the Lomonosov Ridge from LOMROGIII PC06 core plotted against depth (mbsf). The physical properties records were carried out using hard transducer.

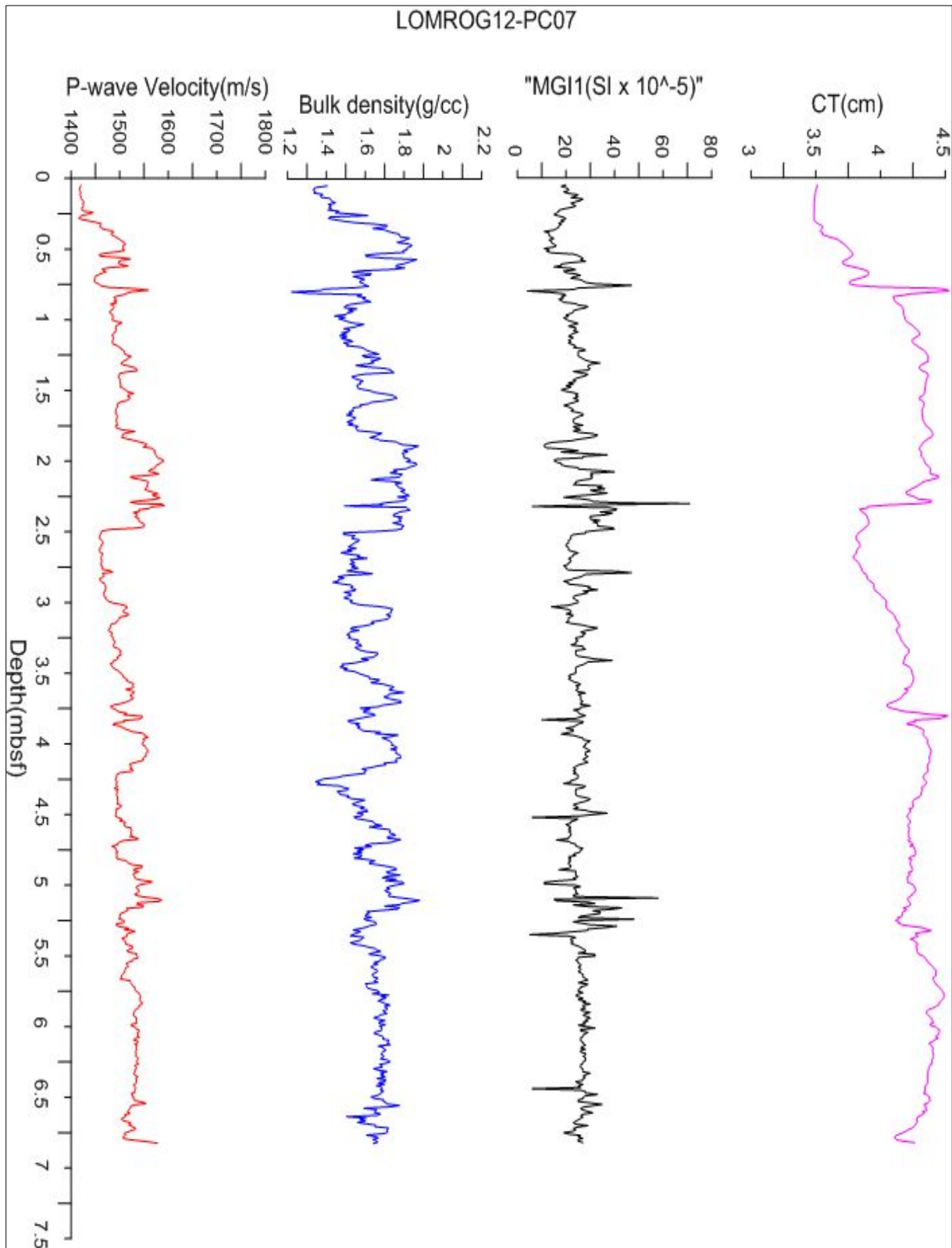


Fig.A1-4. The compressional velocity, bulk density, and magnetic susceptibility for the Lomonosov Ridge from LOMROGIII PC07core plotted against depth (mbsf).The physical properties records were carried out using hard transducer.

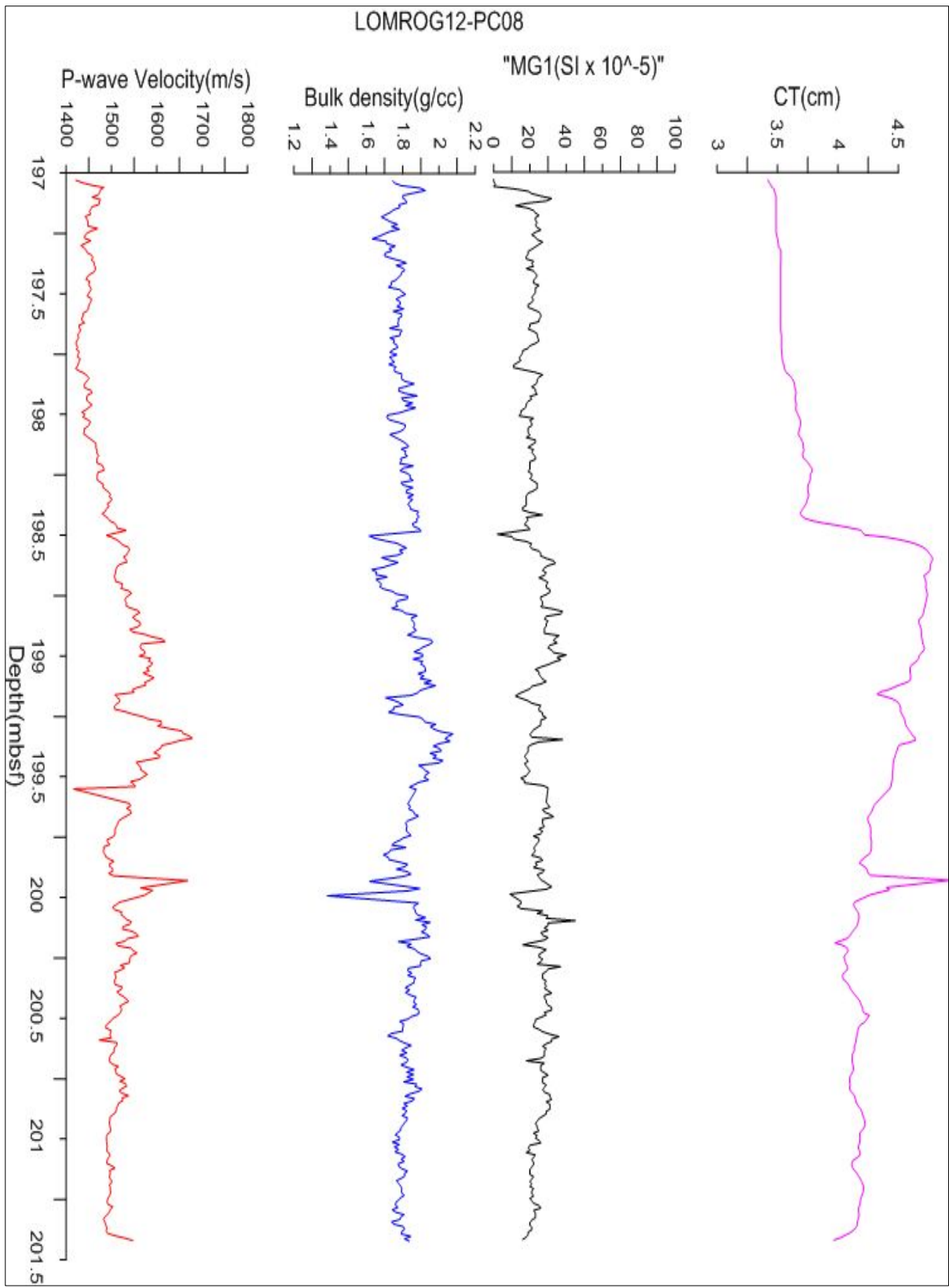


Fig.A2-5. The compressional velocity, bulk density, and magnetic susceptibility for the Lomonosov Ridge from LOMROGIII PC08core plotted against depth (mbsf). The physical properties records were carried out using hard transducer.

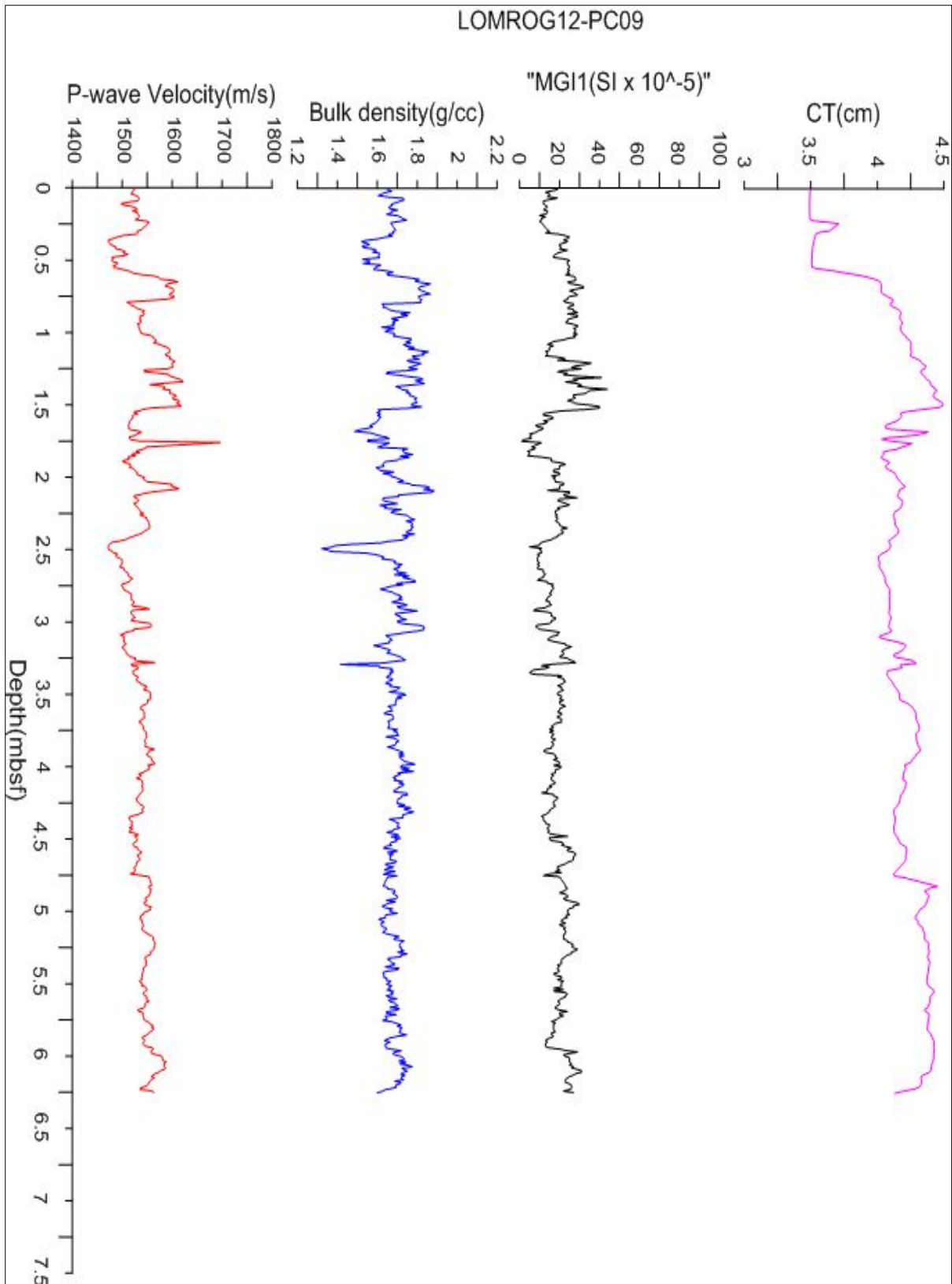


Fig.A2-6.The compressional velocity, bulk density, and magnetic susceptibility for the Lomonosov Ridge from LOMROGIII PC09 core plotted against depth (mbsf). The physical properties records were carried out using hard transducer.

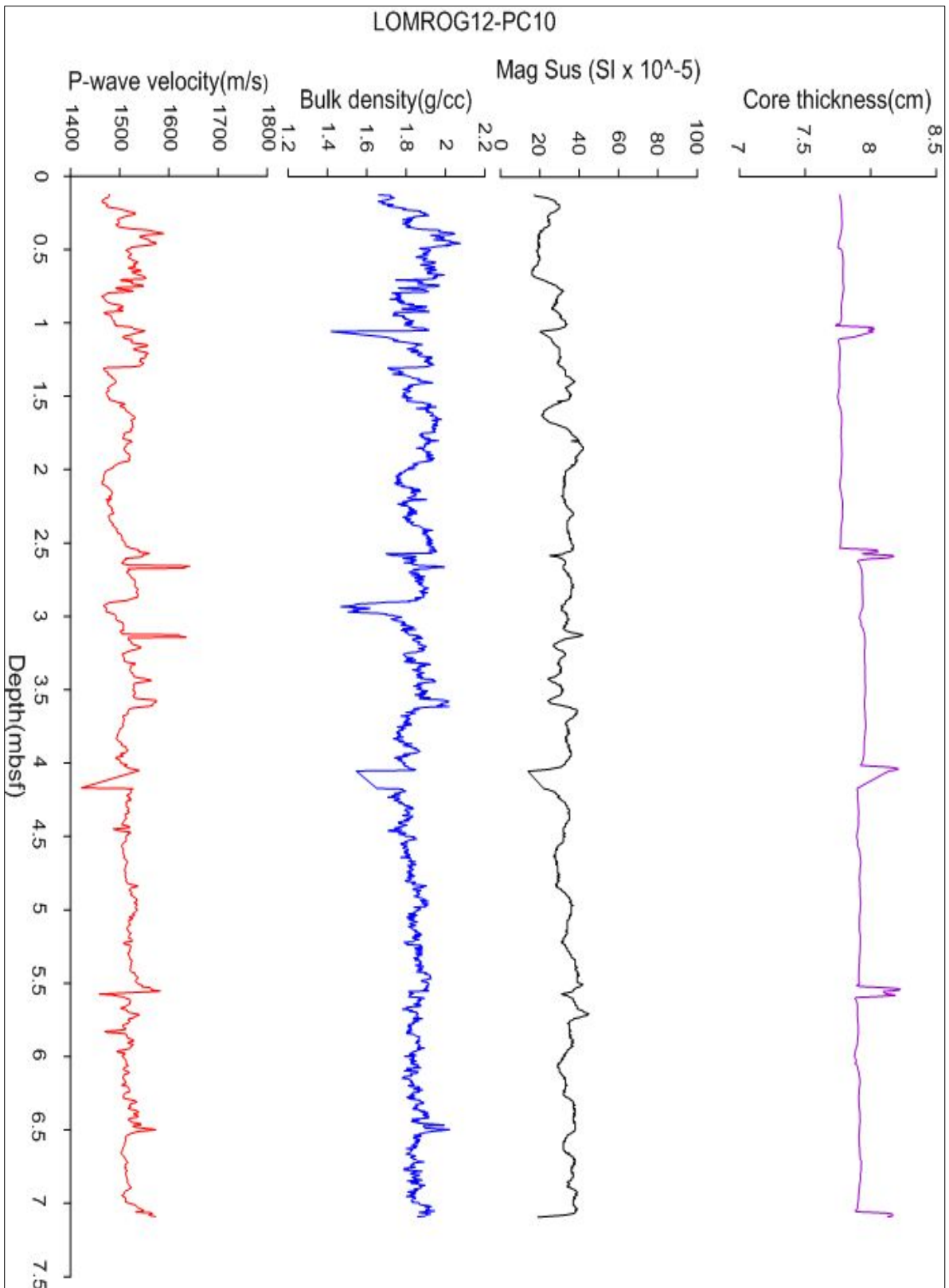


Fig.A2-7. The compressional velocity, bulk density, and magnetic susceptibility for the Lomonosov Ridge from LOMROGIII PC10 core plotted against depth (mbsf). The physical properties records were carried out using hard transducer.

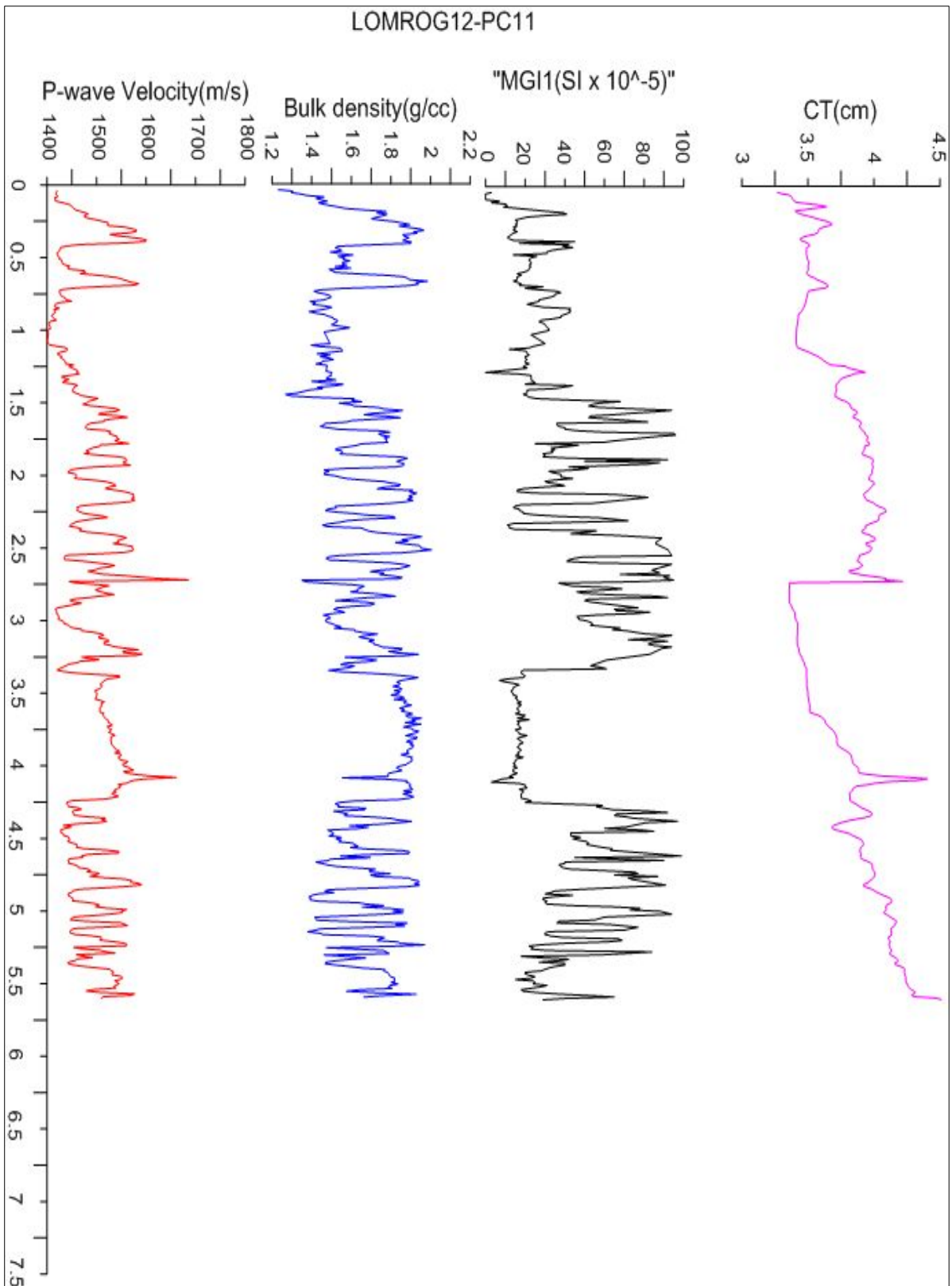


Fig.A2-8. The compressional velocity, bulk density, and magnetic susceptibility for the Lomonosov Ridge from LOMROGIII PC11core plotted against depth (mbsf). The physical properties records were carried out using hard transducer.

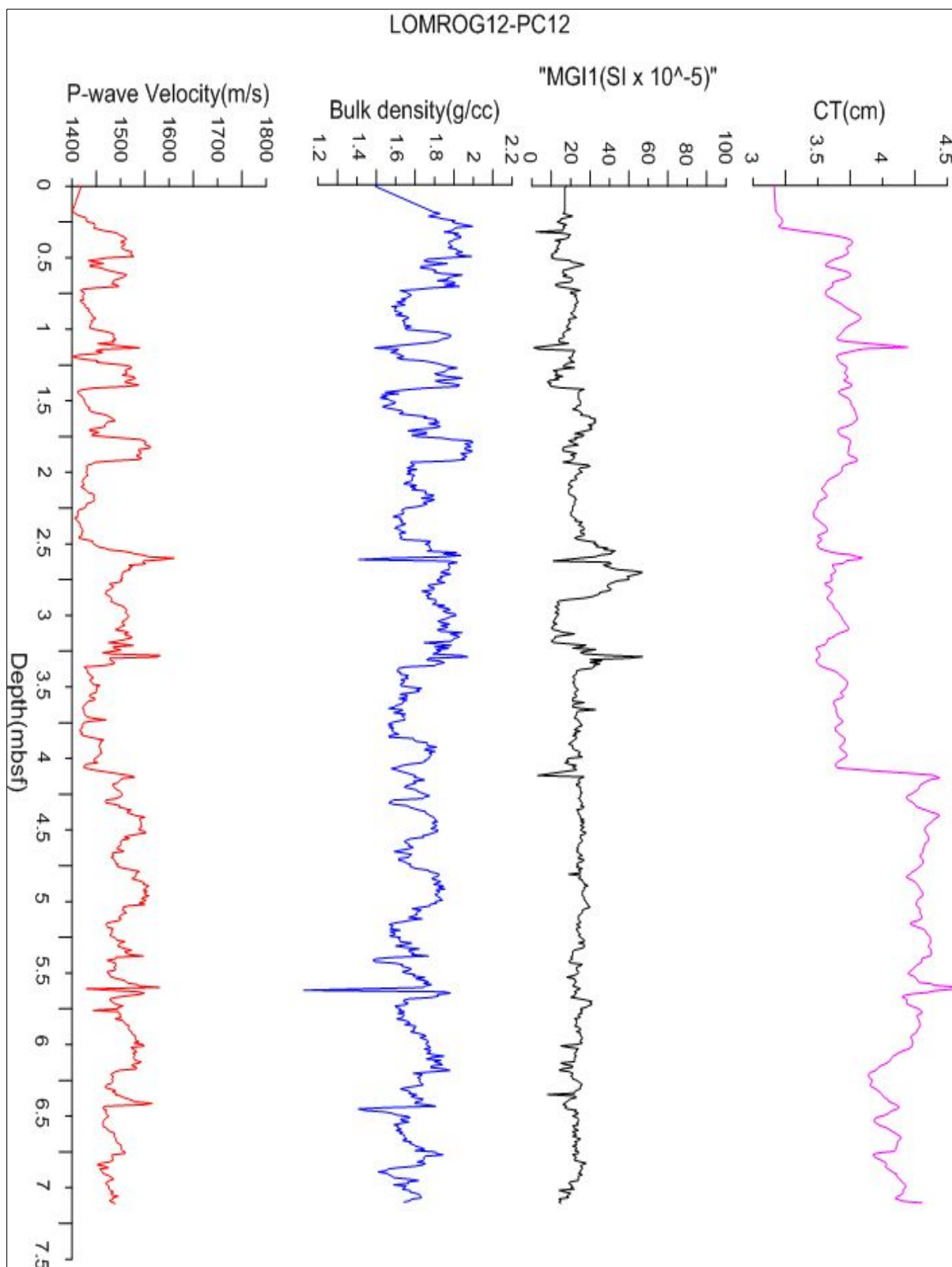


Fig.A2-9. The compressional velocity, bulk density, and magnetic susceptibility for the Lomonosov Ridge from LOMROGIII PC11core plotted against depth (mbsf). The physical properties records were carried out using hard transducer.